Correlated Spin Phenomena in Molecular Quantum Transport Devices

de Bruijckere, Joeri

DOI
10.4233/uuid:9e3a8b94-87b4-4167-a80c-8cddec3ae58e

Publication date
2020

Document Version
Final published version

Citation (APA)
de Bruijckere, J. (2020). *Correlated Spin Phenomena in Molecular Quantum Transport Devices*. [Dissertation (TU Delft), Delft University of Technology]. https://doi.org/10.4233/uuid:9e3a8b94-87b4-4167-a80c-8cddec3ae58e

CORRELATED SPIN PHENOMENA IN MOLECULAR QUANTUM TRANSPORT DEVICES

CORRELATED SPIN PHENOMENA IN MOLECULAR QUANTUM TRANSPORT DEVICES

Proefschrift

ter verkrijging van de graad van doctor
aan de Technische Universiteit Delft,
op gezag van de Rector Magnificus prof.dr.ir. T.H.J.J. van der Hagen
voorzitter van het College voor Promoties,
in het openbaar te verdedigen op maandag 15 juni 2020 om 10:00 uur

door

Joeri DE BRUIJCKERE

Master of Science in Applied Physics, Technische Universiteit Delft, Nederland
geboren te Oostburg, Nederland

Dit proefschrift is goedgekeurd door de promotor

Samenstelling promotiecommissie bestaat uit:

Rector Magnificus,	voorzitter
Prof.dr.ir. H.S.J. van der Zant	Technische Universiteit Delft, promotor

Onafhankelijke leden:

Prof.dr. J.I. Pascual	CIC nanoGUNE, Spanje
Dr. R. Aguado	Instituto de Ciencia de Materiales de Madrid, Spanje
Dr. A.R. Akhmerov	Technische Universiteit Delft
Prof.dr. J. Nygård	University of Copenhagen, Denemarken
Prof.dr. A.F. Otte	Technische Universiteit Delft
Prof.dr. M.R. Wegewijs	RWTH Aachen University, Duitsland
Prof.dr. Y.M. Blanter	Technische Universiteit Delft, reservelid

Keywords: Quantum transport, single-molecule devices, correlated spin phenomena, Kondo effect, hybrid superconducting devices

Printed by: Gildeprint, Enschede

Front & Back: Schematic representation of a charge-stability diagram of a superconducting single-molecule device showing Coulomb blockade and Yu-Shiba-Rusinov states

Casimir PhD Series, Delft-Leiden 2020-14

ISBN 978-90-8593-441-7

An electronic version of this dissertation is available at
http://repository.tudelft.nl/.

Contents

Summary vii

Samenvatting ix

1 Introduction 1
- 1.1 Nanoscale electronics . . . 2
- 1.2 Contacting a single molecule . . . 4
  - 1.2.1 Mechanically-controlled break junctions . . . 4
  - 1.2.2 Scanning tunneling microscopy . . . 5
  - 1.2.3 Electromigration break junctions . . . 5
- 1.3 Superconducting electrodes . . . 7
- 1.4 Thesis outline . . . 7

2 Theoretical Concepts 11
- 2.1 Sequential electron tunneling . . . 12
- 2.2 Cotunneling . . . 14
- 2.3 The Kondo effect . . . 14
- 2.4 The proximity effect . . . 15
  - 2.4.1 Pair potential and pair amplitude . . . 16
  - 2.4.2 Proximity effect by Andreev reflections . . . 16
  - 2.4.3 Modified local density of states . . . 17
  - 2.4.4 Proximitized tunnel junctions . . . 19
- 2.5 Multiple Andreev reflections . . . 20
- 2.6 Subgap bound states . . . 21
  - 2.6.1 Proximity-induced bound states . . . 21
  - 2.6.2 Yu-Shiba-Rusinov states . . . 21

3 Molecular Double-Spin Systems 27
- 3.1 Radical Molecules as Model Spin Systems . . . 28
- 3.2 The Singlet-Triplet Kondo Effect . . . 33
- 3.3 Anomalous temperature dependence of the singlet-triplet Kondo effect . . . 36
- 3.4 Signatures of a two-stage Kondo effect . . . 37
- 3.5 Concluding remarks . . . 39

4 Molecular Triple-Spin Systems 45
- 4.1 Charging the diradical molecule . . . 46
- 4.2 Two-spin system — Singlet ground state . . . 48
- 4.3 Three-spin system — Doublet ground state . . . 50
- 4.4 Exchange coupling analysis . . . 50
- 4.5 Concluding remarks . . . 55

5 Ground-State Spin Blockade in a Single-Molecule Junction 59
5.1 Blockades in quantum transport . . . 60
5.2 Measurement description . . . 61
5.3 Suppression of linear conductance . . . 61
5.4 Spin ground-state transition . . . 63
5.5 Magnetic-field dependence . . . 64
5.6 Molecular spin structure . . . 66
5.7 Concluding remarks . . . 67
5.8 Appendix A — Experimental details . . . 68
5.9 Appendix B — Model calculations . . . 68
5.9.1 Simulation of the spin-excitation spectra in N-1 . . . 68
5.9.2 Tunability of the parabolic ground-state transition line . . . 68
5.9.3 Model calculation of ground-state spin blockade . . . 69
5.10 Appendix C — Additional data . . . 73
5.10.1 Magnetic-field dependence of the dI/dV spectrum in N . . . 73
5.10.2 Magnetic-field evolution of stability diagrams . . . 75

6 Superconducting Single-Molecule Devices 81
6.1 Lead electrodes . . . 82
6.1.1 Deposition of lead . . . 83
6.1.2 Electromigration of lead constrictions . . . 83
6.1.3 Tunnel spectra of lead junctions . . . 85
6.2 Aluminum electrodes . . . 87
6.2.1 Deposition of aluminum . . . 87
6.2.2 Electromigration of aluminum constrictions . . . 88
6.2.3 Transport through aluminum junctions . . . 89
6.3 Molybdenum rhenium electrodes . . . 89
6.4 Niobium titanium nitride electrodes . . . 92
6.4.1 Deposition of NbTiN . . . 92
6.4.2 Tunnel spectra of NbTiN junctions . . . 93
6.4.3 Single-level impurity in a NbTiN device . . . 95
6.5 Concluding remarks . . . 99

7 Superconducting InAs/Pb Nanowire Island Devices 105
7.1 Device description . . . 106
7.2 Coulomb-blockade spectroscopy . . . 107
7.3 Analysis of the Coulomb-peak spacing . . . 110
7.4 Concluding remarks . . . 112

8 Conclusion and outlook 115

Acknowledgements 121

Curriculum Vitæ 123

List of Publications 125

SUMMARY

In this thesis we study charge transport through individual molecules and mainly focus on the properties of molecular spin. We fabricate nanoscale structures for transport measurements and employ the electromigration break-junction technique to realize three-terminal — transistor-like — single-molecule devices. We investigate the spin-related phenomena that occur in these devices by performing transport experiments.

In Chapter 3 we study a molecular two-spin system, realized by embedding a diradical molecule in a tunnel junction. We probe the spin excitations of this molecule by inelastic electron tunneling spectroscopy (IETS) and observe transitions between the singlet state and the triplet states. The IETS measurements are in excellent agreement with simulations of a basic cotunneling model of two exchange-coupled spins, which demonstrates the model two-spin behavior of the diradical molecule. Subsequent measurements focus on the experimental observation of the singlet-triplet Kondo effect, which occurs at a magnetic-field-induced degeneracy of the singlet state and one of the triplet states. We find that the associated Kondo resonance exhibits an anomalous temperature dependence and we provide a plausible explanation for this behavior by considering an anisotropic exchange coupling between the spins of the diradical molecule. Next, we present measurements consistent with the emergence of an exotic Kondo effect known as the two-stage Kondo effect. Magnetic-field-dependent transport measurements show the subsequent breakdown of the two stages of Kondo screening in this device.

The same kind of diradical molecule is used for the measurements presented in Chapter 4, where we focus on one single-molecule device which could be electrostatically reduced to obtain a system with three unpaired spins. We demonstrate the three-spin behavior by probing the associated spin-multiplet excitations by IETS, which include transitions between two distinct doublet states and between the doublet ground state and an excited quartet state. We show that it is impossible to determine the values of the three associated exchange couplings based on the excitation energies alone and propose a complementary procedure to obtain this information by measuring the relative step height of the excitations and comparing these values to a cotunneling model.

In Chapter 5 we focus on a different molecule which exhibits a rarely-observed blockade phenomenon referred to as ground-state spin blockade. The molecule is a polyoxometalate featuring a high-spin Mn-ion core. Charge transport in this device occurs mainly through a ligand orbital which is exchange-coupled to the high-spin core. We find that the sign of the associated exchange coupling flips when an electron is electrostatically added to the Mn core. Due to this sign flip the spin difference between the ground states of adjacent charge states is larger than the spin of a single electron. Low-energy electrons are therefore not allowed to occupy the molecule due to the spin-selection rules. We show that the ground-state spin blockade can be lifted by applying an external magnetic field. At high magnetic field the ground state in one of the charge

states changes from a low-spin state to a high-spin state, thereby lowering the spin difference with the ground state of the adjacent charge state to 1/2.

The previous chapters all involved single-molecule devices with normal-metal electrodes. In Chapter 6 we focus on the development of superconducting single-molecule devices and present preliminary transport measurements using these devices. We respectively discuss the materials aluminum, lead, molybdenum rhenium (MoRe) and niobium titanium nitride (NbTiN). Both intrinsically superconducting electrodes as well as proximity-induced superconducting electrodes are considered. We find NbTiN to be the most promising material for this research and present detailed transport measurements of a single-level system coupled to NbTiN-based proximity-induced superconducting electrodes. Even though the nature of the single-level system is unclear, the measurements display signatures of the phenomena that are envisioned to be studied with this type of device, including multiple Andreev reflections, Yu-Shiba-Rusinov states and Josephson currents.

Chapter 7 is not about molecules, but focuses on transport measurements of a novel hybrid semiconductor-superconductor nanowire with epitaxial lead (Pb). We present measurements of a superconducting island device using this nanowire and demonstrate the $2e$ quantization of charge. By increasing the external magnetic field we observe a gradual transition from $2e$ charge quantization to an even-odd regime to $1e$ charge quantization. As this transition occurs well below the critical field we attribute the doubling of the periodicity to the opening of transport channels through zero-energy bound states. Observed oscillations of the Coulomb-peak spacings resemble the oscillations seen in aluminum-based devices as a result of the hybridization of Majorana modes. These observations in combination with the high critical magnetic field, high critical temperature and large superconducting gap make this novel nanowire device a promising platform for future studies on topological superconductivity.

SAMENVATTING

In deze thesis bestuderen we ladingstransport door individuele moleculen en focussen we in het bijzonder op de eigenschappen van moleculaire spin. We fabriceren nanostructuren voor transportmetingen en maken gebruik van geëlektromigreerde breekjuncties om transistor-achtige apparaten met een enkel molecuul te realizeren. We onderzoeken de spin-gerelateerde fenomenen die ontstaan in deze apparaten met behulp van transportmetingen.

In Hoofdstuk 3 bestuderen we een moleculair systeem met twee spins door een diradicaalmolecuul te integreren in een tunneljunctie. We meten de spinexcitaties van dit molecuul met behulp van inelastische elektron tunnelspectroscopie (IETS) waarmee we transities zien tussen de singlettoestand en de triplettoestanden. De IETS-metingen zijn in goede overeenkomst met simulaties van een eenvoudig tunnelmodel van twee spins gekoppeld door uitwisselingsinteracties. Deze overeenkomst laat zien dat het diradicaalmolecuul zich als een modelsysteem met twee spins gedraagt. Vervolgmetingen focussen op de observatie van het singlet-triplet Kondo-effect, wat plaatsvindt bij een magneetveld-geïnduceerde ontaarding van de singlettoestand en één van de triplettoestanden. We observeren dat de daarbij behorende Kondo-resonantie een afwijkende temperatuursafhankelijkheid laat zien en we geven een mogelijke verklaring voor dit gedrag door een anistropische uitwisselingsinteractie te beschouwen. Vervolgens presenteren we metingen die consistent zijn met de verschijning van een exotisch Kondo-effect dat bekend staat als het twee-stadia Kondo-effect. Magneetveld-afhankelijke metingen laten de stapsgewijze suppressie van de twee stadia van het Kondo-effect zien.

Hetzelfde type diradicaalmolecuul is gebruikt voor de transportmetingen gepresenteerd in Hoofdstuk 4, waar we focussen op één apparaat met een enkel molecuul dat we elektrostatisch konden reduceren tot een systeem met drie ongepaarde spins. We demonstreren het drie-spingedrag door de bijbehorende spinexcitaties te onderzoeken met behulp van IETS. We observeren transities tussen twee verschillende doublettoestanden en een geëxciteerde kwartettoestand. We laten zien dat het niet mogelijk is om de drie uitwisselingskoppelingen van dit systeem te bepalen op basis van alleen de excitatie-energieën. We stellen een complementaire procedure voor om meer informatie over dit systeem te weten te komen door de staphoogte van de excitaties te vergelijken met een tunnelmodel.

In Hoofdstuk 5 focussen we op een ander type molecuul dat een zeldzaam transportblokkadefenomeen laat zien, genaamd grondtoestand-spinblokkade. Het molecuul is een polyoxometalaat met een magnesium-ion kern met een hoge spin. Ladingstransport in dit apparaat vindt voornamelijk plaats door een ligandorbitaal die gekoppeld is aan de molecuulkern door uitwisselingsinteracties. We observeren een verandering in het teken van de uitwisselingskoppeling wanneer een elektron elektrostatisch wordt toegevoegd aan de molecuulkern. Deze verandering heeft als gevolg dat het spinverschil tussen de

grondtoestanden van aangrenzende ladingstoestanden groter is dan de spin van een enkel elektron. Elektronen met lage energie kunnen daardoor niet het molecuul bezetten als gevolg van de spinselectieregels. We laten zien dat de grondtoestand-spinblokkade opgeheven kan worden met een extern magnetisch veld. Bij hoog magneetveld verandert de grondtoestand van één van de ladingstoestanden van een lage spintoestand naar een hoge spintoestand waardoor het spinverschil met de grondtoestand van de aangrenzende ladingstoestand 1/2 wordt.

De voorgaande hoofdstukken hadden allemaal betrekking op apparaten met een enkel molecuul en elektroden van normaal metaal. In Hoofdstuk 6 focussen we op de ontwikkeling van supergeleidende apparaten met een enkel molecuul en presenteren we de eerste transportmetingen waarvoor we deze apparaten gebruiken. Respectievelijk bespreken we de materialen lood, aluminium, MoRe en NbTiN. Zowel intrinsiek supergeleidende elektroden als nabijheidsgeïnduceerde supergeleidende elektroden worden beschoud. We bevinden dat NbTiN het meest veelbelovende materiaal is voor dit onderzoek en presenteren transportmetingen van een systeem met een enkel energyniveau gekoppeld aan nabijheidsgeïnduceerde supergeleidende elektroden met NbTiN. Ook al is het niet bekend waaruit het systeem met een enkel energieniveau bestaat, de metingen laten kenmerken zien van de fenomenen die we willen bestuderen met dit type apparaat, zoals meervoudige Andreev-reflecties, Yu-Shiba-Rusinov-toestanden en Josephson-stroom.

Hoofdstuk 7 gaat niet over moleculen, maar over transportmetingen van een nieuw type hybride halfgeleider-supergeleider nanodraad met epitaxiaal lood. We laten metingen zien van een supergeleidend-eiland-apparaat bestaande uit deze nanodraad en we demonstreren $2e$-ladingskwantisatie. Door het magneetveld te verhogen zien we een geleidelijke overgang van de $2e$-ladingskwantisatie naar een even-oneven-regime en vervolgens naar $1e$-ladingskwantisatie. Aangezien deze overgang ver onder het kritische magneetveld plaatsvindt, schrijven we de verdubbeling van de periodiciteit toe aan het openen van transportkanalen door gebonden toestanden met nul energie. We observeren oscillaties in de afstanden tussen de Coulomb-pieken, vergelijkbaar met de oscillaties geobserveerd in nanodraden met aluminium als gevolg van de hybridisatie van Majorana-toestanden. Deze resultaten in combinatie met het hoge kritische magneetveld, de hoge kritische temperatuur en het grote supergeleidende gat, maken dit nieuwe nanodraadsysteem een veelbelovend platform voor toekomstige metingen met betrekking tot topologische supergeleiding.

1

INTRODUCTION

In this first chapter we introduce the research topics of this thesis. We start from the common ground and gradually zoom in on the scientific context of single-molecule charge-transport studies. We give a brief overview of the experimental techniques that can be used to contact a single molecule with conducting and superconducting electrodes, and motivate why we use the electromigration break-junction technique for this research. Thereafter, we provide a brief outline of this thesis.

1

This thesis is in essence a collection of studies about electricity, or charge transport, at the nanoscale. Traditionally, in the context of electricity it is common to draw an analogy between electric current in a circuit and water flowing through a water pipe. In this analogy, charge is equivalent to water, electric current is the amount of water flowing through the pipe per unit time, and the voltage is the height difference between the two ends of the pipe. Similarly, a resistor in an electric circuit may be seen as a constriction in the water pipe, which suppresses water flow. This picture provides sufficient intuition to grasp the most famous law of electricity, Ohm's law — $I = V/R$, where I is the current, V the voltage and R the resistance. Ohm's law accurately describes the relation between the basic quantities of most electronic circuits — at least for those large enough to be seen with bare eyes. On the macroscopic scale, it is easy to forget that the electric current is in fact carried by individual particles, *electrons* — much like the H_2O molecules in a water stream. One could easily be a very successful electrical engineer without even knowing about electrons or believing in them!

Due to technological advances over the years we have been able to create electric circuits at increasingly smaller scales, cramming as much electronic components as possible in our everyday devices — making them ever more functional. This miniaturization of electronics is described by Moore's law, which predicts that every two years the density of transistors on a chip doubles [1]. As a result, the discrete nature of charge is playing an increasingly important role. Down to the nanoscale, classical laws no longer apply and the physics of charge transport can better be described by quantum theory. In this thesis we experimentally study extremely small electronic devices, which operate exclusively within the quantum realm — perhaps needless to say, Ohm's law does not apply here!

1.1. NANOSCALE ELECTRONICS

As electronic components are getting smaller and smaller, at some point a fundamental limit is reached: the limit of single *atoms*. The smallest structures that are made out of atoms are called *molecules*. It is those elementary structures which are at the core of the devices studied in this thesis. Using individual molecules in commercial electronic devices is not a reality yet, and will probably not be for many years to come — if at all. The scalability, reproducibility and operability of single-molecule components is far from being sufficient for any commercial application. Nevertheless, they are of great interest to fundamental science. Even if there may not be an obvious application for single-molecule components with current technology, the gained knowledge and developed theoretical models from single-molecule experiments can be of great importance in future developments of nanoscale electronics.

Due to their extremely small size, individual molecules are ideal systems for studying unexplored physical phenomena at the nanoscale. With a typical size of the order of 1 nm, the electrostatic repulsion between electrons in a single molecule is particularly strong. This repulsion can be quantified by the charging energy, E_C. Whereas the charging energies of other quantum systems — such as semiconductor quantum dots and carbon nanotubes — is typically not higher than a few meV, in single molecule devices $E_C > 100$ meV [2]. As a result, molecular devices effectively behave as single-level sys-

tems, making them ideal platforms for studying quantum transport effects and comparing theoretical models with experimental data. In addition, by chemical design, structurally perfect molecules can be created with unique properties, chemically tailored for a wide range of studies.

Most experimental data presented in this thesis focus in one way or another on a quantum-mechanical property called *spin*. Spin is known as the intrinsic angular momentum of an elementary particle. Whereas the other type of angular momentum — the *orbital* angular momentum — also appears in classical mechanics, spin does not have a classical counterpart. The spin of an elementary particle is a degree of freedom which only takes discrete values — much like electric charge. The number of different spin states a particle can have depends on its spin quantum number, s, and is equal to $2s+1$. For an electron, $s = 1/2$, which means it can have two spin states, traditionally called spin up and spin down. The two spin states have opposite magnetic moments, so they interact differently in a magnetic field. For example, an isolated electron in a magnetic field can have a lower energy in its spin-up state than in its spin-down state.

Various devices that rely on the spin degree of freedom already exist, including magnetic resonance imaging (MRI) scanners and giant magnetoresistive (GMR) hard-disk drive heads, but also many potential applications are still in the early development stages. Of specific interest here are the fields of spintronics and quantum computing, as these fields are most closely related to the topic of this thesis. In spintronics, one uses — apart from the charge — also the spin degree of freedom to realize more efficient electronic devices. For example, in contrast to electric currents, spin currents do not require the transfer of particles, which results in lower energy losses. Quantum computing relies on the use of quantum-mechanical phenomena, such as superposition and entanglement, to perform specific computational tasks much faster than any classical computer ever could. Instead of classical bits, a quantum computer consists of *qubits*, which can be realized in many forms. Spin qubits are just one example.

For many of the envisioned applications it is crucial to understand the fundamental principles of how spins behave. Isolated spins and spin clusters are already fairly well understood. However, when a spin is embedded in an electric circuit it starts to interact with many other particles, which may result in the emergence of complex many-body phenomena. One famous example is the Kondo effect, which will be discussed in Chapters 2 to 4. The Kondo effect is the emergence of a strongly-coupled bound state between a localized spin — residing on a molecule for instance — and the spins of nearby conduction electrons due to magnetic scattering. In theoretical physics, the Kondo effect has attracted tremendous interest since its first description in 1964 [3]. The seemingly simple problem that Kondo formulated, turned out to be extremely difficult to solve and has led to the development of various theoretical techniques, such as Wilson's numerical renormalization group [4]. In the understanding of these complex phenomena, theory and experiment go hand in hand, as one motivates the other to find pieces of the same puzzle. Throughout this thesis, we focus on experimental observations of spin-related phenomena in single-molecule transport devices with increasing complexity. Where possible, we interpret the measured data based on known theoretical models, and speculate about observations that we could not definitively explain, in the hope that this may motivate future studies. The conducted single-molecule transport experiments heavily

rely on the ability to embed a single molecule in an electric circuit, which is not a trivial task as will be discussed next.

1.2. CONTACTING A SINGLE MOLECULE

The typical size of molecules in charge-transport experiments is of the order of 1 nm, orders of magnitude smaller than what any tweezers or other common manipulation tools can handle. In fact, very few techniques exist that are capable of contacting molecules to conducting electrodes on an individual level. Here, we give an overview of the three main techniques that have been successfully used for this purpose, along with a discussion of their advantages and disadvantages. We first describe the mechanical break junction technique, conceptually the simplest of the three. Then, we focus on using a scanning tunneling microscope to contact individual molecules, and finally we describe the technique used throughout this thesis: creating molecular junctions by electromigration break junctions.

1.2.1. MECHANICALLY-CONTROLLED BREAK JUNCTIONS

A mechanically-controlled break junction (MCBJ) consists of a metallic nanowire connected to macroscopic leads on top of a flexible substrate [5]. The nanowire can be mechanically broken with a high degree of control by bending the substrate using high-precision actuators. In this way, the nanowire — typically made of gold — can be gradually stretched to the point of breaking. Just before the wire breaks an atomic point contact may form between the two leads, which can be verified by conductance measurements. In the case of a single-atom gold contact, the conductance, G, is approximately equal to the conductance quantum, $G_0 = 2e^2/h \approx 77\,\mu\text{S}$. By stretching the nanowire even further, the atomic contact breaks and a tunnel junction ($G \ll G_0$) with atomically sharp leads may form. In order to realize a molecular junction with this technique, the whole device is initially submerged in a dilute solution of the molecule being studied. The solvent is pumped away using a mechanical pump, ideally leaving a (sub)mono-layer of molecules on the surface of the gold nanowire. Upon breaking the wire to the tunneling regime, a single molecule may be trapped between the two leads such that a single-molecule junction is formed. Forming a molecular junction in this way is a stochastic process and one relies on many breaking events to draw reliable conclusions about the experiment. Whether a molecule is trapped can typically be determined from the decay of the current as a function of the separation between the leads. When there is no molecule in the junction this decay is exponential — as is the case for any bare tunnel junction. The observation of an initial non-exponential decay over a certain distance may be due to a molecular junction being formed.

Already for many years, the MCBJ technique has been successfully used to study the conducting properties of single molecules [6]. The technique stands out due to its simplicity, enabling fast characterization both at room temperature and at low temperatures. The simplicity of the technique also reflects its limitations. For one, MCBJs typically only have two leads. Although MCBJs with an additional *gate electrode* have been developed [7, 8], the gate efficiency is low and these devices are therefore limited in their ability to tune the energy levels of the molecule and reversibly change the charge state

of the molecule. This restricts the spectroscopic abilities of the MCBJ technique compared to the electromigration break junction technique, which does allow for a stable gate electrode with a relatively high gate coupling, as discussed in Section 1.2.3.

1.2.2. SCANNING TUNNELING MICROSCOPY

Another limitation of the MCBJ technique is the availability of only one mechanical degree of freedom — the substrate bending. In scanning tunneling microscopy (STM), one of the leads, the STM tip, can move with very high precision in *all* directions over a conducting surface. The STM technique relies on the aforementioned exponential decay of the tunneling current with distance, where the distance in this case is the height of the STM tip relative to the substrate. By keeping the current constant using a fast feedback loop, a fixed height can be maintained. Upon scanning the surface, objects such as atoms and molecules can be detected by changes in the tunneling current. In this way, one can scan the surface for molecules and position the STM tip at the desired location before starting a spectroscopic measurement. The first conductance measurements of single molecules were made in this way using the STM technique [9, 10]. As the height of the STM tip can be controlled with great precision, the technique can be used in a range of transport regimes. For instance, the tip can be placed far away from the molecule of interest to probe it deep within the tunneling regime. Or it can operate in the opposite regime, by indenting the STM tip into the surface and slowly retracting it to form a strongly-coupled molecular junction [11], similar to the MCBJ technique. Despite the high degree of control, also STM lacks the possibility of having an electrostatically-coupled gate electrode, which for various studies makes the electromigration break junction technique more suitable, as discussed in the following section.

1.2.3. ELECTROMIGRATION BREAK JUNCTIONS

Electromigration is the process in which the ions in a solid move as a result of an electric field. Two mechanism are responsible for this movement: The direct electrostatic interaction between the electric field and the ions, and the momentum exchange between the ions and the conduction electrons. Although in most electronic devices electromigration is an undesired effect, it can be used in a controlled way to create nanometer-sized gaps in conducting nanowires in which single molecules can be trapped [12].

The process of creating a molecular junction by electromigration starts with a conducting nanowire at room temperature connected to a voltage source. The bias voltage over the wire is increased, such that the current density in the wire increases. At a certain bias voltage, the current density is so high that the ions start to migrate, which leads to a narrowing of the wire and eventually rupture. In this process, the conductance of the wire is monitored and the bias voltage is controlled using a fast feedback-loop to ensure a gradual breaking of the wire [13]. As soon as the conductance is of the order of the conductance quantum, G_0, the bias voltage is removed. The conductance quantum is the maximum conductance of a single channel and therefore corresponds to a constriction of only one or a few atoms in width. After the electromigration process, the junction is left without a bias voltage at room temperature. The continuous rearrangement of the atoms in the constriction can lead to the self-breaking of the wire [14], ideally resulting

in a nanometer-sized tunnel junction in which a molecule can become trapped.

Before electromigration, a dilute solution of the studied molecules is deposited on the substrate. This solution is pumped out after the formation of the nanogaps, leaving single molecules trapped in some of the junctions. Alternatively, the electromigration is first performed in vacuum, after which the vacuum is temporarily broken to deposit the solution of the molecules. To verify the presence of a molecule, transport measurements are performed as a function of the gate voltage. Conductance peaks in these gate-dependent measurements could correspond to charge transitions of a single molecule in the junction. The presence of a molecule in the junction could be corroborated by targeted subsequent measurements. For example, a non-linear magnetic-field dependence of the conductance peaks corroborates the presence of a molecule with magnetic anisotropy [15]. As is the case for MCBJs, contacting molecules by the electromigration break-junction technique is a stochastic processes. For this reason, many electromigration break junctions are patterned on a chip to increase the chances of trapping a single molecule. In order to decrease the probability of trapping multiple molecules in the same junction, the concentration of the solution is optimized to obtain molecular signatures in roughly ten percent of the junctions — leaving the other electromigrated junctions to be empty tunnel junctions.

Electromigrated molecular junctions have the unique possibility of being equipped with a gate electrode. In the transistor-like configuration obtained in this way it is possible to tune between off-resonant transport and resonant transport, as one can electrostatically shift the discrete energy levels of the molecule with respect to the electrochemical potential of the leads by the gate voltage. Other techniques for probing individual molecules lack this possibility and are typically limited to the off-resonant transport regime of a single charge state. In addition, several studies in this thesis involve the Kondo effect, whose associated energy scale — the Kondo temperature — can be tuned by the gate voltage [2]. Similarly, the energy of Yu-Shiba-Rusinov bound states can be shifted by the gate voltage, as discussed in Chapter 6. The gate electrode thus provides an additional level of control in single-molecule experiments, not yet available by other techniques.

Electromigration single-molecule devices are almost exclusively made from gold because of its advantageous properties. Due to its single outer s-orbital electron, gold is known to behave as a Fermi-gas-like metal with a flat density of states around the Fermi level. This is desired in conductance spectroscopy, where ideally the influence of the electrodes on the measurements is negligible. In addition, gold is significantly less reactive than other metals and is therefore more likely to form pristine atomic contacts. Finally, the relatively high mobility of gold atoms facilitates controlled electromigration at room temperature, which is crucial for realizing nanometer-sized tunnel junctions. Despite all the benefits, gold is not suitable for every single molecule study. For example, for superconducting single-molecule devices, which will be discussed in the next section, other materials are needed since gold does not become superconducting at low temperatures.

1.3. SUPERCONDUCTING ELECTRODES

In a superconductor, electrons are bound in pairs, known as Cooper pairs. These bound pairs have the remarkable property of behaving as one single entity — all Cooper pairs are part of one and the same quantum-mechanical ground state. In order to break a Cooper pair one has to perturb not only that pair, but the whole condensate. This gives rise to the superconducting gap, Δ, which is the energy required to remove an electron from the superconducting condensate. In a nano-object like a semiconductor quantum dot or a single molecule, transport is typically governed by single electrons. In a superconductor on the other hand, transport occurs by the collective motion of Cooper pairs. It is therefore interesting to investigate how superconducting transport through a non-superconducting nano-object works. The ability to combine a nano-object with superconducting electrodes opens up the possibility to study transport in a regime where single-electron effects and many-body phenomena compete [16].

Over the past years it has been made possible to embed non-superconducting nanostructures in a superconducting device. These hybrid superconducting devices include the use of semiconductor nanowires [17], carbon nanotubes [18] and individual C_{60} molecules [19]. So far, research in this field has been mainly focused on semiconductor quantum dots, leaving superconducting transport through single molecules a largely unexplored research topic. The main differences between a single molecule and other nano-objects are the exceptionally high charging energy, which effectively renders it a single-level system, and the possibility to chemically build in properties such as magnetic anisotropy and high-spin states. From a fundamental physics point of view, it seems very interesting to study the interaction between these unique properties of single molecules and superconducting electrodes. In STM probing molecules with superconducting electrodes has already been achieved [20], although the absence of a gate electrode limits the tunability of these studies, which are therefore typically restricted to the off-resonant transport regime. For this reason we developed superconducting single-molecule devices with an added gate electrode, as described in Chapter 6. We make use of the well-established electromigration break-junction technique and further develop this technique to enable the use of superconducting electrodes. As will be shown, the gate electrode plays an important role in studying one of the hot topics in the field in hybrid superconducting devices: the emergence of Yu-Shiba-Rusinov bound states.

1.4. THESIS OUTLINE

In the following chapter of this thesis, Chapter 2, we briefly discuss some of the theoretical concepts which are relevant for the understanding of the transport data. The experimental chapters that follow are presented in order of their complexity. In Chapters 3 and 4 we present the results of charge-transport measurements of a specific type of molecule: an all-organic diradical molecule. This molecule typically behaves as a two-spin system as will be shown in Chapter 3. In Chapter 4 we focus on one device with the same type of diradical molecule, which we were able to electrostatically charge to obtain a three-spin system. The topic of Chapter 5 is ground-state spin blockade, a rarely observed transport-blockade phenomenon, which is measured using a polyoxometalate (POM) molecule. All the aforementioned studies make use of normal metal electrodes.

In Chapter 6 instead, we focus on the development of single-molecule devices with superconducting leads, and show preliminary transport measurements of these devices. Chapter 7 is the only chapter where the nano-object is not a molecule, but a novel hybrid semiconductor-superconductor nanowire. We present transport measurements of a superconducting 'island' device using this nanowire. Finally, in Chapter 8 we end with concluding remarks and discuss future research directions.

REFERENCES

[1] G. E. Moore. “Cramming more components onto integrated circuits”. *Electronics* 38.8 (Apr. 19, 1965).

[2] J. M. Thijssen and H. S. J. van der Zant. “Charge transport and single-electron effects in nanoscale systems”. *physica status solidi (b)* 245.8 (Aug. 2008), pp. 1455–1470. DOI: 10.1002/pssb.200743470.

[3] J. Kondo. “Resistance Minimum in Dilute Magnetic Alloys”. *Progress of Theoretical Physics* 32.1 (July 1964), pp. 37–49. DOI: 10.1143/ptp.32.37.

[4] K. G. Wilson. “The renormalization group: Critical phenomena and the Kondo problem”. *Reviews of Modern Physics* 47.4 (Oct. 1975), pp. 773–840. DOI: 10.1103/revmodphys.47.773.

[5] C. Zhou, C. J. Muller, M. R. Deshpande, J. W. Sleight, and M. A. Reed. “Microfabrication of a mechanically controllable break junction in silicon”. *Applied Physics Letters* 67.8 (Aug. 1995), pp. 1160–1162. DOI: 10.1063/1.114994.

[6] M. A. Reed. “Conductance of a Molecular Junction”. *Science* 278.5336 (Oct. 1997), pp. 252–254. DOI: 10.1126/science.278.5336.252.

[7] A. R. Champagne, A. N. Pasupathy, and D. C. Ralph. “Mechanically Adjustable and Electrically Gated Single-Molecule Transistors”. *Nano Letters* 5.2 (Feb. 2005), pp. 305–308. DOI: 10.1021/nl0480619.

[8] M. L. Perrin, C. J. O. Verzijl, C. A. Martin, A. J. Shaikh, R. Eelkema, J. H. van Esch, J. M. van Ruitenbeek, J. M. Thijssen, H. S. J. van der Zant, and D. Dulić. “Large tunable image-charge effects in single-molecule junctions”. *Nature Nanotechnology* 8.4 (Mar. 2013), pp. 282–287. DOI: 10.1038/nnano.2013.26.

[9] C. Joachim, J. K. Gimzewski, R. R. Schlittler, and C. Chavy. “Electronic Transparence of a Single C_{60} Molecule”. *Physical Review Letters* 74.11 (Mar. 1995), pp. 2102–2105. DOI: 10.1103/physrevlett.74.2102.

[10] L. A. Bumm, J. J. Arnold, M. T. Cygan, T. D. Dunbar, T. P. Burgin, L. Jones, D. L. Allara, J. M. Tour, and P. S. Weiss. “Are Single Molecular Wires Conducting?” *Science* 271.5256 (Mar. 1996), pp. 1705–1707. DOI: 10.1126/science.271.5256.1705.

[11] B. Xu. “Measurement of Single-Molecule Resistance by Repeated Formation of Molecular Junctions”. *Science* 301.5637 (Aug. 2003), pp. 1221–1223. DOI: 10.1126/science.1087481.

[12] H. Park, A. K. L. Lim, A. P. Alivisatos, J. Park, and P. L. McEuen. “Fabrication of metallic electrodes with nanometer separation by electromigration”. *Applied Physics Letters* 75.2 (July 1999), pp. 301–303. DOI: 10.1063/1.124354.

[13] J. M. Campbell and R. G. Knobel. “Feedback-controlled electromigration for the fabrication of point contacts”. *Applied Physics Letters* 102.2 (Jan. 2013), p. 023105. DOI: 10.1063/1.4775695.

[14] K. O’Neill, E. A. Osorio, and H. S. J. van der Zant. “Self-breaking in planar few-atom Au constrictions for nanometer-spaced electrodes”. *Applied Physics Letters* 90.13 (Mar. 2007), p. 133109. DOI: 10.1063/1.2716989.

[15] E. Burzurí, A. S. Zyazin, A. Cornia, and H. S. J. van der Zant. “Direct Observation of Magnetic Anisotropy in an Individual Fe_4 Single-Molecule Magnet”. *Physical Review Letters* 109.14 (Oct. 2012). DOI: 10.1103/physrevlett.109.147203.

[16] S. D. Franceschi, L. P. Kouwenhoven, C. Schönenberger, and W. Wernsdorfer. “Hybrid superconductor-quantum dot devices”. *Nature Nanotechnology* 5.10 (Sept. 2010), pp. 703–711. DOI: 10.1038/nnano.2010.173.

[17] Y.-J. Doh, J. A. van Dam, A. L. Roest, E. P. A. M. Bakkers, L. P. Kouwenhoven, and S. D. Franceschi. “Tunable Supercurrent Through Semiconductor Nanowires”. *Science* 309.5732 (July 2005), pp. 272–275. DOI: 10.1126/science.1113523.

[18] P. Jarillo-Herrero, J. A. van Dam, and L. P. Kouwenhoven. “Quantum supercurrent transistors in carbon nanotubes”. *Nature* 439.7079 (Feb. 2006), pp. 953–956. DOI: 10.1038/nature04550.

[19] C. B. Winkelmann, N. Roch, W. Wernsdorfer, V. Bouchiat, and F. Balestro. “Superconductivity in a single-C_{60} transistor”. *Nature Physics* 5.12 (Oct. 2009), pp. 876–879. DOI: 10.1038/nphys1433.

[20] K. J. Franke, G. Schulze, and J. I. Pascual. “Competition of Superconducting Phenomena and Kondo Screening at the Nanoscale”. *Science* 332.6032 (May 2011), pp. 940–944. DOI: 10.1126/science.1202204.

2

THEORETICAL CONCEPTS

In this chapter we discuss various theoretical concepts which are relevant in the interpretation of the charge-transport measurements presented in this thesis. We describe the basic theory and link the relevant details to the experimental results. We cover electron tunneling processes and their signatures in a quantum-transport experiment, followed by the Kondo effect and the superconducting proximity effect. We conclude by discussing the different types of subgap states that may emerge in superconducting single-molecule devices. For a more elaborate discussion on the various topics we refer to the references in this chapter.

2.1. SEQUENTIAL ELECTRON TUNNELING

The simplest electron tunneling process we discuss is *sequential electron tunneling* (SET). SET is the tunneling of a single electron from an electron reservoir to a nano-object, or *vice versa*. The charge state of the nano-object changes in this process, e.g. from $|N\rangle$ to $|N+1\rangle$ when an electron is added. The added electron changes the spin of the nano-object by $\pm 1/2$. Charge transport by SET is realized when the electron tunneling into the nano-object subsequently tunnels to the other electrode in a second SET event — hence the name sequential electron tunneling. We can write this sequence of SET events as: $|N\rangle \rightarrow |N+1\rangle \rightarrow |N\rangle$. This process is only allowed when the electrochemical potential (or Fermi level) of the first electrode E_{F1} is higher than the electrochemical potential of the nano-object μ_N and the Fermi level of the second electrode E_{F2} is lower than μ_N. The reverse process is also possible, which means that the requirements for SET transport include [1]:

$$E_{F1} \geq \mu_N \geq E_{F2} \quad \text{or} \quad E_{F1} \leq \mu_N \leq E_{F2}. \tag{2.1}$$

These requirements can be met by: (*i*) applying a bias voltage V over the two electrodes, which opens up a bias window between the Fermi levels: $eV = E_{F1} - E_{F2}$, and (*ii*) tuning μ_N inside that bias window by a capacitively-coupled gate electrode. In transport experiments the regime in which Equation (2.1) holds is referred to as the *SET regime*.

Electron transport in the SET regime is schematically depicted in Figure 2.1a, which shows an electrochemical potential scheme with two electron reservoirs filled up to their Fermi levels, E_{F1} and E_{F2}. The electrochemical potential of the nano-object depends on the charge state of the nano-object and is drawn for the charge states $N-1$, N and $N+1$. The arrow indicates a single SET event where one electron tunnels from the left electrode to the nano-object. In a second SET event the electron could tunnel from the nano-object to the right electrode.

Figure 2.1b shows a diagram which indicates the combinations of bias voltage, V, and gate voltage, V_g, for which the requirements in Equation (2.1) are met. In the orange parts of the diagram SET transport can occur, whereas in the blue regions the requirements in Equation (2.1) are not met and electron transport is suppressed by *Coulomb blockade*. The diamond-shaped Coulomb-blockaded regions are known as *Coulomb diamonds*. In every Coulomb diamond the charge of the nano-object is stable at a different value — as indicated by the numbers $N-1$, N and $N+1$ which label the different charge states. In experiments, we refer to these types of (V_g, V) maps as *stability diagrams*.

Excited states of the nano-object can be identified as slanted lines in the SET region of a stability diagram, as indicated by the slanted dashed lines in Figure 2.1b. In the regions above these lines (or for negative V beneath these lines), SET transport not only occurs between the ground states of neighboring charge states, but also involves excited states. For example, the slanted dashed lines on the left in Figure 2.1b correspond to the onset of the process $|N-1\rangle \rightarrow |N_{ex}\rangle \rightarrow |N-1\rangle$, where $|N_{ex}\rangle$ is an excited state. The current can be enhanced or suppressed by introducing this additional transport channel, depending on the rate at which the process occurs [1] — slow SET excitations can suppress the current, which results in lines of negative differential conductance (NDC), as observed e.g. in the experimental data presented in Figure 4.1a.

Equation (2.1) is typically the only requirement of interest for SET transport through a nano-object. In special cases however, additional requirements become relevant such

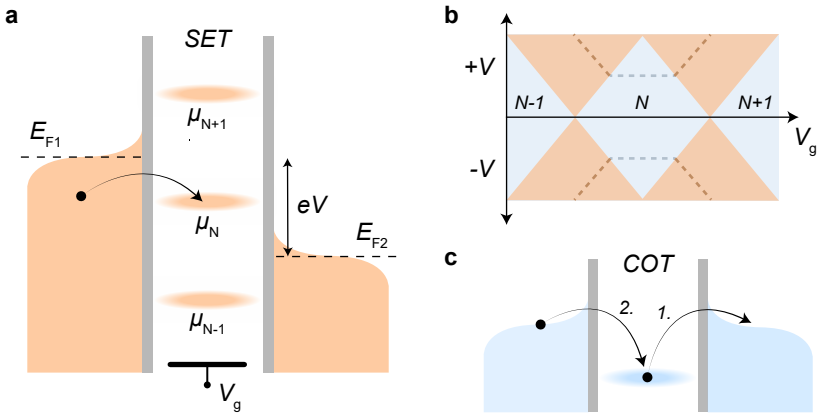

Figure 2.1: a. Electrochemical potential scheme, schematically depicting SET transport. The left and right electrodes are represented by electron reservoirs filled up to their respective Fermi levels, E_{F1} and E_{F2}. The electrochemical potential of the nano-object is drawn for the charge states $N-1$, N and $N+1$. **b.** Schematic stability diagram showing Coulomb-blockaded transport across three charge states, along with a COT excitation line (horizontal dashed line) and the corresponding SET excitation lines (slanted dashed lines). **c.** Schematic representation of elastic COT transport through a nano-object where (*1.*) an electron tunnels from the nano-object to the Fermi level of the right electrode (*2.*) and an electron from the Fermi level of the left electrode tunnels tunnels into the nano-object within a timescale $\sim h/\varepsilon$ where $\varepsilon \equiv E_{F1} - \mu_N$.

as the spin selection rules [1], as will be discussed in Chapter 5. There, we present experimental data of a system for which the difference of the ground-state spin of $|N\rangle$ and $|N+1\rangle$ differs by more than 1/2, such that single electrons cannot realize the transition $|N\rangle \rightarrow |N+1\rangle$ and SET transport involving the two ground states is suppressed.

2.2. COTUNNELING

Outside of the SET regime, i.e., where the requirements in Equation (2.1) are not met, SET events are forbidden and charge transport is largely suppressed (see blue regions in Figure 2.1b). Electrons from one electrode can still reach the other electrode *via* the nano-object through a process known as *cotunneling* (COT). In the simplest form of COT, two electrons are involved in a single COT event. We consider the case where $\mu_N < E_{F1}, E_{F2}$, such that an electron from the nano-object cannot tunnel to the electrodes by an SET event. We refer to the difference between μ_N and E_{F1} (or E_{F2}) as ε. In the case of cotunneling, an electron *can* tunnel into the electrodes, as long as another electron tunnels back into the nano-object within a very short time. Energy conservation is briefly violated in this process, which is quantum-mechanically allowed within a timescale $\sim h/\varepsilon$. A COT event is schematically depicted in Figure 2.1c in which (*1.*) an electron tunnels from the nano-object to electrode 2 and (*2.*) an electron from electrode 1 tunnels to the nano-object. In the depicted case, the energy of the initial and the final state is the same and this process is therefore called *elastic* COT.

If the energy of the initial state is different than the energy of the final state, one speaks of *inelastic* COT. Examples of inelastic COT include transitions to excited spin states and excited vibrational states. These inelastic processes only contribute to transport when the bias voltage exceeds the energy difference between the initial and final state. Accordingly, in a transport measurement a step in the $\mathrm{d}I/\mathrm{d}V$ can be expected at the bias voltage corresponding to this excitation energy. The position at which the $\mathrm{d}I/\mathrm{d}V$ step occurs is indicated by the horizontal dashed lines in the COT region of Figure 2.1b. From the COT $\mathrm{d}I/\mathrm{d}V$ excitation steps one can extract information about the spin- and vibrational excitations in a system. In the case of spin excitations, the only allowed transitions are given by the COT spin-selection rules [1]:

$$\Delta S = 0, \pm 1 \quad \text{and} \quad \Delta m = 0, \pm 1, \tag{2.2}$$

in which ΔS and Δm are the differences in the total spin and the magnet quantum numbers, respectively, between the initial and the final state. This requirement for COT follows from the fact that only two spin-1/2 particles — the two electrons — are involved in the COT process.

2.3. THE KONDO EFFECT

COT events can either leave the state of the nano-object unchanged or can alter e.g. the vibrational- or the spin state. When the outgoing electron has spin up and the incoming electron has spin down, the nano-object's spin has effectively been flipped. Many of such spin-flip COT events can lead to a well-known phenomenon called the *Kondo effect* [2]. The Kondo effect arises when the coupling between the nano-object and the electrode

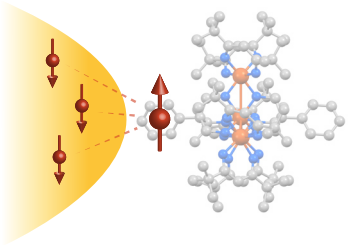

Figure 2.2: Sketch of the Kondo effect, in which a localized spin on a molecule forms a many-body singlet state with the conduction electrons in the coupled electrode.

is strong and the temperature is below a certain temperature T_K known as the *Kondo temperature*. The total energy of this system is lowered by the formation of a many-body state, in which the nano-object's spin forms a singlet state with the nearby conduction electrons in the electrode [3]. The total spin of this state is zero and the conduction electrons — the Kondo 'cloud' — are screening the nano-object's spin. This scenario is sketched in Figure 2.2. The interaction between the electrode and the nano-object through this many-body state results in a highly conductive transport channel pinned to the Fermi level of the electrode, known as a *Kondo resonance* [4].

A Kondo cloud can be distributed over the two electrodes of the junction or — in case of an asymmetric coupling — be localized in one electrode. In the latter case, the other electrode acts as a 'probe' of the Kondo resonance. In both scenarios, the signature of a Kondo resonance in charge-transport measurements is the appearance of a zero-bias peak in the COT region [5]. Typically, only the charge states with an odd number of electrons have a finite spin such that a Kondo resonance is only observed in the 'odd' charge states.

The Kondo effect is ubiquitous in charge transport through single molecules and also in this work it appears in several measurements. Besides the standard Kondo effect, exotic Kondo effects such as the singlet-triplet Kondo effect and the two-stage Kondo effect, are the main topics of discussion in Chapter 3.

2.4. THE PROXIMITY EFFECT

In the introductory chapter of this work we discussed how single-molecule junctions can be created by controlled electromigration and self-breaking. We argued that gold is an exceptionally suitable material for electromigration due to the relatively high mobility of the atoms at room temperature and the chemical inertness of the material. In addition, gold electrodes behave as model electron reservoirs with a relatively flat density of states. Unfortunately, gold does not become superconducting at low temperatures. Nevertheless, it is possible to induce superconductivity in gold electrodes by exploiting the superconducting *proximity effect*. The proximity effect is the adoption of superconducting properties by a normal metal through a nearby superconductor. In this section we will describe the theory of the proximity effect and present simulated properties of proximity-induced superconducting electrodes.

2.4.1. PAIR POTENTIAL AND PAIR AMPLITUDE

A superconductor can be characterized by a complex order parameter $\Delta = |\Delta| e^{i\varphi}$. The magnitude of the order parameter is equal to the superconducting energy gap which can be directly measured in transport measurements. The phase φ is by itself not an observable quantity — only the phase *difference* between two superconductors is. For example, the Josephson effect is driven by the phase difference between weakly-coupled superconductors. In most conventional superconductors the order parameter is homogeneous throughout the material. When a normal metal is brought in contact with the superconductor the order parameter changes across the interface from $\Delta = 0$ deep within the normal metal to $\Delta = \Delta_{SC}$ inside the superconductor. Close to the interface, Δ evolves as a function of the position coordinate $\mathbf{r}$ and the term *pair potential* is typically used in this context [6]. The pair potential is given by:

$$\Delta(\mathbf{r}) = V F(\mathbf{r}) = V \langle \psi_\uparrow(\mathbf{r}) \psi_\downarrow(\mathbf{r}) \rangle , \tag{2.3}$$

where V is the electron-electron interaction potential and $F(\mathbf{r})$ is the *pair amplitude*. The driving force behind the formation of a superconducting condensate is the attractive electron-electron interaction ($V < 0$) which results from electron-phonon interactions. In normal metals the electron-phonon coupling is not strong enough to overcome the repulsive Coulomb forces and $V \geq 0$. The pair amplitude $F(\mathbf{r}) = \langle \psi_\uparrow(\mathbf{r}) \psi_\downarrow(\mathbf{r}) \rangle$ is the probability amplitude of finding electrons with opposite spin — Cooper pairs — at position $\mathbf{r}$. Even in the absence of an attractive electron-phonon coupling, pairing correlations ($F > 0$) can be induced in the normal metal when it is in contact with a superconductor. The Cooper pairs formed in the superconductor can preserve their coherence across the interface over a finite distance. The normal metal thereby locally adopts certain properties of the superconductor, such as an energy gap in its local density of states.

2.4.2. PROXIMITY EFFECT BY ANDREEV REFLECTIONS

At the interface between a normal metal and a superconductor electron transport does not occur in the same way as between two normal metals. While electrons with an energy $\varepsilon > \Delta$ could enter the superconductor through the quasiparticle continuum, electrons with $\varepsilon < \Delta$ cannot access single-particle states. They can only cross the interface by a process known as *Andreev reflection* [7]. Andreev reflection is commonly described as the reflection of an incoming electron as a hole, whereby a charge of $2e$ is transferred from the normal metal to the superconductor [8]. Effectively, a Cooper pair is added to the superconductor in this process. If the energy of the incoming electron was equal to ε, the energy of the reflected hole will be $-\varepsilon$ to ensure energy conservation. Since a hole is defined as the absence of an electron, Andreev reflection can also be described as the transfer of two electrons from the normal metal into the superconductor, where they continue as part of the Cooper-pair condensate.

Charge transfer by Andreev reflection also works in the opposite way: Cooper pairs from the superconductor may continue as two electrons in the normal metal with an energy difference 2ε. This energy mismatch will result in the dephasing of the electrons over a characteristic time $\tau_{dep} \sim \hbar/\varepsilon$ after which they lose coherence. The electrons that return to the superconductor before this time will carry the superconducting correlations throughout the normal metal, thereby establishing the proximity effect.

Electrons in a disordered conductor of size L spend a characteristic time $\tau_{esc} = L^2/D$ in the system before returning — in this case — to the superconductor [9]. Using this expression for the escape time, τ_{esc}, and the dephasing time, $\tau_{dep} = \hbar/\varepsilon$, an energy cutoff can be found above which superconducting correlations are lost in the normal metal: $\varepsilon_{Th} = \hbar D/L^2$, where D is the diffusion constant. This energy is known as the Thouless energy. Electrons with an energy above the Thouless energy will dephase in the normal metal to the extent that they lose coherence with the superconductor and start to contribute to the single-particle density of states. Electrons below the Thouless energy remain part of the superconducting condensate, whereby an induced energy gap, $\Delta_{prox} < \Delta$, is realized in the normal metal — approximately equal to the Thouless energy.

2.4.3. MODIFIED LOCAL DENSITY OF STATES

The opening of an energy gap by the proximity effect is not the only change in the density of states of the normal metal. Here we calculate the modified density of states of a normal wire connected to a superconductor. We perform simulations using the Usadel formalism, which works in the quasiclassical diffusive regime, i.e., where the Fermi wavelength, λ_F, and the mean free path, ℓ, are much smaller than the superconducting coherence length. The simulations discussed in this section are made using the code of P. Virtanen (2007) [10]. The system we simulate is sketched in Figure 2.3a and contains a one-dimensional normal metal wire of length L connected on one side to a superconducting reservoir. We consider this system as a minimal model for a proximity-induced superconducting electrode.

First, we treat the ideal case and neglect pair-breaking effects. The results of the simulations are shown in Figure 2.3b where the local density of states (LDOS) is plotted as a function of energy at the end of the wire (at $x = L$) for various L. For a length of 1 nm the LDOS strongly resembles that of the BCS density of states with a gap size of about Δ_S and a sharp peak at the edge of the gap. As the length is increased the gap shrinks and the peak at the edge of the gap becomes more rounded. Since the Thouless energy scales as $\sim 1/L^2$, the size of the induced gap for longer wires scales in a similar way. For small L the size of the proximity gap, Δ_{prox}, is better approximated by the relation $\Delta_{prox} = 1/(c\xi_S + L)^2$, where c is a constant [11]. The added length scale reflects the inverse proximity effect, i.e., the induced normal-metal behavior in the superconductor close to the interface. In the simulations this effect is taken into account by calculating the pair potential across the interface self-consistently [11].

Next, we focus on the inclusion of pair-breaking effects. We consider an inelastic scattering rate, Γ_{in}, as well as a spin-flip scattering rate, Γ_{sf}, which can be readily included in the Usadel formalism [13]. Scattering processes involving paramagnetic impurities can be described by Γ_{sf}. The term Γ_{in} accounts for inelastic processes, such as electron-phonon scattering. Figure 2.3c and d show the effects of Γ_{in} and Γ_{sf}, respectively. Both effects cause further rounding of the peaks at the gap edge. Additionally, Γ_{sf} reduces the size of the proximity gap. Another difference between Γ_{in} and Γ_{sf} is that spin-flip scattering preserves the complete suppression of the LDOS within the gap — as long as the gap is not closed — whereas for any finite Γ_{in} the subgap LDOS is lifted at all energies (in Figure 2.3d most clearly seen for large L).

The spin-flip scattering rate is not only relevant in the case of paramagnetic impurities,

2

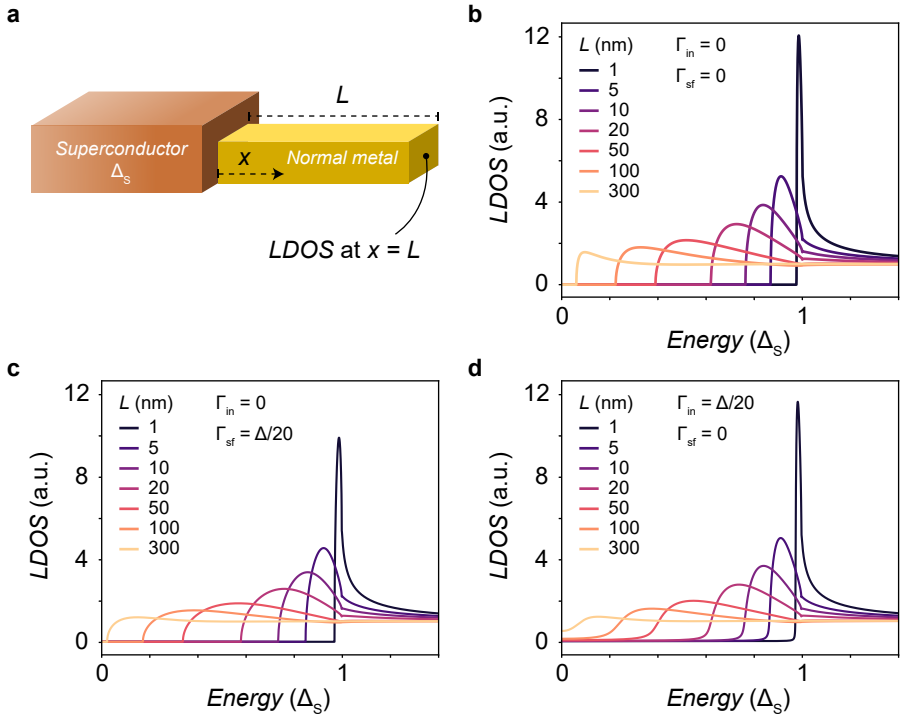

Figure 2.3: a. Sketch of the simulated normal metal-superconductor system for which the local density of states is calculated at the free end of the normal metal. **b.,c.,d.** Simulated local density of states in the normal metal at $x = L$ for different lengths and various values for the inelastic scattering rate Γ_{in} and the spin-flip scattering rate Γ_{sf}. A fully transparent interface between the normal metal and the superconductor is assumed. Other simulation parameters include the diffusion constant of the normal metal, $D_N = 0.026\,m^2/s$, the Debye energy $\Theta_D = 165\,K$, of which the values are based on other reports in which gold was used [12].

but can also be used as an effective parameter to account for transverse magnetic fields [13]. The simulation in Figure 2.3c shows that such a magnetic field will broaden the gap edge and will cause an additional decrease of Δ_{prox} in addition to the magnetic-field suppression of Δ_{S}.

2.4.4. PROXIMITIZED TUNNEL JUNCTIONS

In Chapter 6 we present transport measurements of tunnel junctions with proximity-induced superconducting, or *proximitized* electrodes on both sides. When transport through the junction occurs deep inside the tunneling regime, i.e., the normal-state resistance of the junction, $R \gg R_{\text{Q}} \approx 13\,\text{k}\Omega$, we can calculate the IV-characteristics of the proximitized junction from the LDOS of the electrodes (see Section 2.4.3) by employing the *semiconductor model* [14]. With this model, the tunneling current can be directly calculated by a convolution of the LDOS of both electrodes within a thermally broadened bias-voltage window:

$$I(V) = \frac{G_{\text{N}}}{e} \int_{-\infty}^{\infty} \frac{N_{1\text{S}}(E)}{N_{1\text{N}}} \frac{N_{2\text{S}}(E+eV)}{N_{2\text{N}}} [f(E,T) - f(E+eV,T)]\,dE. \tag{2.4}$$

where $N_{1\text{S,2S}}$ ($N_{1\text{N,2N}}$) is the LDOS of the two proximitized electrodes in the superconducting (normal) state and $G_{\text{N}} = 1/R$ is the normal-state conductance of the proximitized junction. Figure 2.4a shows a schematic representation of the semiconductor model, in which the LDOS of the two electrodes is drawn. The orange fill color represents the occupation of quasiparticles up to the Fermi levels E_{F1} and E_{F2}, according to the Fermi-Dirac distribution. The Fermi levels of the two electrodes are offset by the bias voltage $eV = E_{\text{F1}} - E_{\text{F2}}$. This scheme shows that quasiparticles can tunnel from one electrode to the other (as indicated by the horizontal arrow) when the bias voltage exceeds two times the proximity gap, i.e., $|eV| > 2\Delta_{\text{prox}}$.

Using the LDOS calculated within the Usadel formalism we simulate the $\text{d}I/\text{d}V$ spectra of the proximitized tunnel junction using Equation (2.4) for different lengths of the normal-metal part of the electrodes (a single electrode is schematically depicted in Figure 2.3a). The results are shown in Figure 2.4b, where we plot the simulated $\text{d}I/\text{d}V$ (normalized to G_{N}) as a function of V in units of the bulk superconducting gap, Δ_{S}. For all simulated spectra the lengths of the normal metal parts of the two electrodes are equal and we neglect any pair-breaking effects. All spectra show a hard gap which decreases in size as the length is increased. Quasiparticle currents are only allowed when $|eV| > 2\Delta_{\text{prox}}$ which implies that the distance between the $\text{d}I/\text{d}V$ peaks equals $4\Delta_{\text{prox}}$.

The $\text{d}I/\text{d}V$ spectrum corresponding to the shortest length of 25 nm shows negative $\text{d}I/\text{d}V$ dips at the outer edges, which correspond to a decrease in the current. The negative $\text{d}I/\text{d}V$ can be understood as follows: Around $|eV| = 2\Delta_{\text{prox}}$ the LDOS peak of the occupied states in one electrode is at the same energy as the LDOS peak of the unoccupied states in the other electrodes (as in Figure 2.4a), which results in a large quasiparticle current. As V is increased, the LDOS peaks are no longer at the same energy and the contribution from these peaks to the quasiparticle current goes down. Depending on the exact shape of the LDOS peaks the suppression in the $\text{d}I/\text{d}V$ can become negative, as e.g. in the 25 nm-spectrum. These negative $\text{d}I/\text{d}V$ dips have been reported e.g. in proximitized gold tunnel junctions [15].

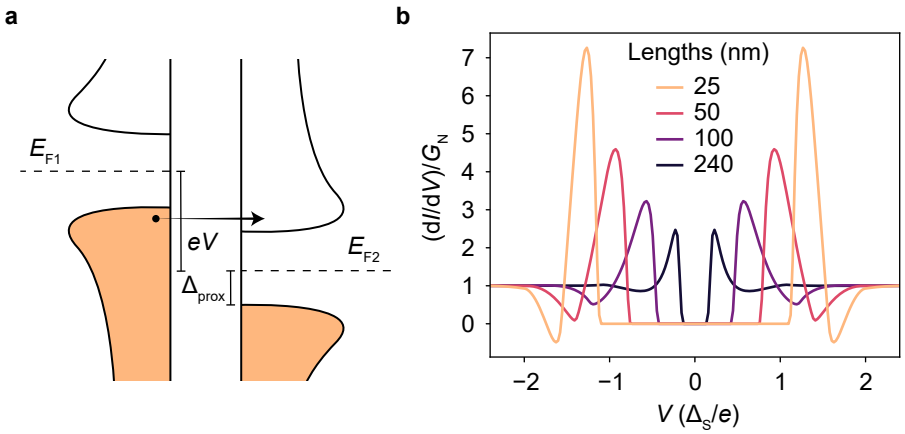

Figure 2.4: a. Schematic representation of the semiconductor model showing the LDOS of both electrodes, filled with quasiparticles (orange) according to the Fermi-Dirac distribution. As $|eV| > 2\Delta_{prox}$ quasiparticles from one electrode can flow to the other as indicated by the arrow. **b.** Simulated dI/dV spectra, using the semiconductor model, for a tunnel junction consisting of two proximitized electrodes with normal-metal parts of different lengths. The LDOS of the proximitized electrodes has been taken from similar Usadel calculations as presented in Figure 2.3b, using the same simulation parameters.

When the transparency of the junction is increased and we shift from deep in the tunneling regime towards a metallic constriction, the semiconductor model is no longer valid [8]. The IV-characteristics of the proximitized junction start to show additional features related to quantum-transport phenomena such as multiple Andreev reflections [16, 17], as discussed in the next section.

2.5. MULTIPLE ANDREEV REFLECTIONS

In Section 2.4.2 we discussed the Andreev reflection — the process by which a charge of $2e$ is transferred across a normal metal-superconductor interface. The same process can occur between two superconductors connected by a constriction. Quasiparticles from one superconductor can undergo an Andreev reflection at the other superconductor, thereby transferring a charge of $2e$. The reflected quasiparticle can in turn undergo another Andreev reflection at the first superconductor without losing coherence [18]. Coherent processes containing several individual Andreev reflections are known as *multiple Andreev reflections* (MAR). It can be shown that MAR processes of order n open up transport channels at $V = 2\Delta/ne$ [16]. As a result, the IV-characteristics of the superconducting junction show sharp increases in the current at those bias voltages.

In this thesis we study proximity-induced superconducting junctions in which the gaps of the two (proximitized) superconductors can be different ($\Delta_1 \neq \Delta_2$). In this case the requirement for MAR is more complicated [19]. MAR processes open up when the bias voltage reaches $eV > \Delta_1/n$, $eV > \Delta_2/m$ and $eV > (\Delta_1 + \Delta_2)/(2l+1)$ for certain integer values of n, m and l. The relative size of Δ_1 and Δ_2 determines which integers are

allowed and which are forbidden [19].

The transparency of the constriction between the superconductors plays an important role in the visibility of MAR in a transport experiment. As the transparency goes to zero MAR of all orders is suppressed [16, 20]. At slightly higher transparency only MAR processes of low order are visible whereas at high transparency high-order MAR processes dominate the low-bias spectrum.

2.6. SUBGAP BOUND STATES

In superconducting transport through confined nanostructures, such as semiconductor quantum dots and single molecules, Andreev reflections play an important role. In these nano-objects, the combination of Andreev reflection and strong scattering may lead to the formation of *Andreev bound states* (ABS) [21]. These ABS result from multiple Andreev reflections becoming resonant — constructively interfering — and are localized in the region where the pair potential $\Delta(\mathbf{r})$ strongly varies. ABS typically result in sharp peaks in the density of states of the junction and can therefore be probed in transport experiments [22]. Depending on the relative size of the charging energy U of the nano-object and the Δ of the superconductor two distinct types of ABS can be considered [23]. In the following we discuss the two types of ABS that form as a result of Andreev reflections in the regimes $\Delta \gg U$ and $U \gg \Delta$.

2.6.1. PROXIMITY-INDUCED BOUND STATES

When the charging energy of the nano-object is much smaller than the superconducting gap of the coupled superconducting electrode, i.e., $U \ll \Delta$, a BCS-like superconducting state can form in the nanostructure when the tunnel coupling is sufficiently strong [24]. As an example we consider a single-level system and suppose that for $\Delta = 0$ the ground state is $|\uparrow\rangle$, i.e., the single level only contains one spin-up electron. When Δ is increased the BCS-like state $\sim (|0\rangle + |\uparrow\downarrow\rangle)$ starts to compete with the ground state as the states with even occupancy are favored by the finite Δ. We refer to this state as the *proximity-induced bound state*. The energy of this state can drop below Δ and could potentially be probed as a subgap excitation in a transport experiment. In single molecules and nanoscale semiconductor quantum dots however, the charging energy is typically much larger than the superconducting gap and the formation of proximity-induced ABS is suppressed. In other confined nanostructures, such as carbon nanotube quantum dots [22], the limit $U \ll \Delta$ does never fully apply as the experiments occur in the intermediate regime, where $U \sim \Delta$. Whereas the two limits $U \ll \Delta$ and $U \gg \Delta$ are well understood, the intermediate regime is difficult to treat from a theoretical point of view. The involved states in the intermediate regime are expected to be a combination of proximity-induced bound states and the Yu-Shiba-Rusinov states described in the next section.

2.6.2. YU-SHIBA-RUSINOV STATES

In the regime $U \gg \Delta$ charge fluctuations are suppressed by the large charging energy and the proximity-induced ABS described above is energetically unfavorable. Still, a different

kind of ABS known as the *Yu-Shiba-Rusinov* (YSR) state [25–27] can form when the tunnel coupling between the nano-object and the superconductor is sufficiently strong. To explain the emergence of YSR states we consider a decoupled system of a nano-object in the ground state $|\uparrow\rangle$ and a superconductor in the BCS ground state. As the tunnel coupling between the nano-object and the superconductor is increased, a quasiparticle state in the superconductor is lowered in energy by the magnetic exchange interaction with the nano-object's spin. This state corresponds to a singlet state of the nano-object's spin and the quasiparticle spin. In the limit of a classical spin, i.e., the spin S on the nano-object is static, the excitation energy of the YSR state is given by [26, 28]:

$$E_{\mathrm{YSR}} = \Delta \frac{1-(\pi J S \rho)^2}{1+(\pi J S \rho)^2}, \tag{2.5}$$

where J is the exchange coupling and ρ is the density of states at the Fermi level. From this expression it follows that the YSR-singlet crosses zero energy at $J = 1/\pi S\rho$ and becomes the ground state at higher J. In a transport experiment the exchange coupling can be manipulated by applying a voltage to a capacitively-coupled gate electrode, whereby the energy of the YSR state can be tuned and the system can be driven through a quantum phase transition [29].

Treating the spin of the nano-object as a classical spin is a crude approximation, but is often used to make calculations tractable and to give qualitatively valid results in certain regimes [30, 31]. Without the classical-spin approximation no closed expression such as Equation (2.5) can be found for the bound-state energy and the simple picture of a *single* exchange-coupled quasiparticle is no longer valid. The problem of a quantum spin coupled to a superconductor can be addressed by numerical renormalization group (NRG) [32] calculations, which show that the nano-object's spin may form a many-body singlet state with a quasiparticle 'cloud' in the superconductor [33]. In a transport experiment, this singlet state appears as a subgap ($E_{\mathrm{YSR}} < \Delta$) excitation which can be probed e.g. in a normal metal-superconductor tunnel junction [29]. The emergence of the many-body YSR singlet in superconducting devices is similar to the Kondo effect in the case of normal-metal electrodes [2]. Indeed, the exchange coupling J in Equation (2.5) is also the driving force behind the formation of a Kondo singlet.

REFERENCES

[1] R. Gaudenzi, M. Misiorny, E. Burzurí, M. R. Wegewijs, and H. S. J. van der Zant. "Transport mirages in single-molecule devices". *The Journal of Chemical Physics* 146.9 (Mar. 2017), p. 092330. DOI: 10.1063/1.4975767.

[2] J. Kondo. "Resistance Minimum in Dilute Magnetic Alloys". *Progress of Theoretical Physics* 32.1 (July 1964), pp. 37–49. DOI: 10.1143/ptp.32.37.

[3] K. G. Wilson. "The renormalization group: Critical phenomena and the Kondo problem". *Reviews of Modern Physics* 47.4 (Oct. 1975), pp. 773–840. DOI: 10.1103/revmodphys.47.773.

[4] S. Hershfield, J. H. Davies, and J. W. Wilkins. "Probing the Kondo resonance by resonant tunneling through an Anderson impurity". *Physical Review Letters* 67.26 (Dec. 1991), pp. 3720–3723. DOI: 10.1103/physrevlett.67.3720.

[5] J. Nygård, D. H. Cobden, and P. E. Lindelof. "Kondo physics in carbon nanotubes". *Nature* 408.6810 (Nov. 2000), pp. 342–346. DOI: 10.1038/35042545.

[6] T. M. Klapwijk. "Proximity Effect From an Andreev Perspective". *Journal of Superconductivity* 17.5 (Oct. 2004), pp. 593–611. DOI: 10.1007/s10948-004-0773-0.

[7] A. F. Andreev. "The thermal conductivity of the intermediate state in superconductors". *JETP* 19.5 (1964), pp. 1228–1231.

[8] G. E. Blonder, M. Tinkham, and T. M. Klapwijk. "Transition from metallic to tunneling regimes in superconducting microconstrictions: Excess current, charge imbalance, and supercurrent conversion". *Physical Review B* 25.7 (Apr. 1982), pp. 4515–4532. DOI: 10.1103/physrevb.25.4515.

[9] B. Pannetier and H. Courtois. "Andreev Reflection and Proximity effect". *Journal of Low Temperature Physics* 118.5/6 (2000), pp. 599–615. DOI: 10.1023/a:1004635226825.

[10] P. Virtanen and T. T. Heikkilä. "Thermoelectric effects in superconducting proximity structures". *Applied Physics A* 89.3 (July 2007), pp. 625–637. DOI: 10.1007/s00339-007-4189-0.

[11] W. Belzig, F. K. Wilhelm, C. Bruder, G. Schön, and A. D. Zaikin. "Quasiclassical Green's function approach to mesoscopic superconductivity". *Superlattices and Microstructures* 25.5-6 (May 1999), pp. 1251–1288. DOI: 10.1006/spmi.1999.0710.

[12] M. Wolz, C. Debuschewitz, W. Belzig, and E. Scheer. "Evidence for attractive pair interaction in diffusive gold films deduced from studies of the superconducting proximity effect with aluminum". *Physical Review B* 84.10 (Sept. 2011). DOI: 10.1103/physrevb.84.104516.

[13] W. Belzig, C. Bruder, and G. Schön. "Local density of states in a dirty normal metal connected to a superconductor". *Physical Review B* 54.13 (Oct. 1996), pp. 9443–9448. DOI: 10.1103/physrevb.54.9443.

[14] J. Bardeen. "Tunneling Into Superconductors". *Physical Review Letters* 9.4 (Aug. 1962), pp. 147–149. DOI: 10.1103/physrevlett.9.147.

[15] E. Scheer, W. Belzig, Y. Naveh, M. H. Devoret, D. Esteve, and C. Urbina. "Proximity Effect and Multiple Andreev Reflections in Gold Atomic Contacts". *Physical Review Letters* 86.2 (Jan. 2001), pp. 284–287. DOI: 10.1103/physrevlett.86.284.

[16] D. Averin and A. Bardas. "ac Josephson Effect in a Single Quantum Channel". *Physical Review Letters* 75.9 (Aug. 1995), pp. 1831–1834. DOI: 10.1103/physrevlett.75.1831.

[17] J. C. Cuevas, A. Martín-Rodero, and A. L. Yeyati. "Hamiltonian approach to the transport properties of superconducting quantum point contacts". *Physical Review B* 54.10 (Sept. 1996), pp. 7366–7379. DOI: 10.1103/physrevb.54.7366.

[18] T. M. Klapwijk, G. E. Blonder, and M. Tinkham. "Explanation of subharmonic energy gap structure in superconducting contacts". *Physica B+C* 109-110 (July 1982), pp. 1657–1664. DOI: 10.1016/0378-4363(82)90189-9.

[19] M. Hurd, S. Datta, and P. F. Bagwell. "Current-voltage relation for asymmetric ballistic superconducting junctions". *Physical Review B* 54.9 (Sept. 1996), pp. 6557–6567. DOI: 10.1103/physrevb.54.6557.

[20] M. Ternes, W.-D. Schneider, J.-C. Cuevas, C. P. Lutz, C. F. Hirjibehedin, and A. J. Heinrich. "Subgap structure in asymmetric superconducting tunnel junctions". *Physical Review B* 74.13 (Oct. 2006). DOI: 10.1103/physrevb.74.132501.

[21] J. A. Sauls. "Andreev bound states and their signatures". *Philosophical Transactions of the Royal Society A: Mathematical, Physical and Engineering Sciences* 376.2125 (June 2018), p. 20180140. DOI: 10.1098/rsta.2018.0140.

[22] J.-D. Pillet, C. H. L. Quay, P. Morfin, C. Bena, A. L. Yeyati, and P. Joyez. "Andreev bound states in supercurrent-carrying carbon nanotubes revealed". *Nature Physics* 6.12 (Nov. 2010), pp. 965–969. DOI: 10.1038/nphys1811.

[23] G. O. Steffensen. *Yu-Shiba-Rusinov Bound States in Quantum Dots*. Niels Bohr Institute, University of Copenhagen, 2017.

[24] T. Meng, S. Florens, and P. Simon. "Self-consistent description of Andreev bound states in Josephson quantum dot devices". *Physical Review B* 79.22 (June 2009). DOI: 10.1103/physrevb.79.224521.

[25] L. Yu. "Bound state in superconductors with paramagnetic impurities". *Acta Phys. Sin* 21.1 (1965), pp. 75–91.

[26] H. Shiba. "Classical Spins in Superconductors". *Progress of Theoretical Physics* 40.3 (Sept. 1968), pp. 435–451. DOI: 10.1143/ptp.40.435.

[27] A. I. Rusinov. "Superconductivity near a paramagnetic impurity". *Soviet Journal of Experimental and Theoretical Physics Letters* 9 (1969), p. 85.

[28] R. Žitko, J. S. Lim, R. López, and R. Aguado. “Shiba states and zero-bias anomalies in the hybrid normal-superconductor Anderson model”. *Physical Review B* 91.4 (Jan. 2015). DOI: 10.1103/physrevb.91.045441.

[29] A. Jellinggaard, K. Grove-Rasmussen, M. H. Madsen, and J. Nygård. “Tuning Yu-Shiba-Rusinov states in a quantum dot”. *Physical Review B* 94.6 (Aug. 2016). DOI: 10.1103/physrevb.94.064520.

[30] A. V. Balatsky, I. Vekhter, and J.-X. Zhu. “Impurity-induced states in conventional and unconventional superconductors”. *Reviews of Modern Physics* 78.2 (May 2006), pp. 373–433. DOI: 10.1103/revmodphys.78.373.

[31] V. Koerting, B. M. Andersen, K. Flensberg, and J. Paaske. “Nonequilibrium transport via spin-induced subgap states in superconductor/quantum dot/normal metal cotunnel junctions”. *Physical Review B* 82.24 (Dec. 2010). DOI: 10.1103/physrevb.82.245108.

[32] R. Bulla, T. A. Costi, and T. Pruschke. “Numerical renormalization group method for quantum impurity systems”. *Reviews of Modern Physics* 80.2 (Apr. 2008), pp. 395–450. DOI: 10.1103/revmodphys.80.395.

[33] K. Satori, H. Shiba, O. Sakai, and Y. Shimizu. “Numerical Renormalization Group Study of Magnetic Impurities in Superconductors”. *Journal of the Physical Society of Japan* 61.9 (Sept. 1992), pp. 3239–3254. DOI: 10.1143/jpsj.61.3239.

3

MOLECULAR DOUBLE-SPIN SYSTEMS

Single pairs of exchange-coupled spins are among the most basic spin systems. Despite their simplicity, when embedded in an electrical circuit they can host many interesting spin-related phenomena which can be probed in charge-transport experiments. In this chapter, we study some of these phenomena in chemically-synthesized organic diradical molecules. We show that the molecule's complex structure can be well approximated by only considering two exchange-coupled spins, each with a spin of $S = 1/2$. Given this simplification, the diradical molecule behaves as a model system and provides a platform for studying exchange-coupled spin pairs or — more generally — double quantum dot systems. We present transport measurements of diradical single-molecule devices with increasing levels of complexity. From model two-spin behavior and the appearance of the singlet-triplet Kondo effect, to observations of an anisotropic exchange coupling and an exotic two-stage Kondo effect.

Parts of this chapter have been published in [1] and [2].

Double quantum dots are ubiquitous in the field of quantum transport as they exhibit many interesting spin-related phenomena, such as the Pauli spin blockade [3] and exotic Kondo effects [4], and provide proof-of-concept demonstrations for applications in spintronics and quantum computation [5–7]. Experimental realizations of double quantum dots include nanoscale devices based on carbon nanotubes [8], silicon [9], two-dimensional electron gases [10], graphene [11] and semiconductor nanowires [12]. Far less abundant are molecular double quantum dots [13]. Nevertheless, individual molecules that behave as double quantum dots are attractive platforms because of their well-separated energy scales. For example, the addition energy of a single-molecule system typically exceeds all the other energy scales. This enables measuring all the spin- and vibrational excitations in a large energy range, within a single charge state. Also, the exchange coupling between the dots can be of the order of 10 meV — significantly larger than in other systems — such that the spin structure of the molecular double quantum dot can be resolved in great detail, as will be shown in this chapter.

The double quantum dot system of interest in this chapter is an all-organic diradical molecule [14]. This molecule proved to be exceptionally well-suited for transport studies on electromigrated junctions, exhibiting a vast range of spin-related phenomena. We first focus on measurements which display exceptionally clean spin-excitation spectra which can be understood in terms of elementary quantum-dot models. Later in this chapter, we turn to more exotic behavior observed in the same type of devices. We focus on the singlet-triplet Kondo effect, the anisotropic exchange coupling and the rarely observed two-stage Kondo effect.

3.1. RADICAL MOLECULES AS MODEL SPIN SYSTEMS

Organic radical molecules have one or more unpaired spins in their ground state. In contrast to non-radical molecules, only one electron resides in the highest occupied molecular orbital (HOMO), which is why this orbital is commonly referred to as the singly-occupied molecular orbital (SOMO). For certain radical molecules, this orbital remains singly-occupied even at room temperature such that the radical character of the molecule is preserved. In this chapter we focus on one chemically-synthesized organic radical in particular, namely the 2,4,6-hexakis-(pentachlorophenyl)mesitylene diradical molecule [14]. It belongs to a family of organic poly-radicals of which two members have already been previously studied by charge transport experiments: a monoradical molecule [15] and a triradical molecule [16].

As the name suggests, the diradical molecule has two unpaired electrons and thus two unpaired spins in its ground state. The spins are coupled by exchange interactions and can form a spin singlet or a spin triplet ground state, depending on the sign of the exchange coupling J. In frozen solutions, the diradical molecule is known to have a ferromagnetic exchange coupling $J < 0$, such that its ground state is a spin triplet and the total spin $S = 1$ [2, 14]. In the absence of other interactions the energy difference between the singlet state and the triplet states is equal to $|J|$. The molecular structure of the diradical molecule is shown in Figure 3.1b. The two black dots above the carbon (C) atoms indicate the unpaired electrons and the red arrows are drawn to emphasize the presence of

the unpaired spins in these radical centers. The exchange coupling between the radical spins is represented by the dashed line.

The expected spin-excitation spectra and magnetic-field dependence of an exchange-coupled spin pair is shown in Figure 3.1c and d, for $J > 0$ and $J < 0$, respectively. The singlet and triplet state are separated by J at $B = 0$, and the triplet excitations split in three for $B > 0$. In the singlet ground state, all three spin excitations are accessible through cotunneling (COT) processes (see Section 2.2), as indicated by the dashed arrows. For the triplet ground state, the COT spin-selection rules $\Delta m = 0, \pm 1$ (see Section 2.2) prevent transitions between the spin states $|S = 0, m = -1\rangle$ and $|S = 0, m = 1\rangle$, so only two excitations from the ground state are expected in this case.

We study charge transport through the diradical molecule by embedding it in an electric circuit, as sketched in Figure 3.1a, and measuring transport through the resulting single-molecule device. The molecule is embedded in the circuit as follows: By electromigration [17] and self-breaking [18] of a gold nanowire (shown in the middle of Figure 3.1a), a nanometer-sized gap is formed in which molecules can be trapped. The size of the diradical molecule is of the order of a nanometer, which enables single molecules to enter the electromigrated gap and contact the two gold electrodes (see sketch on the right in Figure 3.1a).

The diradical molecules are introduced by dropcasting a dilute solution on a chip with 24 electromigrated gold nanowires. After pumping away the solution and cooling down the system in a dilution refrigerator ($T \approx 40\,\mathrm{mK}$), we find transport signatures of trapped single molecules in 2 to 5 junctions per chip. The concentration of diradical molecules in the solution is adjusted to obtain a yield of this order. A higher yield would likely result in trapping multiple molecules in the electromigrated gap, which is undesired for these experiments.

We measure the DC current, I, through the single-molecule devices as a function of the applied bias voltage, V, over the junction, the voltage applied to a capacitively coupled gate electrode, V_g, the temperature T and the magnetic field B. By measuring the $\mathrm{d}I/\mathrm{d}V$ as a function of V and B we can probe the spin excitations of this system and identify the spin structure of the molecule. This technique is known as spin-flip inelastic electron tunneling spectroscopy (IETS). In the measurements presented in this section, the gate voltage is set to a fixed value deep within the cotunneling regime (see Sections 2.1 and 2.2 for a discussion about the different transport regimes) such that charge fluctuations are suppressed and the spin excitations can be resolved in great detail.

Two spin-flip IETS measurements of different diradical single-molecule devices are shown in Figure 3.2a and b. The measurements are performed at fixed $V_\mathrm{g} = -2.3\,\mathrm{V}$ and $V_\mathrm{g} = 0\,\mathrm{V}$, respectively. In Figure 3.2a the $\mathrm{d}I/\mathrm{d}V$ increases abruptly around $V = \pm 5\,\mathrm{mV}$ as a result of COT excitations to the triplet state: When the excess energy of the conduction electrons ($e|V|$) equals the singlet-triplet excitation energy (J) an additional transport channel involving the triplet state opens up, which causes the increase in the $\mathrm{d}I/\mathrm{d}V$ at the corresponding energy. As the magnetic field increases, the triplet excitation splits in three, as indicated by the white dashed lines in Figure 3.1c. These excitations correspond to transitions from the singlet state to the three triplet states with the magnetic quantum numbers $m = -1, 0, 1$, whose energies change in magnetic field by $g\mu_\mathrm{B} mB$ due to the Zeeman effect. In this term, g is the g-factor of the system and μ_B is the Bohr magneton.

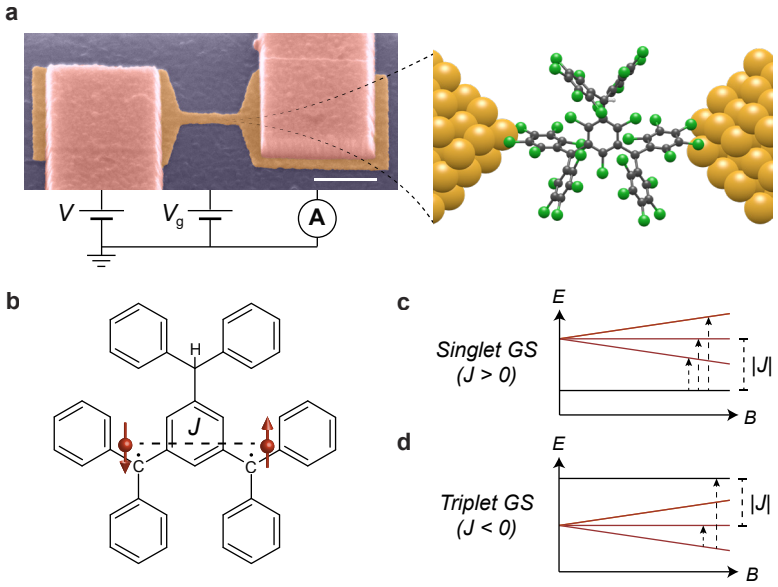

Figure 3.1: a. False-colored scanning electron microscope (SEM) image of a single-molecule transistor, along with a simplified sketch of the electronic circuit. The DC current, I, can be measured as a functions of the bias voltage, V, over the junction (brown, gold) and the gate voltage, V_g, applied to a capacitively coupled bottom gate electrode (dark gray). In the middle of the gold junction a nanometer-sized gap is formed by electromigration (not visible on this scale) wherein a molecule is embedded, as sketched on the right. The white scale bar in the SEM image represents 500 nm. **b.** The molecular structure of the diradical molecule. Unpaired electrons are indicated by the black dots above two C atoms. The red spins represent the radical spins, coupled by an exchange coupling J (dashed line). **c.** and **d.** Magnetic-field dependence of the energy levels of a two-spin system with an antiferromagnetic ($J > 0$) and a ferromagnetic exchange coupling ($J < 0$), respectively. The allowed cotunneling transitions are represented by dashed arrows. The slopes of the excitation lines result from the Zeeman effect and are equal to $gm\mu_B$.

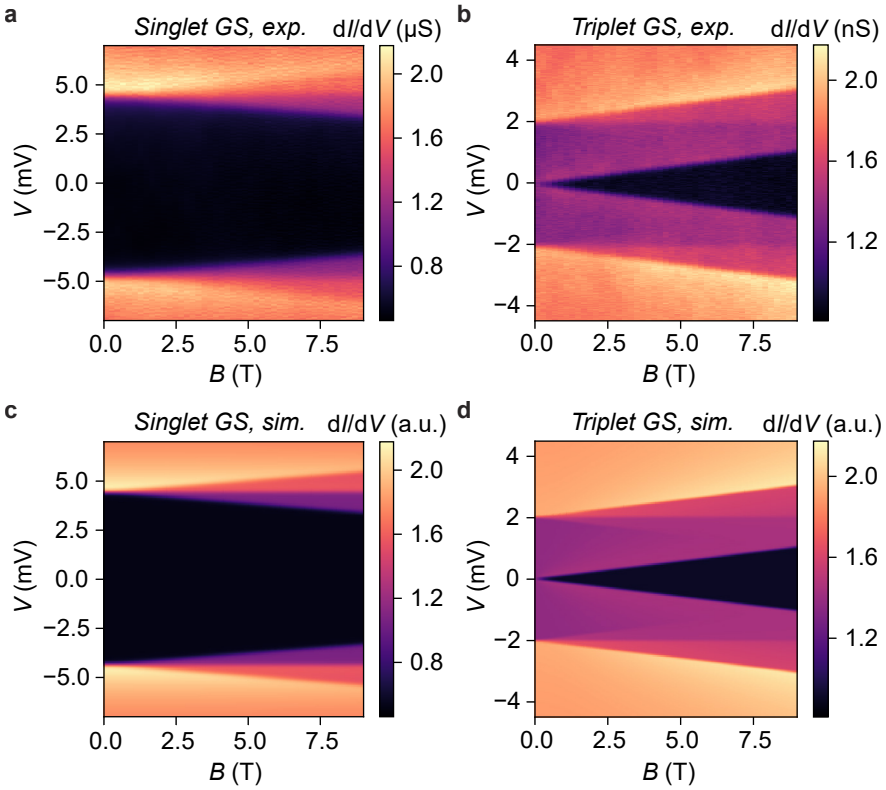

Figure 3.2: a. Experimental magnetic-field dependence of the $\mathrm{d}I/\mathrm{d}V$ spectrum of a diradical molecule device, recorded at $V_g = -2.3\,\mathrm{V}$. The triplet COT excitation around $V = \pm 5\,\mathrm{mV}$ splits in three with magnetic field in a linear way, in accordance with the Zeeman effect. **b.** Same type of measurement as in **a.** measured in a different device, recorded at $V_g = 0\,\mathrm{V}$, where we observe a spectrum which corresponds to a triplet ground state. The same excitations as in Figure 3.1d can be identified, along with a non-equilibrium excitation (see main text) at $V = \pm 2\,\mathrm{mV}$, which does not move in magnetic field. **c.** and **d.** Simulated cotunneling spectra of a two-spin system with an exchange coupling of $J = 4.5\,\mathrm{meV}$ and $J = -2\,\mathrm{meV}$, respectively.

In Figure 3.2b the excitation spectrum looks qualitatively different. At $B = 0\,\mathrm{T}$ a COT excitation is observed at $V = \pm 2\,\mathrm{mV}$. This excitation linearly moves to higher bias with increasing magnetic field. In addition, a linearly growing region of low $\mathrm{d}I/\mathrm{d}V$ (black region) develops from zero bias. This excitation spectrum is consistent with a triplet ground state (see Figure 3.1d). The $\mathrm{d}I/\mathrm{d}V$ step at $V = \pm 2\,\mathrm{mV}$ corresponds to the transition from $|S = 1, m = -1\rangle$ to $|S = 0, m = 0\rangle$, while the step developing from zero bias corresponds to the transition $|S = 1, m = -1\rangle$ to $|S = 1, m = 0\rangle$.

An additional *magnetic-field independent* COT excitation is present at $V = \pm 2\,\mathrm{mV}$, which cannot be explained by the sketch of Figure 3.1d. This excitation results from a *non-equilibrium* COT process [19]: When the relaxation rate from an excited spin state to the ground state is slow compared to the tunneling rate, the average occupation of the excited state can become comparable to the ground state. Transitions between different excited states start to play an important role in this case. In Figure 3.2b, the step at $V = \pm 2\,\mathrm{mV}$ corresponds to the transition from the excited state $|S = 1, m = 0\rangle$ to the excited state $|S = 0, m = 0\rangle$. Since $m = 0$ for both states their energies are independent of magnetic field, which is why the corresponding excitation line is horizontal.

The transport data in Figure 3.2 shows that the exchange coupling J can vary both in magnitude and sign when the diradical molecule is confined between two electrodes. Even though the molecules are identical, we cannot control the way they are positioned in the junction. As a result, the influence of the electrodes and the substrate on the molecule will be different in every junction. For example, the tunnel coupling from the molecule to the electrodes can vary significantly, as can be seen in Figure 3.2a and b where the $\mathrm{d}I/\mathrm{d}V$ differs by three orders of magnitude. Also the conformation of the molecule and the strain in the molecule can be strongly influenced by the surroundings, which in turn have a strong effect on the magnitude and sign of the exchange coupling [16, 20].

Apart from the excitations between the singlet state and the triplet states no other features are present. As such — despite the differences in the exchange- and tunnel couplings — the measurements in both Figure 3.2a and Figure 3.2b can be well explained by only considering two exchange-coupled spins and ignoring any other molecular features. We corroborate the validity of this simple description by simulating COT transport through a system of two exchange-coupled spins, of which the results are shown in Figure 3.2c and d.

The code used to perform the simulations is based on the COT model of Ternes (2015) [21]. Within this model, we consider second-order COT between two electrodes through *one* of the two exchange-coupled spins, which we call spin A. The tunnel couplings from the two electrodes to spin A are called Γ_1 and Γ_2. The second spin, spin B, is considered to be uncoupled from the electrodes and only interacts through an exchange coupling, J, with spin A. The Hamiltonian of the (isolated) spin system includes the isotropic exchange-coupling term $J\mathbf{S}_\mathrm{A}\cdot\mathbf{S}_\mathrm{B}$, where $J = 4.5\,\mathrm{meV}$ in Figure 3.2c and $J = -2\,\mathrm{meV}$ in Figure 3.2d), and two Zeeman terms $g\mu_\mathrm{B}\mathbf{B}\cdot\mathbf{S}_\mathrm{A}$ and $g\mu_\mathrm{B}\mathbf{B}\cdot\mathbf{S}_\mathrm{B}$, where $g = 2$. The average occupation of the states and the tunneling current are found using the rate-equation formalism [21] and a background conductance is added manually. We estimate the ratio of the tunnel couplings by matching the simulations with the measurements, particularly focusing on the shape of the excitation steps. A strongly asymmetric coupling re-

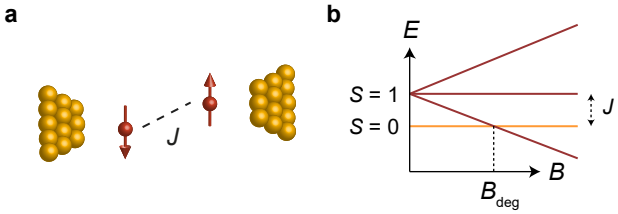

Figure 3.3: a. Schematic representation of a pair of unpaired spins with an exchange coupling J. **b.** Energy (E) diagram of a singlet state and a triplet state as a function of magnetic field B. At $B = B_{\mathrm{deg}} = J/g\mu_{\mathrm{B}}$ the $|S = 1, m = -1\rangle$ state of the triplet becomes degenerate with the $|S = 0, m = 0\rangle$ state. As a result of this degeneracy the singlet-triplet Kondo effect may develop.

sults in flat excitation steps, whereas an increasingly symmetric tunnel coupling leads to a peak-shaped contribution at the step edge [21]. We use this observation to match the simulations and the measurements in Figure 3.2a and b, and obtain $\Gamma_1/\Gamma_2 \sim 2$ and $\Gamma_1/\Gamma_2 \sim 4$, respectively.

The excellent agreement between the experimental data and the simulations in Figure 3.2 shows that the diradical molecule behaves as a model spin system and therefore provides an excellent platform for studying coupled spin pairs on an individual level. A more interesting low-energy spectrum of the diradical can be expected when the exchange coupling is weaker. In that case, one of the $S = 1$ states can be tuned to the same energy as the singlet state by a magnetic field. This magnetic-field-induced spin degeneracy can result in the singlet-triplet Kondo effect, as discussed in Section 3.2.

3.2. THE SINGLET-TRIPLET KONDO EFFECT

The Kondo effect has played an important role in quantum transport since the experimental observations in charge traps [22], single-electron transistors [23] and single-molecule devices [24]. The standard Kondo effect in a quantum dot result from a single spin with $S = 1/2$, which is fully screened by the conducting electrons in the electrodes. When multiple unpaired spins are present, more exotic Kondo effects can occur, e.g., the underscreened Kondo effect [25, 26], the two-stage Kondo effect [27] and the singlet-triplet Kondo effect [28].

The singlet-triplet Kondo effect may occur in a system containing a pair of exchange-coupled spins with $S = 0$, as sketched in Figure 3.3a. An external magnetic field B lifts the degeneracy of the triplet states by the Zeeman effect, as depicted in Figure 3.3b. When the singlet state is the ground state and the magnetic field is set to a field $B_{\mathrm{deg}} = J/g\mu_{\mathrm{B}}$, the energy of the $|S = 1, m = -1\rangle$ state is equal to the energy of the $|S = 0, m = 0\rangle$ state (see Figure 3.3). Even though the number of spins is even, a fully-screened Kondo effect may arise due to the magnetic-field-induced doubly-degenerate ground state. We refer to this phenomenon as the *singlet-triplet Kondo effect*.

In Figure 3.4 we present transport measurements of a diradical single-molecule device which exhibits the singlet-triplet Kondo effect. Figure 3.4a shows a $\mathrm{d}I/\mathrm{d}V$ map as a

function of V and V_g. A step in the dI/dV is present at $V = \pm 0.76\,\text{mV}$ which corresponds to a cotunneling (COT) excitation (see Section 2.2). Towards the left and right edge of the map the overall dI/dV increases, which can occur when the gate voltage is tuned towards a charge degeneracy point. However, within the limited accessible gate-voltage range no charge transitions could be observed. This means that the charge of the diradical in this map is fixed and sequential electron tunneling (SET) processes do not play a role. Instead, transport is governed by COT processes (see Section 2.1 and Section 2.2 for a more detailed discussion on SET and COT transport).

The magnetic-field dependence of the dI/dV spectra are shown in Figure 3.4c and d, for $V_g = -1.7\,\text{V}$ and $V_g = -2.8\,\text{V}$, respectively. Figure 3.4c shows that the COT step at $V = \pm 0.7\,\text{mV}$ splits in three with increasing B, in a linear way. This behavior is consistent with a singlet ground state as depicted in Figure 3.2.

As the exchange coupling is $J = 0.76\,\text{meV}$, the value of $B_{\text{deg}} = J/g\mu_B \approx 6.6\,\text{T}$. Here, the energy of $|S = 1, m = -1\rangle$ is equal to the energy of the singlet state. At even higher magnetic fields the $|S = 1, m = -1\rangle$ state becomes the new ground state. The map in Figure 3.4c shows this ground-state transition at $B = 6.6\,\text{T}$ where the excitation energy to the $|S = 1, m = -1\rangle$ state reaches zero. For $B > 6.6\,\text{T}$ only two excitations remain, as is expected for a triplet ground state (see the scheme in Figure 3.3d and the maps in Figure 3.2b and d).

In Figure 3.4c, all features can be qualitatively explained by COT through a two-spin system, like in Figure 3.2. The same measurement at $V_g = -2.8\,\text{V}$ shown in Figure 3.4d, however, exhibits significantly different behavior. The COT excitation steps appear as peaks rather than steps. In addition, a zero-bias peak develops around the singlet-triplet degeneracy at $B_{\text{deg}} = 6.6\,\text{T}$. Figure 3.4e and f show bias traces at selected B-values, in which the development of the zero-bias peak can be seen more clearly.

We explain the appearance of the peak-shaped COT excitations at strongly negative gate voltages as follows: By setting the gate voltage to more negative values the dI/dV increases, which suggests that the single-molecule device is approaching a charge degeneracy point, i.e., a point where the chemical potential of the single-molecule device equals the Fermi level of the electrodes. In other words, the *level alignment* is decreasing. The level alignment is an important parameter in determining the strength of the Kondo effect — when the level alignment decreases the strength of the Kondo effect increases [29]. Stronger Kondo coupling leads to a larger contribution of third-order COT processes which in turn gives rise to the appearance of COT excitation *peaks* rather than steps [21].

The development of the zero-bias peak at the singlet-triplet degeneracy also appears as a result of the stronger Kondo coupling and can be interpreted as a special type of Kondo resonance. We refer to the appearance of a Kondo resonance at a magnetic-field-induced singlet-triplet degeneracy point as the *singlet-triplet Kondo effect*. Even though different spin states are involved in the singlet-triplet Kondo effect and the standard Kondo effect, the screening is expected to behave similarly [1]. The magnetic-field-induced degeneracy with an average spin $\langle S \rangle = 1/2$ can be screened in the same manner, albeit at a finite magnetic field.

We present an additional dI/dV map in Figure 3.4b where the dI/dV at zero bias is plotted as a function of V_g and B. This map shows in more detail the development of

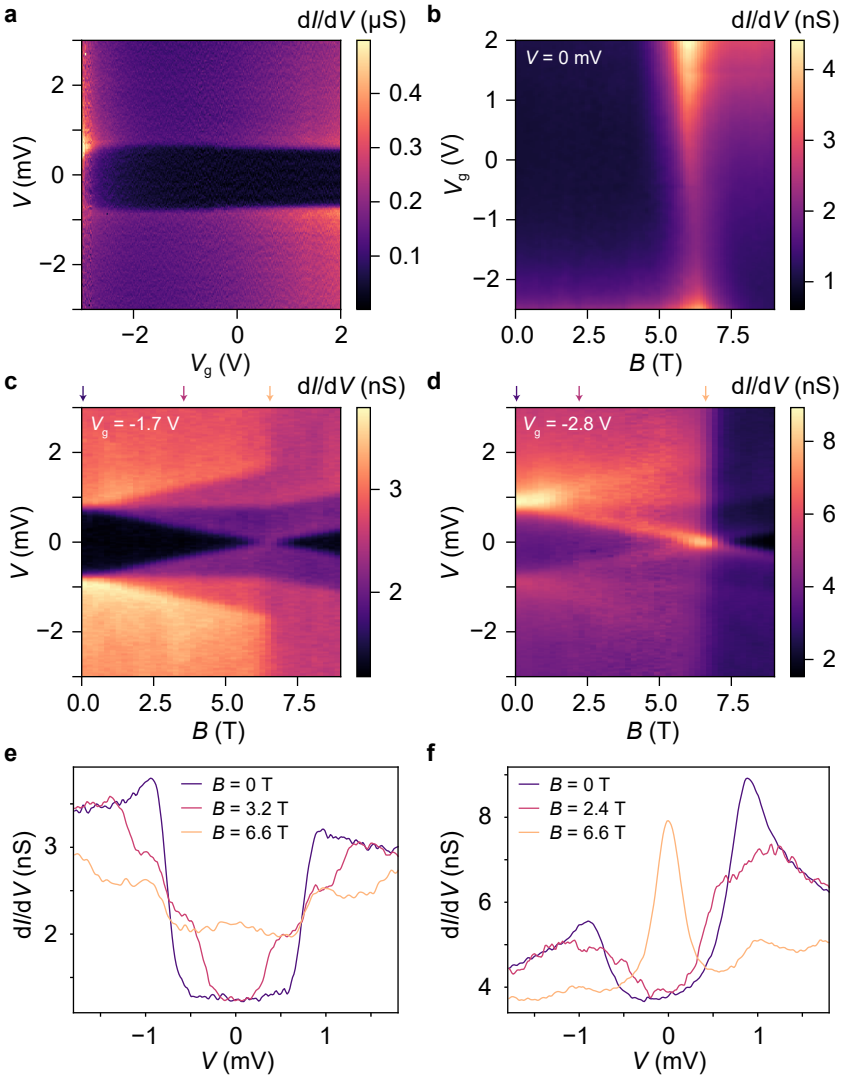

Figure 3.4: a. Differential conductance ($\mathrm{d}I/\mathrm{d}V$) map showing the bias- and gate-voltage dependence of a diradical single-molecule device in a single charge state. **b.** $\mathrm{d}I/\mathrm{d}V$ as a function of B and V_g at zero bias. An enhancement of the $\mathrm{d}I/\mathrm{d}V$ appears at $B = 6.6\,\mathrm{T}$ due to the singlet-triplet Kondo effect. **c.** and **d.** Magnetic-field evolution of the $\mathrm{d}I/\mathrm{d}V$ spectra measured at $V_\mathrm{g} = -1.7\,\mathrm{V}$ and $V_\mathrm{g} = -2.8\,\mathrm{V}$, respectively, showing the COT spin excitations between the singlet state and the triplet states. In **d.** the singlet-triplet Kondo resonance appears at $B = 6.6\,\mathrm{T}$. **e.** and **f.** Selected bias-voltage traces from **c.** and **d.**

the Kondo resonance with magnetic field and gate voltage. Around $B = 6.6\,\mathrm{T}$ the Kondo resonance appears a vertical line across the whole gate voltage range. The change in intensity of this line reflects the variation in the strength of the Kondo effect as a function of V_g.

3.3. ANOMALOUS TEMPERATURE DEPENDENCE OF THE SINGLET-TRIPLET KONDO EFFECT

In a simple model of two spins coupled by an isotropic exchange coupling, the singlet-triplet Kondo effect behaves in the same way as a standard spin-1/2 Kondo effect [1]. Accordingly, the linear conductance as a function of temperature is expected to follow the commonly-used universal curve [30]:

$$G(T) = G_0 \left(\frac{T_K'^2}{T^2 + T_K'^2} \right)^s + G_b, \tag{3.1}$$

where $T_K' = T_K / \sqrt{2^{1/s} - 1}$, with T_K being the Kondo temperature, G_b the background conductance and $s = 0.2$. To experimentally obtain $G(T)$, we recorded $\mathrm{d}I/\mathrm{d}V$ spectra at fixed $B = 6.6\,\mathrm{T}$ and $V_g = -2.8\,\mathrm{V}$ at various temperatures. The measured $\mathrm{d}I/\mathrm{d}V$ spectra are shown in Figure 3.5a. The linear conductance was determined by fitting the Kondo peaks to Lorentzian functions and by extracting the peak height to estimate $G(T) - G_b$. The obtained values are normalized to the saturation conductance G_{max} and plotted in Figure 3.5b, along with the universal curve of Equation (3.1) and a modified universal curve with $s = 0.7$. The temperature T is normalized by $T_K = 0.6\,\mathrm{K}$, which is the temperature at which the conductance reaches $0.5 G_{max}$. Remarkably, the experimental data strongly deviates from the universal curve for a standard spin-1/2 system ($s = 0.2$). A good agreement with the experimental data is found by choosing a significantly higher value for the empirical parameter s, which illustrates the anomalous behavior of this Kondo effect.

An explanation for the anomalous temperature dependence can be obtained by considering the presence of an anisotropic exchange coupling between the two spins of the diradical [1]. Besides the isotropic Heisenberg coupling, a coupling of the form:

$$H_A = -2\sqrt{2}\Delta_A(\hat{\mathbf{S}}_1^x \hat{\mathbf{S}}_2^z - \hat{\mathbf{S}}_1^z \hat{\mathbf{S}}_2^x), \tag{3.2}$$

known as the Dzyaloshinskii-Moriya interaction, can alter the universal Kondo curve. It can be shown that for increasing Δ_A the temperature dependence of the linear conductance at a Kondo peak can no longer be fitted by Equation (3.1). Accurate fits could only be obtained upon using significantly higher s-values [1], as in Figure 3.5b.

At this stage we cannot rule out other scenarios and more detailed measurements would be needed to verify the presence of an anisotropic exchange coupling. For example, as Equation (3.2) mixes the singlet and the triplet states of the two-spin system, an avoided crossing can be expected at the singlet-triplet ground state transition in e.g. Figure 3.4c. In the performed measurements we do not have the resolution to rule out or verify the presence of such an avoided crossing however. Nevertheless, the anisotropic exchange coupling provides a plausible explanation for the anomalous temperature dependence which can be of general interest in other exchange-coupled spin systems.

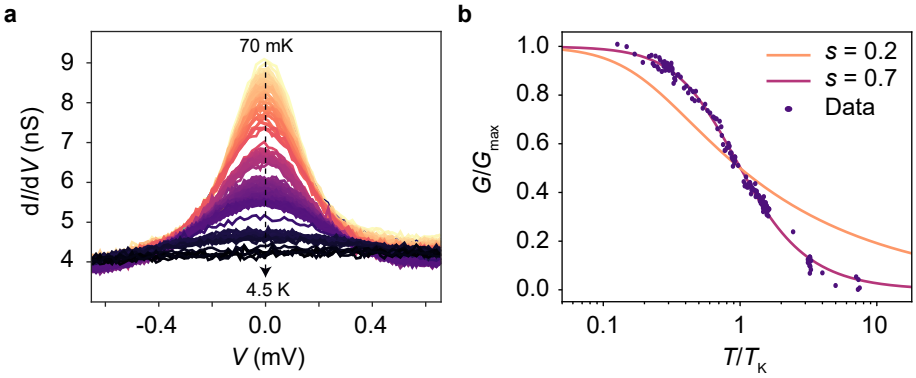

Figure 3.5: a. Experimental $\mathrm{d}I/\mathrm{d}V$ spectra recorded at different temperatures ranging from $T = 70\,\mathrm{mK}$ to $T = 4.5\,\mathrm{K}$ **b.** Temperature dependence of the linear conductance (purple dots), obtained by fitting the peaks in **a** to Lorentzian functions and extracting the peak height. The universal curve of Equation (3.1) for the standard value of $s = 0.2$ and a modified value of $s = 0.7$ is plotted for comparison with the experimental data.

3.4. SIGNATURES OF A TWO-STAGE KONDO EFFECT

We already discussed in Section 3.2 that a double-spin system can exhibit a type of Kondo effect when the spins are coupled antiferromagnetically, such that the ground state is a spin singlet and a singlet-triplet degeneracy can be induced by a magnetic field. A different type of Kondo screening can occur in double-spin systems where the exchange coupling is ferromagnetic. Then, the total spin of the ground state is $S = 1$. It is known that this spin can be partially screened by a single electrode, whereby the spin is reduced from $S = 1$ to $S = 1/2$. This phenomenon is known as the *underscreened* Kondo effect [25, 26] and occurs below a certain Kondo temperature T_{K1}. In rare cases, the remaining $S = 1/2$ is also screened by the conduction electrons below a *second* Kondo temperature $T_{\mathrm{K2}} < T_{\mathrm{K1}}$. Similarly, as a magnetic field suppresses the Kondo effect both stages of Kondo screening are quenched at different critical magnetic fields [31–33].

Since the Kondo temperatures depend exponentially on the tunnel coupling between the spin and their respective lead, it is difficult to realize a system in which T_{K1} and T_{K2} are both within an accessible range. The tunnel coupling is generally asymmetric and the Kondo temperature of the second screening stage T_{K2} may therefore be too low to reach experimentally. Only one stage of screening is observed in that case [25, 26]. Very few experiments have been reported where both T_{K1} and T_{K2} were within experimental reach, such that the *two-stage Kondo effect* could be observed [27]. The diradical molecule could be an eligible host for two-stage Kondo screening. Various devices were observed to be in a spin-triplet ground state as a result of a small and ferromagnetic exchange coupling ($J < 0$, see Figure 3.2b).

In Figure 3.6 we present transport measurements of a diradical single-molecule device which shows signatures of a two-stage Kondo effect. The $\mathrm{d}I/\mathrm{d}V$ map shown in Figure 3.6a shows two charge degeneracy points, one at $V_{\mathrm{g}} = -2\,\mathrm{V}$ and the other around $V_{\mathrm{g}} = -0.5\,\mathrm{V}$. At the far right of the $\mathrm{d}I/\mathrm{d}V$ map a zero-bias peak appears which splits in

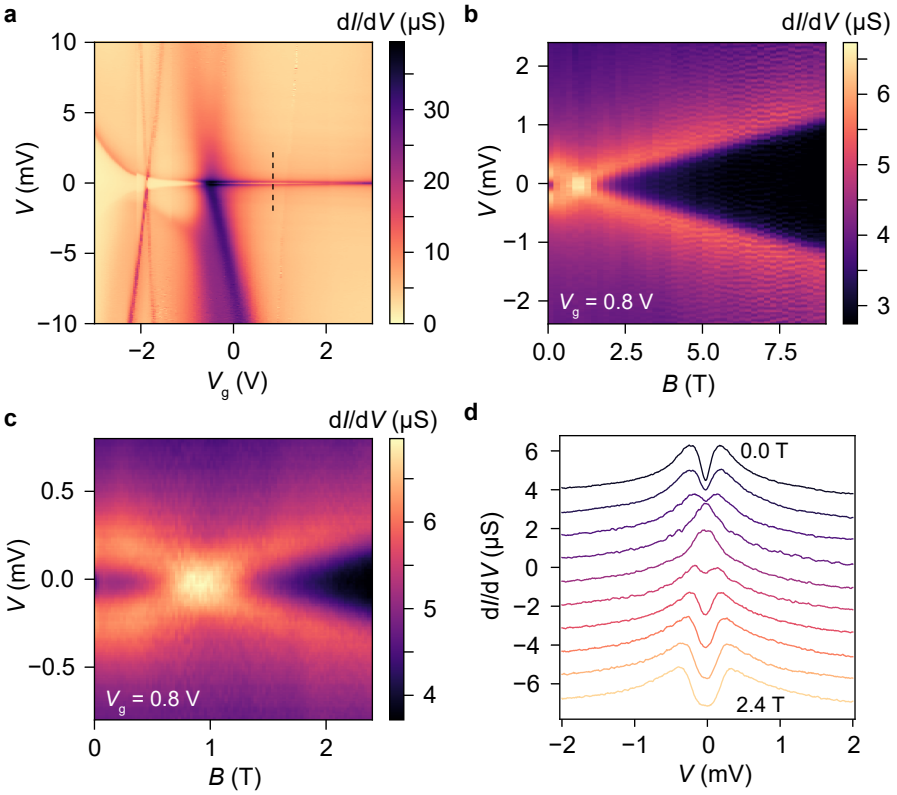

Figure 3.6: a. Differential conductance ($\mathrm{d}I/\mathrm{d}V$) map of a diradical single-molecule device, where two charge degeneracy points are observed along with a zero-bias peak at high gate voltage that splits as V_g is decreased. **b.** Magnetic-field dependence of the $\mathrm{d}I/\mathrm{d}V$ spectrum at $V_\mathrm{g} = 0.8\,\mathrm{V}$ (indicated by dashed line in **a.**) showing a peak-dip structure at $B = 0\,\mathrm{T}$ which evolves into a zero-bias peak around 1 T. Above 1 T he zero-bias peak splits linearly with B. **c.** Detailed measurement of the low bias and low magnetic field range of **b.**, showing the magnetic-field evolution more clearly. **d.** Individual $\mathrm{d}I/\mathrm{d}V$ line spectra taken from the same data set as **c**. The traces are vertically offset for clarity.

two as the gate voltage is lowered. In the following we focus on the magnetic-field dependence of this split zero-bias peak at a fixed gate voltage of $V_g = 0.8\,\mathrm{V}$, marked by the dashed line in the $\mathrm{d}I/\mathrm{d}V$ map.

Figure 3.6b shows the evolution of the $\mathrm{d}I/\mathrm{d}V$ spectrum with magnetic field. The peak-dip structure centered at zero bias turns into a single peak around $B = 1\,\mathrm{T}$. At higher B, the zero-bias peak splits again in a linear way up to the maximum field. A more detailed measurement of the low-B region is presented in Figure 3.6c, which shows the peculiar shape of the excitation spectrum more clearly. From zero field up to 1 T, the two peaks at $V = \pm 0.2\,\mathrm{mV}$ merge in a slightly non-linear way. No other excitation peaks or steps are observed in this measurement. This can be seen in a different way by the bias-voltage line traces shown in Figure 3.6d, which are taken from the same measurement as Figure 3.6c.

The peculiar magnetic-field dependence of this device cannot be explained by a simple COT model of exchange-coupled spins, as in Figure 3.2. Instead, the data bears a striking resemblance with experimental observations of the two-stage Kondo effect [27]. Within this interpretation, the peak-dip structure at zero field emerges due to the two stages of Kondo screening. As the magnetic field is increased the second stage of Kondo screening is quenched before the first stage, which results in the appearance of a single peak at an intermediate field — in Figure 3.6c at $B = 1\,\mathrm{T}$. At higher magnetic fields the second stage of Kondo screening is also quenched and the Kondo resonance splits again [31]. This expected behavior for the two-stage Kondo effect is consistent with the experimental data shown in Figure 3.6. We note that with the experimental setup used for these measurements we were not able to obtain an accurate measurement of the temperature dependence over a wide temperature range, which would be required to corroborate the proposed interpretation [33].

3.5. CONCLUDING REMARKS

In this chapter we presented transport measurements of diradical single-molecule devices which exhibit various spin-related transport phenomena. From spin-flip IETS measurements we could determine that the exchange coupling between the two unpaired spins of the molecule varied from device to device, both in magnitude as well as in sign. Various spectra could be understood in terms of an elementary COT model, only considering the exchange coupling and the Zeeman interaction. This model behavior makes the diradical molecule an attractive platform for studies of more complex spin-related phenomena, such as the singlet-triplet Kondo effect and the two-stage Kondo effect discussed in Section 3.2 and Section 3.4, respectively. The singlet-triplet Kondo effect was observed at a magnetic-field induced singlet-triplet degeneracy. Temperature dependent measurements of the Kondo resonance showed an unexpected deviation from the universal curve. We discussed how this anomaly could be explained by considering an anisotropic exchange coupling between the spins [1]. A different device exhibited the expected behavior of the rarely observed two-stage Kondo effect. At zero magnetic field a peak-dip structure was observed which, as the magnetic field was increased, evolved into a single peak that subsequently split at even higher magnetic fields. The disappearance of the dip and the subsequent splitting of the peak reflect the breakdown of the two

stages of Kondo screening. The exceptionally clean data demonstrates the suitability for this type of molecule to be used as a platform for experimentally verifying theoretical predictions.

Finally we note that the well-understood two-spin behavior makes diradical molecules attractive systems for transport studies with superconducting electrodes. The interplay between superconductivity and exchange-coupled two-spin systems are predicted to have rich phase diagrams [34, 35], which could potentially be explored by embedding the diradical molecule in the superconducting devices discussed in Chapter 6.

REFERENCES

[1] P. Zalom, **J. de Bruijckere**, R. Gaudenzi, H. S. J. van der Zant, T. Novotný, and R. Korytár. "Magnetically Tuned Kondo Effect in a Molecular Double Quantum Dot: Role of the Anisotropic Exchange". *The Journal of Physical Chemistry C* 123.18 (Apr. 2019), pp. 11917–11925. DOI: 10.1021/acs.jpcc.9b00783.

[2] R. Gaudenzi, **J. de Bruijckere**, D. Reta, I. de P. R. Moreira, C. Rovira, J. Veciana, H. S. J. van der Zant, and E. Burzurí. "Redox-Induced Gating of the Exchange Interactions in a Single Organic Diradical". *ACS Nano* 11.6 (May 2017), pp. 5879–5883. DOI: 10.1021/acsnano.7b01578.

[3] N. S. Lai, W. H. Lim, C. H. Yang, F. A. Zwanenburg, W. A. Coish, F. Qassemi, A. Morello, and A. S. Dzurak. "Pauli Spin Blockade in a Highly Tunable Silicon Double Quantum Dot". *Scientific Reports* 1.1 (Oct. 2011). DOI: 10.1038/srep00110.

[4] H. Jeong. "The Kondo Effect in an Artificial Quantum Dot Molecule". *Science* 293.5538 (Sept. 2001), pp. 2221–2223. DOI: 10.1126/science.1063182.

[5] S. D. Sarma, J. Fabian, X. Hu, and I. Žutić. "Spintronics: electron spin coherence, entanglement, and transport". *Superlattices and Microstructures* 27.5-6 (May 2000), pp. 289–295. DOI: 10.1006/spmi.2000.0829.

[6] D. P. DiVincenzo. "Double Quantum Dot as a Quantum Bit". *Science* 309.5744 (Sept. 2005), pp. 2173–2174. DOI: 10.1126/science.1118921.

[7] F. Kuemmeth, H. O. H. Churchill, P. K. Herring, and C. M. Marcus. "Carbon nanotubes for coherent spintronics". *Materials Today* 13.3 (Mar. 2010), pp. 18–26. DOI: 10.1016/s1369-7021(10)70030-4.

[8] N. Mason. "Local Gate Control of a Carbon Nanotube Double Quantum Dot". *Science* 303.5658 (Jan. 2004), pp. 655–658. DOI: 10.1126/science.1093605.

[9] B. M. Maune, M. G. Borselli, B. Huang, T. D. Ladd, P. W. Deelman, K. S. Holabird, A. A. Kiselev, I. Alvarado-Rodriguez, R. S. Ross, A. E. Schmitz, M. Sokolich, C. A. Watson, M. F. Gyure, and A. T. Hunter. "Coherent singlet-triplet oscillations in a silicon-based double quantum dot". *Nature* 481.7381 (Jan. 2012), pp. 344–347. DOI: 10.1038/nature10707.

[10] J. R. Petta. "Coherent Manipulation of Coupled Electron Spins in Semiconductor Quantum Dots". *Science* 309.5744 (Sept. 2005), pp. 2180–2184. DOI: 10.1126/science.1116955.

[11] F. Molitor, S. Dröscher, J. Güttinger, A. Jacobsen, C. Stampfer, T. Ihn, and K. Ensslin. "Transport through graphene double dots". *Applied Physics Letters* 94.22 (June 2009), p. 222107. DOI: 10.1063/1.3148367.

[12] C. Fasth, A. Fuhrer, M. T. Björk, and L. Samuelson. “Tunable Double Quantum Dots in InAs Nanowires Defined by Local Gate Electrodes”. *Nano Letters* 5.7 (July 2005), pp. 1487–1490. DOI: 10.1021/nl050850i.

[13] M. Koole, J. C. Hummelen, and H. S. J. van der Zant. “Spin excitations in an all-organic double quantum dot molecule”. *Physical Review B* 94.16 (Oct. 2016). DOI: 10.1103/physrevb.94.165414.

[14] J. Veciana, C. Rovira, N. Ventosa, M. I. Crespo, and F. Palacio. “Stable polyradicals with high-spin ground states. 2. Synthesis and characterization of a complete series of polyradicals derived from 2,4,6 - trichloro - α,α,α',α',α'',α'' - hexakis(pentachlorophenyl)mesitylene with S = 1/2, 1, and 3/2 ground states”. *Journal of the American Chemical Society* 115.1 (Jan. 1993), pp. 57–64. DOI: 10.1021/ja00054a008.

[15] R. Frisenda, R. Gaudenzi, C. Franco, M. Mas-Torrent, C. Rovira, J. Veciana, I. Alcon, S. T. Bromley, E. Burzurí, and H. S. J. van der Zant. “Kondo Effect in a Neutral and Stable All Organic Radical Single Molecule Break Junction”. *Nano Letters* 15.5 (Apr. 2015), pp. 3109–3114. DOI: 10.1021/acs.nanolett.5b00155.

[16] R. Gaudenzi, E. Burzurí, D. Reta, I. de P. R. Moreira, S. T. Bromley, C. Rovira, J. Veciana, and H. S. J. van der Zant. “Exchange Coupling Inversion in a High-Spin Organic Triradical Molecule”. *Nano Letters* 16.3 (Feb. 2016), pp. 2066–2071. DOI: 10.1021/acs.nanolett.6b00102.

[17] H. Park, A. K. L. Lim, A. P. Alivisatos, J. Park, and P. L. McEuen. “Fabrication of metallic electrodes with nanometer separation by electromigration”. *Applied Physics Letters* 75.2 (July 1999), pp. 301–303. DOI: 10.1063/1.124354.

[18] K. O’Neill, E. A. Osorio, and H. S. J. van der Zant. “Self-breaking in planar few-atom Au constrictions for nanometer-spaced electrodes”. *Applied Physics Letters* 90.13 (Mar. 2007), p. 133109. DOI: 10.1063/1.2716989.

[19] R. Gaudenzi, M. Misiorny, E. Burzurí, M. R. Wegewijs, and H. S. J. van der Zant. “Transport mirages in single-molecule devices”. *The Journal of Chemical Physics* 146.9 (Mar. 2017), p. 092330. DOI: 10.1063/1.4975767.

[20] E. Burzurí, A. García-Fuente, V. García-Suárez, K. S. Kumar, M. Ruben, J. Ferrer, and H. S. J. van der Zant. “Spin-state dependent conductance switching in single molecule-graphene junctions”. *Nanoscale* 10.17 (2018), pp. 7905–7911. DOI: 10.1039/c8nr00261d.

[21] M. Ternes. “Spin excitations and correlations in scanning tunneling spectroscopy”. *New Journal of Physics* 17.6 (June 2015), p. 063016. DOI: 10.1088/1367-2630/17/6/063016.

[22] D. C. Ralph and R. A. Buhrman. “Kondo-assisted and resonant tunneling via a single charge trap: A realization of the Anderson model out of equilibrium”. *Physical Review Letters* 72.21 (May 1994), pp. 3401–3404. DOI: 10.1103/physrevlett.72.3401.

[23] D. Goldhaber-Gordon, H. Shtrikman, D. Mahalu, D. Abusch-Magder, U. Meirav, and M. A. Kastner. “Kondo effect in a single-electron transistor”. *Nature (London)* 391.6663 (Jan. 1998), pp. 156–159. DOI: 10.1038/34373.

[24] W. Liang, M. P. Shores, M. Bockrath, J. R. Long, and H. Park. “Kondo resonance in a single-molecule transistor”. *Nature (London)* 417.6890 (June 2002), pp. 725–729. DOI: 10.1038/nature00790.

[25] J. J. Parks, A. R. Champagne, T. A. Costi, W. W. Shum, A. N. Pasupathy, E. Neuscamman, S. Flores-Torres, P. S. Cornaglia, A. A. Aligia, C. A. Balseiro, G. K.-L. Chan, H. D. Abruna, and D. C. Ralph. “Mechanical Control of Spin States in Spin-1 Molecules and the Underscreened Kondo Effect”. *Science* 328.5984 (June 2010), pp. 1370–1373. DOI: 10.1126/science.1186874.

[26] N. Roch, S. Florens, T. A. Costi, W. Wernsdorfer, and F. Balestro. “Observation of the Underscreened Kondo Effect in a Molecular Transistor”. *Physical Review Letters* 103.19 (Nov. 2009). DOI: 10.1103/physrevlett.103.197202.

[27] W. G. van der Wiel, S. D. Franceschi, J. M. Elzerman, S. Tarucha, L. P. Kouwenhoven, J. Motohisa, F. Nakajima, and T. Fukui. “Two-Stage Kondo Effect in a Quantum Dot at a High Magnetic Field”. *Physical Review Letters* 88.12 (Mar. 2002). DOI: 10.1103/physrevlett.88.126803.

[28] J. Nygård, D. H. Cobden, and P. E. Lindelof. “Kondo physics in carbon nanotubes”. *Nature* 408.6810 (Nov. 2000), pp. 342–346. DOI: 10.1038/35042545.

[29] S. M. Cronenwett. “A Tunable Kondo Effect in Quantum Dots”. *Science* 281.5376 (July 1998), pp. 540–544. DOI: 10.1126/science.281.5376.540.

[30] D. Goldhaber-Gordon, J. Göres, M. A. Kastner, H. Shtrikman, D. Mahalu, and U. Meirav. “From the Kondo Regime to the Mixed-Valence Regime in a Single-Electron Transistor”. *Physical Review Letters* 81.23 (Dec. 1998), pp. 5225–5228. DOI: 10.1103/physrevlett.81.5225.

[31] M. Pustilnik and L. I. Glazman. “Kondo Effect in Real Quantum Dots”. *Physical Review Letters* 87.21 (Nov. 2001). DOI: 10.1103/physrevlett.87.216601.

[32] W. Hofstetter and H. Schoeller. “Quantum Phase Transition in a Multilevel Dot”. *Physical Review Letters* 88.1 (Dec. 2001). DOI: 10.1103/physrevlett.88.016803.

[33] R. Žitko. “Fano-Kondo effect in side-coupled double quantum dots at finite temperatures and the importance of two-stage Kondo screening”. *Physical Review B* 81.11 (Mar. 2010). DOI: 10.1103/physrevb.81.115316.

[34] N. Y. Yao, C. P. Moca, I. Weymann, J. D. Sau, M. D. Lukin, E. A. Demler, and G. Zaránd. “Phase diagram and excitations of a Shiba molecule”. *Physical Review B* 90.24 (Dec. 2014). DOI: 10.1103/physrevb.90.241108.

[35] K. Grove-Rasmussen, G. Steffensen, A. Jellinggaard, M. H. Madsen, R. Žitko, J. Paaske, and J. Nygård. “Yu-Shiba-Rusinov screening of spins in double quantum dots”. *Nature Communications* 9.1 (June 2018). DOI: 10.1038/s41467-018-04683-x.

4

MOLECULAR TRIPLE-SPIN SYSTEMS

After discussing single pairs of exchange-coupled spins in Chapter 3 we continue in this chapter with molecular systems containing three spins. We focus on a diradical single-molecule that could be electrostatically charged to obtain a stable molecular triple-spin system. Radical molecules are commonly known to be highly reactive and short-lived, making this molecule an exceptionally odd case. The charged diradical molecule can be used as a platform to study transport through three-spin systems. The analysis in this chapter shows that the exchange couplings between the radical spins cannot be determined from the measured excitation energies alone — as in the case of two-spin systems. Additional information is required and we propose an approach to extract this information based on the intensity of the cotunneling excitations. This approach can potentially be used in the analysis of other three-spin systems where obtaining the exchange couplings can lead to a better understanding of the system's orbital structure.

Parts of this chapter have been published in [1].

In this chapter we go up one step in complexity by adding a single spin to the same type of diradical molecule [2] as discussed in Chapter 3. We show that the added spin remarkably preserves the radical character of the diradical molecule and that we can probe the rich spin-excitation spectrum of a three-spin system, which includes two spin-doublets and a spin-quartet state. By analyzing the energies of the spin excitations as well as their intensity, we can estimate the most likely configuration of the molecular three-spin system.

Three-spin systems or — more generally — triple quantum dots have been realized experimentally in two-dimensional electron gases [3], semiconductor nanowires [4], silicon [5] and organic triradical molecules [6], where the latter belongs to the same family of molecules as the molecule used in this chapter. The interest in these devices arises from the potential charge-transport applications, such as charge rectification [7] and creating separated currents of spin-entangled electrons [8]. Additionally, in quantum computer architectures triple quantum dots can serve e.g. as coded qubits that can be fully controlled by electric fields [9] and as spin qubit clusters which can act without local spin control [10]. The analysis of the exchange couplings discussed in Section 4.4 is not restricted to molecular systems and could potentially be valuable in studies of other triple quantum dots.

4.1. CHARGING THE DIRADICAL MOLECULE

The transport measurements discussed in Chapter 3 were recorded in a single charge state of the diradical molecule. Electrostatic oxidation or reduction did not occur within the accessible gate voltage range. The inability to change the charge state of a single-molecule junction is not uncommon. The charging energy and quantum level spacing are high compared to other nanoscale objects [11], which reduces the chance of being able to access even a single charge-degeneracy point. Whether the molecule can be charged depends on the distance in energy between the molecule's chemical potential and the Fermi level of the electrodes. We refer to this distance as the level alignment ε. The gate voltage required to charge the molecule is (up to a sign) given by: $\alpha\varepsilon$, where α is the gate-coupling parameter. Both parameters depend strongly on the microscopic details of the single-molecule junction: The surrounding electrodes and the substrate affect the charge distribution and the conformation of the molecule, which in turn affect ε. The distance of the molecule to the gate electrode and the amount of charge screening by the electrodes determine α.

In one diradical single-molecule device the microscopic details of the junction allowed for changing the charge state of the molecule by the gate electrode. The level alignment happened to be close to zero energy, which enabled performing detailed transport measurements in the two accessible charge states. As will be discussed in Section 4.3, a third unpaired spin is added to the molecule upon charging. This process is reversible and — as long as the gate voltage is maintained — stable. Figure 4.1b schematically depicts the charging events between the neutral two-spin system and the reduced three-spin system.

Figure 4.1a shows a *stability diagram* of the diradical single-molecule device, i.e., a

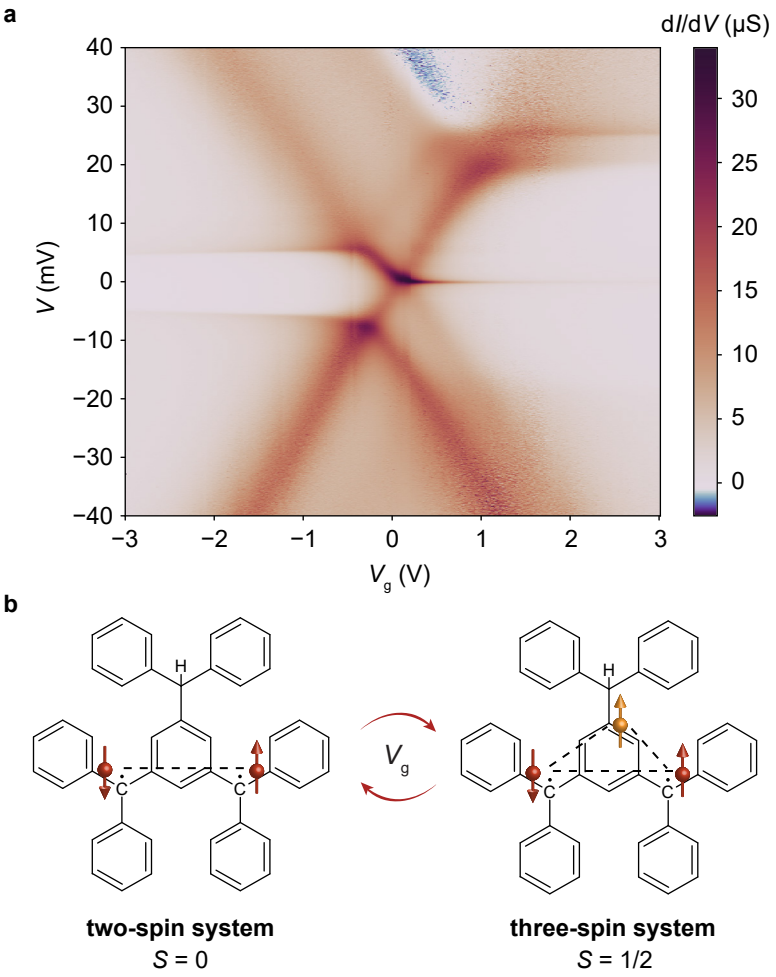

Figure 4.1: a. The measured dI/dV map of a diradical single-molecule device as a function of the bias voltage V and the gate voltage V_g, recorded at zero magnetic field. A single charge degeneracy point appears close to $V_g = 0$ V, which separates two Coulomb-blockaded regions on the left and on the right side. COT excitations can be seen on both sides, some of which continue in the sequential-electron tunneling (SET) regions above and below the charge degeneracy point where the Coulomb blockade is lifted. **b.** Molecular structures of the neutral (left) and reduced (right) diradical molecule. The curved arrows represent the reversible tuning by the gate electrode from a two-spin system with a ground-state total spin $S = 0$ to a three-spin system with $S = 1/2$.

$\mathrm{d}I/\mathrm{d}V$ map as a function of V and V_g. The stability diagram includes (among other features) two slanted lines which cross at zero bias and at $V_\mathrm{g} \approx 0\,\mathrm{V}$. We refer to these slanted lines as the *Coulomb edges*, which cross at a *charge degeneracy point*. The Coulomb edges separate two Coulomb-blockaded regions on the left and on the right side of the charge degeneracy point. In these regions the number of electrons on the molecule is stable and transport is governed by cotunneling (COT) processes (see Section 2.2).

The horizontal lines at $V \approx \pm 5\,\mathrm{mV}$ in the left Coulomb-blockaded region result from inelastic COT. When the bias voltage reaches the excitation energy from the ground state to an excited state the $\mathrm{d}I/\mathrm{d}V$ increases due to the opening of a transport channel *via* that excited state. In the right Coulomb-blockaded region COT excitation lines appear at different bias voltages: In the positive bias region at $V = 20\,\mathrm{mV}$ and 25 mV, and in the negative bias region more faintly at $V = -22\,\mathrm{mV}$ and $-19\,\mathrm{mV}$. In addition, a horizontal zero-bias line appears, which resembles a Kondo resonance [12].

The regions above and below the charge degeneracy point, separated from the COT regions by the Coulomb edges, belong to the *sequential-electron-tunneling* (SET) regime (see Section 2.1). The Coulomb blockade is lifted in this region and charge fluctuations by single electrons are allowed. The COT excitations from the left Coulomb-blockaded region at $V \approx \pm 5\,\mathrm{mV}$ continue as SET excitations — following the same slope as the Coulomb-blockade edges — in the top and bottom SET regions. The COT line at $V = 20\,\mathrm{mV}$ on the right side, also continues in the top SET region. A negative differential conductance (NDC) line appears which starts where the COT excitation at $V = 25\,\mathrm{mV}$ crosses the Coulomb edge. The opening of this SET excitation channel reduces the current, which implies that the transition rates to the corresponding excited state are relatively low.

In the following sections we analyze the magnetic-field dependence of the COT regions by which we identify the spin structure of the diradical molecule. As we will show, the ground state in the left Coulomb-blockaded region is a spin singlet with a triplet excited state, as in Chapter 3. Therefore, this region most likely corresponds to the neutral charge state of the molecule with a ground state spin $S = 0$. In the right Coulomb-blockaded region the ground state turns out to be a spin doublet ($S = 1/2$) with — remarkably — a second doublet excited state and a quartet excited state. This excitation spectrum cannot be explained by one or two unpaired spins alone. Instead of occupying one of the half-filled radical centers, the added electron resides in a third singly-occupied orbital. This scenario is sketched in Figure 4.1b in which the molecular structure of the diradical molecule is drawn. We highlight the unpaired spins in both the neutral and reduced charge state by the vertical arrows. The curved arrows symbolize the reversible charging by the gate voltage V_g.

4.2. TWO-SPIN SYSTEM — SINGLET GROUND STATE

We first focus on the left side of the diagram and identify the involved spin states by analyzing the magnetic-field dependence of the COT excitations. Figure 4.2a shows the $\mathrm{d}I/\mathrm{d}V$ spectra at different magnetic fields B and at a fixed gate voltage $V_\mathrm{g} = -2.3\,\mathrm{V}$, which corresponds to the left Coulomb-blockaded region in Figure 5.8. The spectrum taken at 0 T shows symmetric steps at $V = \pm 4.65\,\mathrm{mV}$, which can be associated with transitions to

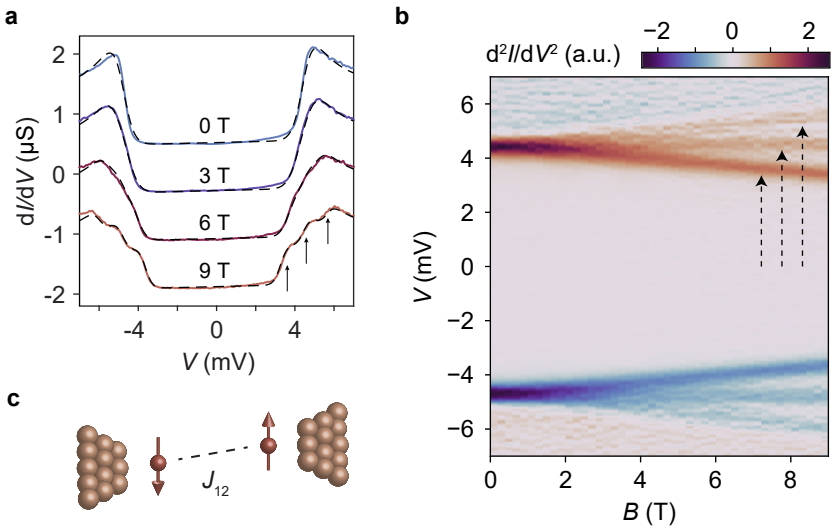

Figure 4.2: a. $\mathrm{d}I/\mathrm{d}V$ spectra of the diradical single-molecule device at fixed $V_g = -2.3\,\mathrm{V}$, measured at different magnetic fields (vertically offset for clarity). Inelastic COT excitation steps appear at $V = \pm 4.65\,\mathrm{mV}$, which split in three (see arrows) as the magnetic field is increased. The black dashed lines show the results of simulated spectra using the tunneling model described in the main text. **b.** Magnetic-field dependence of the excitation spectrum, where the second derivative of the current, the $\mathrm{d}^2I/\mathrm{d}V^2$, is plotted to clarify the linear splitting of the excitations (white arrows). **c.** Sketch of the model exchange-coupled two-spin system coupled to the two electrodes.

excited spin states. The magnetic nature of the transitions follows from the linear shift of the excitation energies as B is increased, which is shown in Figure 4.2b where the second derivative of the current — the $\mathrm{d}^2I/\mathrm{d}V^2$— is plotted for better visibility of the COT lines. The excitations at $V = \pm 4.65\,\mathrm{mV}$ split in three as the magnetic field is increased. This spectrum corresponds with the energy level scheme of Figure 3.1d, where the ground state is a spin singlet and the excited state is a spin triplet. The energy difference between the triplet and the singlet is given by a positive exchange coupling J_{12}, as depicted in Figure 4.2c.

We compare the experimental spectra with numerical simulations based on the tunneling model of Ternes (2015) [13], which is commonly used to simulate $\mathrm{d}I/\mathrm{d}V$ spectra in scanning tunneling spectroscopy. The dashed black lines in Figure 4.2a show the results of these simulations. Within the framework of the model we describe the diradical molecule by a model Hamiltonian with two spin-1/2 centers interacting through a Heisenberg exchange coupling J_{12}. The data is in good agreement with this simulation for all magnetic field values using $J_{12} = 4.65\,\mathrm{meV}$. In order to account for the broadening of the excitations steps we take an effective temperature of 1.4 K. The linear splitting of the steps with increasing magnetic field results from the included Zeeman effect with a g-factor of 2. A linear function with a small slope is added to correct for the observed tilt of the $\mathrm{d}I/\mathrm{d}V$ spectrum, which might be due to density-of-states fluctuations in the

electrodes.

The inelastic COT excitations in Figure 4.2 do not appear as flat steps. Rather, they have a peak-shaped contribution positioned at the bias voltage which corresponds to the excitation energy. This peak-shaped feature can be reproduced within the framework of the tunneling model by two mechanisms: Third-order tunneling processes and non-equilibrium transport effects. Third-order tunneling processes give rise to peak-shaped contributions at bias voltages corresponding to the energy of the intermediate state in the tunneling process [13]. Non-equilibrium effects appear as a result of the non-zero occupations of the excited states, which can be calculated by solving the rate equations of this model. We find that the difference between including non-equilibrium tunneling and third-order tunneling processes is reflected in the relative height of the excitation peaks. Third-order processes yield equal peak-shaped contributions to all three excitation steps, whereas the contribution for non-equilibrium tunneling decreases with increasing energy, as seen in Figure 4.2. We find the best agreement with the data by including only *second-order non-equilibrium* tunneling processes and excluding third-order tunneling processes.

4.3. THREE-SPIN SYSTEM — DOUBLET GROUND STATE

A similar magnetic-field dependent measurement is conducted at fixed $V_g = 3\,\mathrm{V}$, which corresponds to the right Coulomb-blockaded region. Figure 4.3a shows the resulting $\mathrm{d}I/\mathrm{d}V$ spectra recorded at two different magnetic fields. At $B = 0\,\mathrm{T}$, COT excitation steps appear at $V = 25\,\mathrm{mV}$, $20\,\mathrm{mV}$, $-19\,\mathrm{mV}$ and $-22\,\mathrm{mV}$, along with a zero-bias peak. The asymmetry in bias-voltage positions with respect to zero bias and the asymmetry in step heights can be attributed to a V-dependent exchange coupling $J(V)$ and asymmetrically coupled electrodes [14], respectively.

For increasing B, the zero-bias peak splits (see Figure 4.3b) and appears as a dip at $B = 9\,\mathrm{T}$ (see Figure 4.3a). The excitation step at $V = 25\,\mathrm{meV}$ splits in three and the step at $V = 20\,\mathrm{meV}$ in two (see the $\mathrm{d}^2I/\mathrm{d}V^2$ in Figure 4.3e and in the inset of Figure 4.3a). This excitation spectrum is consistent with the energy level diagram of Figure 4.3d, which consists of a ground-state doublet $|D_-\rangle$, an excited-state doublet $|D_+\rangle$ and a quartet $|Q\rangle$. In this picture, the excitations at +20 mV (-19 mV) and +25 mV (-22 mV) correspond to the transitions $|D_-\rangle \rightarrow |D_+\rangle$ and $|D_-\rangle \rightarrow |Q\rangle$, respectively.

The simplest spin system capable of hosting two doublets and one quartet state is the three-spin system schematically depicted in Figure 4.3c. The sketch shows the three spins along with the three exchange couplings between them. The observation of a three-spin $\mathrm{d}I/\mathrm{d}V$ spectrum suggests that the electrostatically added electron — in contrast with e.g. PTM monoradicals [15] and other diradical molecules [16] — occupies an empty orbital, thereby preserving the half-filled occupation of the two radical centers.

4.4. EXCHANGE COUPLING ANALYSIS

The excitation spectrum of the reduced diradical molecule shows features that cannot be reproduced by the COT model used in Section 4.2, such as the zero-bias peak and the prominent excitation peak at $V = 25\,\mathrm{mV}$. These peaks are fingerprints of Kondo

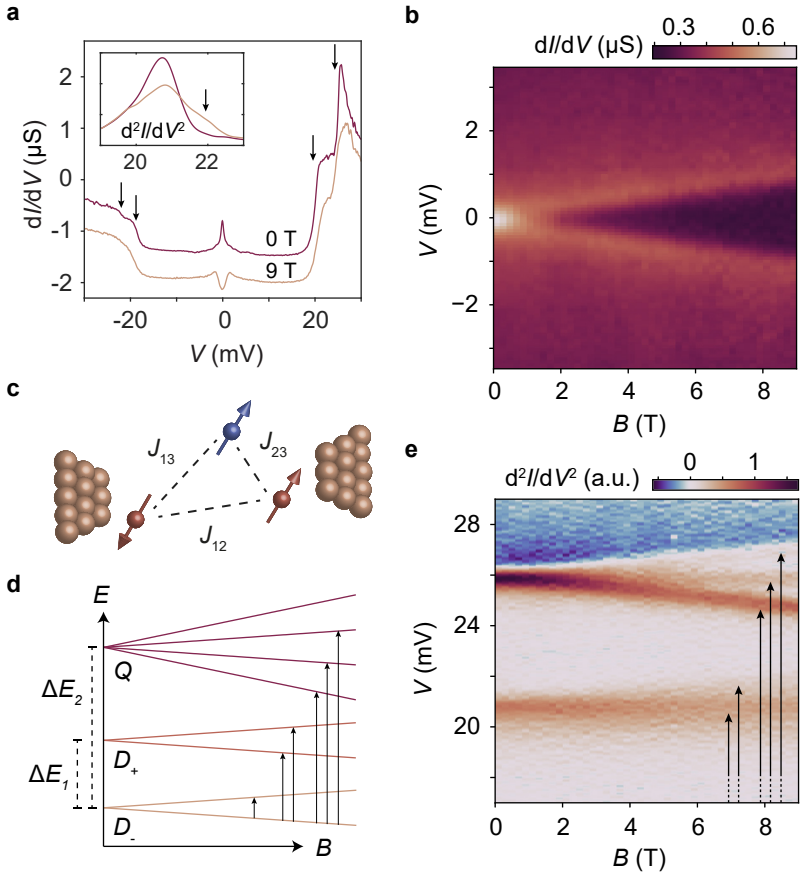

Figure 4.3: a. The $\mathrm{d}I/\mathrm{d}V$ spectra of the diradical single-molecule device in the right Coulomb-blockaded region of Figure 4.1a ($V_g = 3$ V), recorded at $B = 0$ T and $B = 9$ T, showing excitations (see arrows) at -22 mV, -19 mV, 20 mV and 25 mV. The inset shows the $\mathrm{d}^2I/\mathrm{d}V^2$ which clarifies the splitting of the doublet excitation seen in **e.** The zero-bias peak at 0 T becomes a dip at 9 T. **b.** Magnetic-field dependence of the low-bias region, showing the linear splitting of the Kondo peak. **c.** Sketch of a model three-spin system, with the associated exchange couplings J_{12}, J_{13} and J_{23}. **d.** Energy diagram of the accessible spin states in a three-spin system and the associated allowed transitions from the ground state. ΔE_1 and ΔE_2 indicate the zero-field energy differences between the two doublet states, and the quartet and doublet ground state, respectively. **e.** Magnetic-field dependence of the high-bias region of the spin-excitation spectra, showing the transitions (see white arrows) sketched in **d**.

correlations, which can only be modeled by more advanced theoretical techniques [14]. Nevertheless, we can extract valuable information from the dI/dV spectrum within the framework of a simpler model in order to make reasonable estimates of the three spin-exchange couplings.

For the analysis of the spin-excitation spectra we model the three-spin system by the phenomenological Heisenberg-Dirac-Van Vleck (HDVV) Hamiltonian:

$$\hat{\mathscr{H}}^{\mathrm{HDVV}} = J_{12}\hat{\mathbf{S}}_1 \cdot \hat{\mathbf{S}}_2 + J_{13}\hat{\mathbf{S}}_1 \cdot \hat{\mathbf{S}}_3 + J_{23}\hat{\mathbf{S}}_2 \cdot \hat{\mathbf{S}}_3 \tag{4.1}$$

where J_{ij} represents the spin-exchange coupling between spins i and j, and $\hat{\mathbf{S}}_i$ the spin operator of spin i. This system can host three different spin multiplets: one quartet ($|Q\rangle$) and two doublets ($|D_+\rangle$ and $|D_-\rangle$), which can be written as

$$|Q\rangle = \begin{cases} |\uparrow\uparrow\uparrow\rangle & m = \frac{3}{2} \\ (|\uparrow\uparrow\downarrow\rangle + |\uparrow\downarrow\uparrow\rangle + |\downarrow\uparrow\uparrow\rangle)/\sqrt{3} & m = \frac{1}{2} \\ (|\uparrow\downarrow\downarrow\rangle + |\downarrow\uparrow\downarrow\rangle + |\downarrow\downarrow\uparrow\rangle)/\sqrt{3} & m = -\frac{1}{2} \\ |\downarrow\downarrow\downarrow\rangle & m = -\frac{3}{2} \end{cases} \tag{4.2}$$

and

$$|D_\pm\rangle = \begin{cases} \alpha^\pm|\uparrow\uparrow\downarrow\rangle + \beta^\pm|\uparrow\downarrow\uparrow\rangle + \gamma^\pm|\downarrow\uparrow\uparrow\rangle & m = \frac{1}{2} \\ \gamma^\pm|\uparrow\downarrow\downarrow\rangle + \beta^\pm|\downarrow\uparrow\downarrow\rangle + \alpha^\pm|\downarrow\downarrow\uparrow\rangle & m = -\frac{1}{2} \end{cases} \tag{4.3}$$

where the coefficients $\alpha^\pm$, $\beta^\pm$ and $\gamma^\pm$ depend on the values of the exchange couplings.

Whereas the coefficients of the quartet eigenstate are simple numerical factors — as is also the case in the singlet and triplet states of a double-spin system — the coefficients of the doublet eigenstates dependent on the values of the three exchange couplings. The J-dependence disappears once a symmetry is imposed, like $J_{12} = J_{23}$ or any permutation of this equality. Here, we treat the most general case, which remains valid for $J_{12} \neq J_{13} \neq J_{23}$. The eigenenergies that correspond to the spin eigenstates are given by

$$E_Q = (J_{12} + J_{13} + J_{23})/4 \tag{4.4}$$

and

$$E_{D_\pm} = -(J_{12} + J_{13} + J_{23})/4 \pm X/2. \tag{4.5}$$

where

$$X = \sqrt{J_{12}^2 + J_{13}^2 + J_{23}^2 - J_{12}J_{13} - J_{12}J_{23} - J_{13}J_{23}}. \tag{4.6}$$

We note that $X \geq 0$, from which follows that $|D_-\rangle$ is always the lowest-energy doublet. Given that the quartet appears as an excited state in the spin-spectroscopy measurements (see Figure 4.3e) we conclude that $|D_-\rangle$ is the ground state of the three-spin system and the observed multiplet excitations correspond to $|D_-\rangle \rightarrow |D_+\rangle$ and $|D_-\rangle \rightarrow |Q\rangle$. The excitation energies of these transitions follow from equations 4.4 and 4.5:

$$\Delta E_1 \equiv E_{D_+} - E_{D_-} = X, \tag{4.7}$$

$$\Delta E_2 \equiv E_Q - E_{D_-} = (J_{12} + J_{13} + J_{23})/2 + X/2. \tag{4.8}$$

The experimental values we find for ΔE_1 and ΔE_2 are 20 meV and 25 meV, respectively. By equating these values with equations 4.7 and 4.8 we obtain a system of two equations

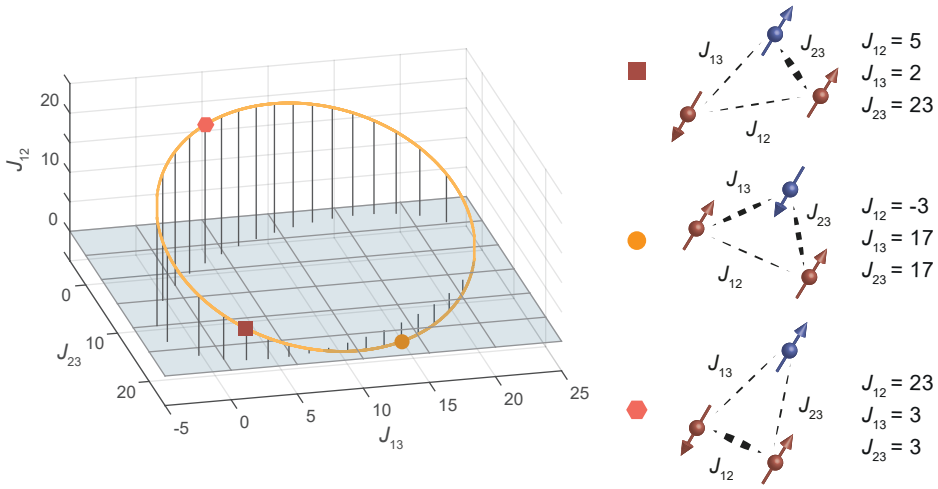

Figure 4.4: Solution set (yellow ellipse) of equations 4.7 and 4.8 in the parameter space spanned by the exchange couplings J_{12}, J_{13} and J_{23} for the experimental values $\Delta E_1 = 20\,\text{meV}$ and $\Delta E_2 = 25\,\text{meV}$. Three scenarios are highlighted: (1, square) Coupling J_{12} remains unchanged upon charging and the added spin 3 couples asymmetrically to spins 1 and 2. (2, circle) One coupling is weakly ferromagnetic and the other two couplings are strongly antiferromagnetic and of similar strength. (3, hexagon) Coupling J_{12} increases significantly upon charging and the added spin 3 is weakly coupled to both spin 1 and spin 2.

with three unknown variables: J_{12}, J_{13} and J_{23}. This system of equations is underdetermined and its solutions form a closed ellipse in the parameter space spanned by the three exchange couplings. All solutions of this underdetermined system of equations with the experimentally obtained values $\Delta E_1 = 20\,\text{meV}$ and $\Delta E_2 = 25\,\text{meV}$ are plotted in Figure 4.4. This figure shows that based on the excitation energies alone one cannot discern between these different solutions.

Even though no single solution can be determined, certain scenarios can be excluded. For example, the fully-symmetric case $J_{12} \approx J_{13} \approx J_{23}$ is not a solution as can be seen in Figure 4.4. Only strongly asymmetric solutions exist for the experimental values of ΔE_1 and ΔE_2. This suggests that the added spin in the reduced charge state does not reside at the same position as in the structurally equivalent PTM triradical [6] (see position of H-atom in Figure 4.1b). Moreover, if we assume that the exchange coupling of the neutral charge state remains unchanged upon charging ($J_{12} \approx 5\,\text{meV}$), the solution set reduces to a single solution in which the added electron is asymmetrically coupled to the two radical centers ($J_{13} \approx 2\,\text{meV}$ and $J_{23} \approx 23\,\text{meV}$, see square symbol in Figure 4.4). Under this assumption the third radical spin is likely to be located on one of the two ligands attached to a radical center. To demonstrate the diversity of the solution set, two other scenarios are highlighted in Figure 4.4, including a solution with a ferromagnetic coupling ($J_{12} < 0$).

So far, the analysis only considered the differences between the excitation *energies*.

Additional information can be gained from the $\mathrm{d}I/\mathrm{d}V$ spectra of the three-spin system by analyzing the relative step height of the two spin-multiplet excitations. The step height of an excitation corresponding to a transition $|\psi_i\rangle \rightarrow |\psi_f\rangle$ is proportional to the modulus squared of its transition matrix element [13]:

$$|M_{if}|^2 = \frac{1}{2}|\langle\psi_f|\hat{\mathbf{S}}_-^{(j)}|\psi_i\rangle|^2 + \frac{1}{2}|\langle\psi_f|\hat{\mathbf{S}}_+^{(j)}|\psi_i\rangle|^2 + |\langle\psi_f|\hat{\mathbf{S}}_z^{(j)}|\psi_i\rangle|^2, \tag{4.9}$$

where $S_-^{(j)}$, $S_+^{(j)}$ and $S_z^{(j)}$ are the spin operators of spin j. In this expression, only spin-dependent second-order tunneling (COT) through spin j is taken into account, as in the simulation of Figure 4.2a. Given that the coefficients of the doublet eigenstates depend on the values of the three exchange couplings (see equations 4.3 to 4.6) we can express the matrix elements of the transitions $|D_-\rangle \rightarrow |D_+\rangle$ and $|D_-\rangle \rightarrow |Q\rangle$ in terms of J_{12}, J_{13} and J_{23}. Accordingly, we can calculate the expected relative step height for the combinations of exchange couplings that give the observed excitation energies (the solutions shown in Figure 4.4). Table 4.1 lists the relative step heights for three combinations of exchange couplings. For the estimation of the step heights from the experimental spec-

Table 4.1: Ratio of step heights $|D_-\rangle \rightarrow |D_+\rangle$ and $|D_-\rangle \rightarrow |Q\rangle$ excitations for different combinations of exchange couplings.

J_{12}	J_{13}	J_{23}	$\lvert M_{D_-\rightarrow D_+}\rvert^2/\lvert M_{D_-\rightarrow Q}\rvert^2$
5	2	23	2
-3	17	17	1.5
23	3	3	0.5

trum we focus on the COT excitation steps at negative bias voltage — estimating the step heights at positive bias voltage is hindered by the peak-shaped contributions resulting from the Kondo correlations. We estimate the ratio of the step heights of the two excitations to be ~ 2, for which the present analysis favors the first configuration in Table 4.1. Two spins are strongly coupled to each other ($\sim 23\,\mathrm{meV}$), whereas the third spin is relatively weakly coupled (2 meV to 5 meV) to the former two. This is consistent with the scenario we proposed before, in which $J_{12} \approx 5\,\mathrm{meV}$ as in the two-spin state, $J_{13} \approx 2\,\mathrm{meV}$ and $J_{23} \approx 23\,\mathrm{meV}$.

The contribution of the elastic COT background, however, which we have neglected so far, is in this configuration one order of magnitude larger than the inelastic COT steps, which is not what we observe in the experimental spectrum. In fact, if we consider transport through only one spin there is no combination of exchange couplings that reproduces the relative step height and elastic COT background at the same time. Only by introducing an interfering channel through a second spin, both the ratio of the inelastic step heights as well as the observed elastic COT contribution can match the experimental spectrum. From this analysis we would infer that transport through the three-spin system occurs through at least two interfering channels.

4.5. CONCLUDING REMARKS

In this chapter, we focused on the transport measurements of a molecular three-spin system, which was realized by electrostatically adding an electron to a diradical molecule. We deduced from IETS measurements that the added electron resided in a third singly-occupied orbital, whereby the radical character of the molecule was preserved. We discussed how the three exchange couplings of a three-spin system cannot be determined by measurements of spin excitation energies alone, and we proposed a method to extract this information based on the step height of the COT excitations. Even though the exchange-coupling analysis was made difficult by a relatively strong tunnel coupling to the electrodes in this particular device, the procedures described in Section 4.4 can be applied to other spin systems to extract information that would otherwise not be available. For example, the PTM triradical molecule studied by Gaudenzi et al. (2016) [6] would be an excellent candidate molecule for this type of analysis. Knowing the values of the exchange couplings can be used to gain insight in the structural conformation of the molecule when embedded in a single-molecule device. For example, the observation of a nearly symmetric coupling $J_{12} \approx J_{13} \approx J_{23}$ would most likely reflect a robustness in the molecule's rotational symmetry. Alternatively, one can obtain clues about the position of electrostatically added electrons, such as whether they reside on the ligands or in the core. Finally, knowing the actual spin configuration could also be essential for using coupled-spin systems as quantum logic gates [17–19].

REFERENCES

[1] R. Gaudenzi, **J. de Bruijckere**, D. Reta, I. de P. R. Moreira, C. Rovira, J. Veciana, H. S. J. van der Zant, and E. Burzurí. "Redox-Induced Gating of the Exchange Interactions in a Single Organic Diradical". *ACS Nano* 11.6 (May 2017), pp. 5879–5883. DOI: 10.1021/acsnano.7b01578.

[2] J. Veciana, C. Rovira, N. Ventosa, M. I. Crespo, and F. Palacio. "Stable polyradicals with high-spin ground states. 2. Synthesis and characterization of a complete series of polyradicals derived from 2,4,6 - trichloro - α,α,α',α',α'',α'' - hexakis(pentachlorophenyl)mesitylene with S = 1/2, 1, and 3/2 ground states". *Journal of the American Chemical Society* 115.1 (Jan. 1993), pp. 57–64. DOI: 10.1021/ja00054a008.

[3] L. Gaudreau, G. Granger, A. Kam, G. C. Aers, S. A. Studenikin, P. Zawadzki, M. Pioro-Ladrière, Z. R. Wasilewski, and A. S. Sachrajda. "Coherent control of three-spin states in a triple quantum dot". *Nature Physics* 8.1 (Nov. 2011), pp. 54–58. DOI: 10.1038/nphys2149.

[4] J.-Y. Wang, S. Huang, G.-Y. Huang, D. Pan, J. Zhao, and H. Q. Xu. "Coherent Transport in a Linear Triple Quantum Dot Made from a Pure-Phase InAs Nanowire". *Nano Letters* 17.7 (June 2017), pp. 4158–4164. DOI: 10.1021/acs.nanolett.7b00927.

[5] G. Yamahata, Y. Tsuchiya, H. Mizuta, K. Uchida, and S. Oda. "Electron transport through silicon serial triple quantum dots". *Solid-State Electronics* 53.7 (July 2009), pp. 779–785. DOI: 10.1016/j.sse.2009.03.009.

[6] R. Gaudenzi, E. Burzurí, D. Reta, I. de P. R. Moreira, S. T. Bromley, C. Rovira, J. Veciana, and H. S. J. van der Zant. "Exchange Coupling Inversion in a High-Spin Organic Triradical Molecule". *Nano Letters* 16.3 (Feb. 2016), pp. 2066–2071. DOI: 10.1021/acs.nanolett.6b00102.

[7] A. Vidan, R. M. Westervelt, M. Stopa, M. Hanson, and A. C. Gossard. "Triple quantum dot charging rectifier". *Applied Physics Letters* 85.16 (Oct. 2004), pp. 3602–3604. DOI: 10.1063/1.1807030.

[8] D. S. Saraga and D. Loss. "Spin-Entangled Currents Created by a Triple Quantum Dot". *Physical Review Letters* 90.16 (Apr. 2003). DOI: 10.1103/physrevlett.90.166803.

[9] D. P. DiVincenzo, D. Bacon, J. Kempe, G. Burkard, and K. B. Whaley. "Universal quantum computation with the exchange interaction". *Nature* 408.6810 (Nov. 2000), pp. 339–342. DOI: 10.1038/35042541.

[10] F. Meier, J. Levy, and D. Loss. "Quantum Computing with Spin Cluster Qubits". *Physical Review Letters* 90.4 (Jan. 2003). DOI: 10.1103/physrevlett.90.047901.

[11] J. M. Thijssen and H. S. J. van der Zant. “Charge transport and single-electron effects in nanoscale systems”. *physica status solidi (b)* 245.8 (Aug. 2008), pp. 1455–1470. DOI: 10.1002/pssb.200743470.

[12] D. Goldhaber-Gordon, H. Shtrikman, D. Mahalu, D. Abusch-Magder, U. Meirav, and M. A. Kastner. “Kondo effect in a single-electron transistor”. *Nature (London)* 391.6663 (Jan. 1998), pp. 156–159. DOI: 10.1038/34373.

[13] M. Ternes. “Spin excitations and correlations in scanning tunneling spectroscopy”. *New Journal of Physics* 17.6 (June 2015), p. 063016. DOI: 10.1088/1367-2630/17/6/063016.

[14] J. Paaske, A. Rosch, P. Wölfle, N. Mason, C. M. Marcus, and J. Nygård. “Non-equilibrium singlet-triplet Kondo effect in carbon nanotubes”. *Nature Physics* 2.7 (July 2006), pp. 460–464. DOI: 10.1038/nphys340.

[15] C. Simao, M. Mas-Torrent, N. Crivillers, V. Lloveras, J. M. Artés, P. Gorostiza, J. Veciana, and C. Rovira. “A robust molecular platform for non-volatile memory devices with optical and magnetic responses”. *Nature Chemistry* 3.5 (Mar. 2011), pp. 359–364. DOI: 10.1038/nchem.1013.

[16] M. Souto, V. Lloveras, S. Vela, M. Fumanal, I. Ratera, and J. Veciana. “Three Redox States of a Diradical Acceptor-Donor-Acceptor Triad: Gating the Magnetic Coupling and the Electron Delocalization”. *The Journal of Physical Chemistry Letters* 7.12 (June 2016), pp. 2234–2239. DOI: 10.1021/acs.jpclett.6b00912.

[17] J. Lehmann, A. Gaita-Ariño, E. Coronado, and D. Loss. “Spin qubits with electrically gated polyoxometalate molecules”. *Nature Nanotechnology* 2.5 (May 2007), pp. 312–317. DOI: 10.1038/nnano.2007.110.

[18] J. Lehmann, A. Gaita-Ariño, E. Coronado, and D. Loss. “Quantum computing with molecular spin systems”. *J. Mater. Chem.* 19.12 (2009), pp. 1672–1677. DOI: 10.1039/b810634g.

[19] F. Luis, A. Repollés, M. J. Martínez-Pérez, D. Aguilà, O. Roubeau, D. Zueco, P. J. Alonso, M. Evangelisti, A. Camón, J. Sesé, L. A. Barrios, and G. Aromí. “Molecular Prototypes for Spin-Based CNOT and SWAP Quantum Gates”. *Physical Review Letters* 107.11 (Sept. 2011). DOI: 10.1103/physrevlett.107.117203.

5

GROUND-STATE SPIN BLOCKADE IN A SINGLE-MOLECULE JUNCTION

It is known that the quantum mechanical ground state of a nanoscale junction has a significant impact on its electrical transport properties. This becomes particularly important in transistors consisting of a single molecule. Because of strong electron-electron interactions and the possibility of accessing ground states with high spins, these systems are eligible hosts of a current-blockade phenomenon called ground-state spin blockade. This effect arises from the inability of a charge carrier to account for the spin difference required to enter the junction, as that process would violate the spin selection rules. Here, we present a direct experimental demonstration of a ground-state spin blockade in a high-spin single-molecule transistor. The measured transport characteristics of the device exhibit a complete suppression of resonant transport due to a ground-state spin difference of 3/2 between subsequent charge states. Strikingly, the blockade can be reversibly lifted by driving the system through a magnetic ground-state transition in one charge state, using the tunability offered by both magnetic and electric fields.

Parts of this chapter have been published in Physical Review Letters [1].

After discussing molecular systems with two and three exchange-coupled spins in Chapters 3 and 4, respectively, we now turn to a single-molecule device with an even richer spin structure. As will be discussed in more detail below, the molecule of interest is a polyoxometalate or POM molecule [2], which consists of an inorganic cage with a Mn-ion at its core. We will show that the high-spin properties of this molecule allow us to observe an elusive blockade phenomenon, to which we refer to as ground-state spin blockade (GSSB).

5.1. BLOCKADES IN QUANTUM TRANSPORT

Quantum transport through nano-objects is an important research direction comprising different phenomena, some of which could potentially be used for spintronics [3–5] and quantum computing [6–8] applications. Intriguing examples of quantum transport phenomena include blockades of electric current. Various physical phenomena are involved in the underlying mechanisms of these blockades: the current in double quantum dots can be inhibited by the Pauli exclusion principle [9–11], vibrational transitions in molecular junctions and quantum dots can be suppressed by the Franck-Condon blockade [12–14], and in junctions with superconducting electrodes there may be no low-energy transport as a result of the superconducting energy gap [15, 16]. These blockade mechanisms all occur in combination with the Coulomb blockade, which results from the energy level spacing ΔE and the energy costs of charging a weakly coupled nano-object, i.e., the charging energy $U = e^2/2C$. The Coulomb blockade can be overcome as soon as the energy of an electron in one electrode exceeds the addition energy $E_{\text{add}} = \Delta E + 2U$. Then, electrons can sequentially travel from one electrode to the other via the nano-object. In every sequential electron tunneling (SET) event, the charge of the object changes by an elementary charge and the spin typically by 1/2, due to the added or removed electron.

Here, we study an exceptionally clear manifestation of the blockade phenomenon that occurs when the ground-state spin of subsequent charge states differs by more than 1/2. SET transitions between these ground states are forbidden by the spin selection rules and Coulomb blockade peaks are suppressed [17–19]. We refer to this effect as a ground-state spin blockade (GSSB). One of the necessary requirements for a GSSB is a high-spin ground state, i.e., $S > 1$, in one of the charge states. This requirement is hard to obtain for top-down quantum dots and in the few earlier demonstrations of a GSSB, neither the full suppression of the Coulomb blockade peaks nor control over the blockade was achieved [20, 21]. For molecules, high-spin ground states can be tailored by chemical design, making them promising candidates for observing a GSSB. In this transport study, we provide experimental evidence for a complete GSSB in a high-spin single-molecule junction. With an external magnetic field, the blockade can be reversibly lifted by driving the molecule in one charge state through a magnetic ground-state transition. The presence of a GSSB puts constraints on the allowed transitions and is used as a diagnostic tool to determine the ground state, and excited states of the molecule.

5.2. MEASUREMENT DESCRIPTION

The measurements were carried out with the device sketched in Figure 5.1a. A single molecule is embedded in a circuit with two gold electrodes in which DC current (I) is measured as a function of the applied voltage difference between the electrodes (the bias voltage V) and the voltage applied to a capacitively coupled gate electrode (V_g). The junction is formed by room-temperature electromigration [22] and self-breaking [23] of a gold nanowire. A dilute solution of the molecules is drop casted on a chip with 24 electromigrated junctions on which, after pumping away the solution and cooling down the sample ($T \approx 40\,\text{mK}$), three junctions show a Coulomb blockade with addition energies in the typical regime of molecular junctions, i.e., $E_{\text{add}} > 100\,\text{meV}$. The tunnel couplings and energy level alignments cannot be controlled by this technique and depend on the way the molecule is trapped inside the junction. One of the three samples shows the right combination of a small tunnel coupling, which allows for high-resolution spectroscopy, and a level alignment close to the Fermi level of the electrodes, such that the molecule can be charged within the accessible gate-voltage range. The molecule in the junction is a pyridine-functionalized Mn(III) Anderson polyoxometalate (POM) [2], which is sketched in Figure 5.1a. Its properties and synthesis are discussed in Section 5.8.

5.3. SUPPRESSION OF LINEAR CONDUCTANCE

In Figure 5.1b, the two top panels show differential conductance ($\mathrm{d}I/\mathrm{d}V$) maps of the device as a function of V and V_g, at zero magnetic field and at 8 T. For clarity, we first discuss the map at 8 T, which looks like a common $\mathrm{d}I/\mathrm{d}V$ map of a Coulomb-blockaded system containing a single object, here, a molecule. The regions labeled N and $N-1$ are regions in which the charge of the molecule is fixed and SET processes are suppressed. Inside these regions, transport is governed by cotunneling (COT) processes, which appear as horizontal lines. The two slanted lines forming the cross-like shape are the edges of the Coulomb diamonds and their point of incidence at zero bias is the charge degeneracy point. The bottom right panel shows that this point appears as a peak in the linear-conductance gate trace, i.e., the $\mathrm{d}I/\mathrm{d}V|_{V=0}$ as a function of V_g. In the top and bottom regions of the $\mathrm{d}I/\mathrm{d}V$ map, the charge of the molecule can fluctuate, allowing for SET processes to occur. The top SET region contains slanted lines starting from the left Coulomb edge at $V = 0.9\,\text{mV}$ and, less intense, at $V = 0.3\,\text{mV}$, both moving towards the top right. These lines correspond to SET processes involving excited states.

Remarkably, in the map at 0 T, the charge degeneracy point is absent: slanted lines are present, but they do not cross at zero bias. At any gate voltage, the linear conductance is suppressed and only SET lines at finite voltages are present. This shows that transitions between the ground state of N and the ground state of $N-1$ are blocked. The complete suppression can be seen more clearly in the zero-bias trace presented in the corresponding bottom panel, which in contrast to the 8 T trace shows no peak. All the slanted lines in the map appear at finite bias voltages and mark transitions involving at least one excited state: the SET line starting at $V = 0.7\,\text{mV}$ coincides with a COT line at that same bias voltage, which implies that their excitation energies are equal, and involve the same excited state. Similarly, the COT lines at $V = \pm 0.1\,\text{mV}$ in N connect to two SET lines starting at the same bias voltages. Another faint COT line appears at $V = -0.4\,\text{mV}$ in $N-1$,

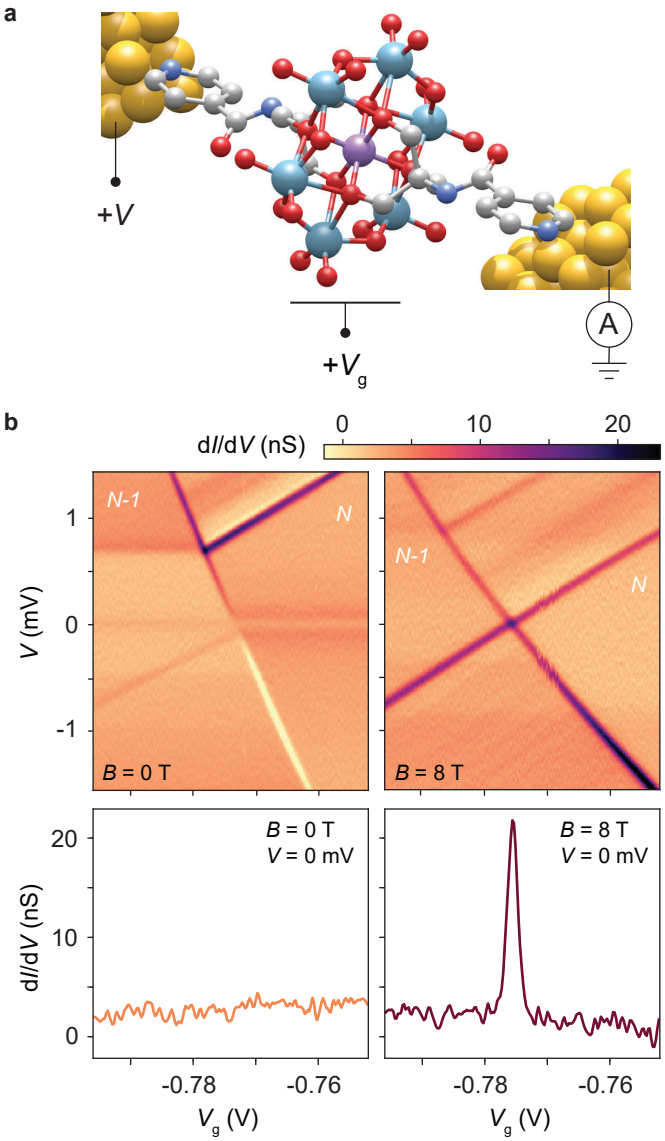

Figure 5.1: a. Sketch of the molecule, gold electrodes and measurement circuit. The molecule consists of a Mn(III) center (purple) surrounded by six MoO_6 octahedra, which connect on both sides to pyridine-based ligands. Electric current (I) through the molecule is recorded as a function of bias voltage (V) and gate voltage (V_g). **b**. (Top) dI/dV maps at zero magnetic field (left) and at 8 T (right). At 0 T, no SET lines corresponding to transitions between the ground states of N and $N-1$ are present, as a result of ground-state spin blockade. At 8 T, these lines do appear and the blockade is lifted. (Bottom) dI/dV traces at zero bias, showing a charge degeneracy peak at 8 T and its complete suppression at 0 T.

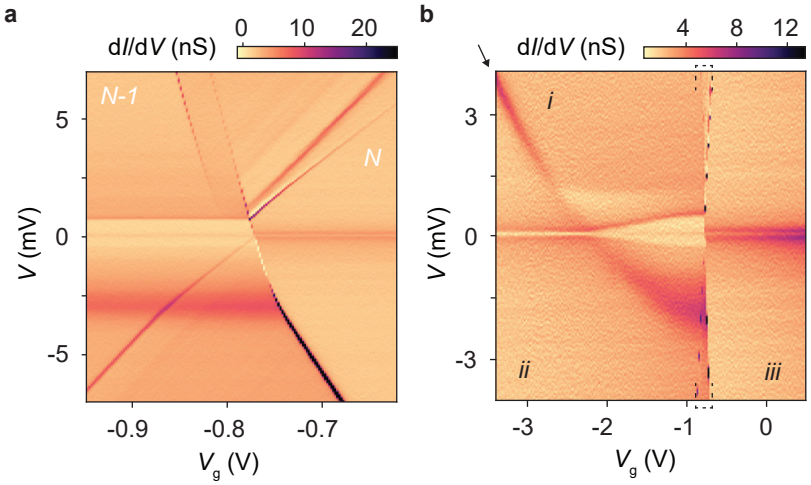

Figure 5.2: dI/dV maps at 0 T in a wide bias- and gate-voltage range. **a**. dI/dV map showing the same features as in Figure 5.1b, along with a ground-state transition line at $V = -3$ mV and additional SET excitation lines with different slopes. The SET lines at negative bias change slope at the ground-state transition. **b**. dI/dV map in a larger gate window, where the region marked by dashed brackets is the region shown in **a**. The dark parabolic feature indicated by the arrow is the ground-state transition line in **a**. Three different regions with different ground states are separated by the discontinuity and the parabola, labeled *i, ii* and *iii*. The excitation energy of the COT excitations in *i* are tunable by the gate voltage.

closer to zero bias than its counterpart at positive bias. This asymmetry suggests that the corresponding excitation energy is influenced by the bias voltage. The region $N-1$ also contains a zero-bias line, which resembles a Kondo resonance [24].

5.4. SPIN GROUND-STATE TRANSITION

The striking difference between the maps at 0 and 8 T in Figure 5.1b is the presence of the charge degeneracy point; the complete suppression of this point at 0 T is lifted at 8 T. To study the blockade mechanism in more detail, we show two dI/dV maps in a larger gate and bias-voltage range in Figure 5.2, both recorded at 0 T. In Figure 5.2a, the same features as in Figure 5.1b can be observed, along with a broad horizontal line at $V = -3$ mV and additional SET excitation lines at higher bias. The Coulomb edges at negative bias change slope at the two coincidences with the broad horizontal line. This feature shows striking similarities with the simulated transport data presented in reference [25], where a singlet-triplet ground-state transition line in a double-quantum-dot model is studied. The energies of the ground states separated by this line have a different dependence on bias voltage, causing their corresponding Coulomb edges to have different slopes.

The gate- and bias-voltage dependence of the ground-state transition line is shown

in Figure 5.2b where the transport data are presented for an even wider gate-voltage range. The dashed brackets in this figure mark the gate-voltage range of Figure 5.2a. Figure 5.2b reveals that the ground-state transition line, indicated by the arrow, extends towards positive bias voltages and has an anomalous parabolic shape (see Section 5.9.2 for a more detailed analysis). Three regions with different ground states can be distinguished, separated by the parabola and the Coulomb edges. We label the regions *i*, *ii* and *iii*, where *i* and *ii* belong to the charge state $N-1$, and *iii* to the charge state N. In both *ii* and *iii*, a pair of COT lines appears at $V = \pm 0.1\,\mathrm{mV}$, symmetrically positioned around zero bias. In *i*, a pair of gate-voltage dependent COT lines is present, starting at $V = \pm 0.1\,\mathrm{mV}$ around $V_g = -2\,\mathrm{V}$, moving away from zero bias as V_g is increased. The excitation energy of this COT line thus depends on the gate voltage.

5.5. MAGNETIC-FIELD DEPENDENCE

Next, we investigate the magnetic-field dependence of the parabolic ground-state transition line. Figure 5.3a shows four maps in the same bias- and gate-voltage range as in Figure 5.2b, at different magnetic fields. By increasing the magnetic field, the parabola moves towards higher bias voltages, and the $\mathrm{d}I/\mathrm{d}V$ along the line changes in magnitude and sign. For an increasing part of the line, the $\mathrm{d}I/\mathrm{d}V$ turns negative; i.e., the current goes down by increasing the bias voltage at the transition from *ii* to *i*.

The fact that the ground-state transition line moves upwards with magnetic field implies that the total spin of the ground state in region *ii* is larger than in region *i*; upon increasing the magnetic field, the ground state with higher spin becomes energetically more favorable and the transition occurs at higher bias voltages. Above 4 T, region *ii* moves across zero bias at the charge degeneracy point, which lifts the GSSB at this point. The parabola thus marks the transition from a spin-blockaded region (*i*), to a region where the blockade is lifted (*ii*).

To identify the spin states in $N-1$ we focus on the magnetic-field dependence of the $\mathrm{d}I/\mathrm{d}V$ spectrum in $N-1$ (see Section 5.10.1 for a discussion on the spectrum of charge state N, which includes references [26–29]), recorded at a fixed gate voltage $V_g = -1\,\mathrm{V}$ (see Figure 5.3b). The Kondo-like peak at zero bias splits linearly in two in a magnetic field, which verifies the presence of a degenerate ground state at 0 T. The COT excitations at $V = 0.7\,\mathrm{mV}$ and $V = 0.4\,\mathrm{mV}$ split in three and appear asymmetric in position and intensity. The fact that these excitations split in three implies that the corresponding excited state is a spin multiplet with a larger spin than the ground state; this can be deduced from the spin selection rules for COT processes [19]. Moreover, the spin selection rules impose additional constraints which lead to the conclusion that the spin difference between the excited state and the ground state is 1.

At about 5 T, one excitation from the excited spin multiplet crosses zero bias, which at that point becomes the new spin ground state. The two regions with different ground states are separated by the slanted line indicated by the arrow. These regions correspond to *i* and *ii* in Figure 5.2b, labeled accordingly in Figure 5.3b. The finite slope of the ground-state transition line results from the influence of the bias voltage on the associated excitation energy. This is also reflected by the asymmetry in bias voltage at which the multiplet excitations appear.

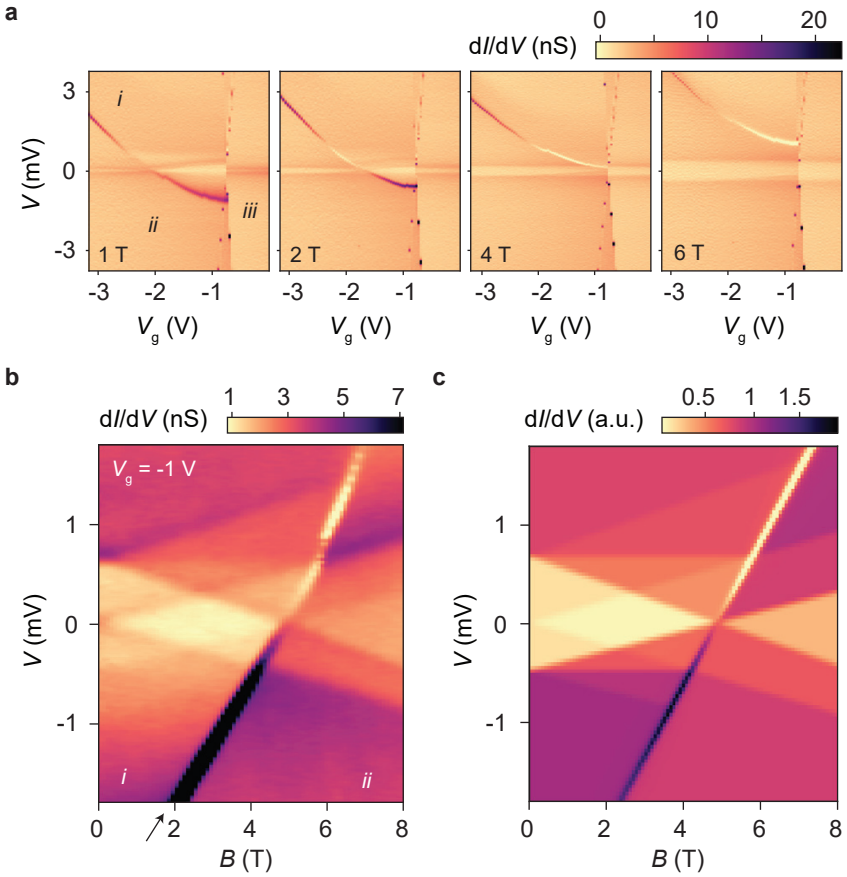

Figure 5.3: a. dI/dV maps of the same region as Figure 5.2b, at different magnetic fields. The parabolic line separating the two spin ground states in $N-1$ moves upwards by increasing the magnetic field as the high-spin state becomes energetically more favorable. **b**. Magnetic-field dependence of the dI/dV spectrum at $V_g = -1$ V. One line originating from the excited multiplet crosses zero bias at $B = 5$ T and becomes the new ground state above this field. The two ground states are separated by the slanted line indicated by the arrow. **c**, Simulated dI/dV spectra for a system of a spin-1/2, tunnel coupled to two reservoirs and exchange coupled to a spin-3/2, with a V-dependent exchange coupling.

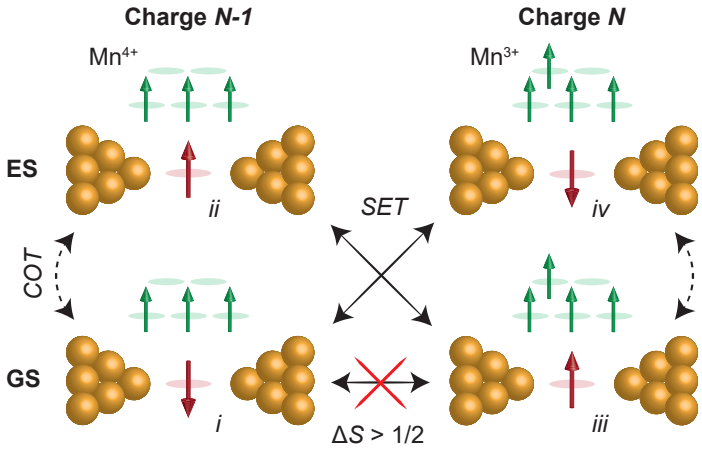

Figure 5.4: Diagram showing the four states of different charge and spin, where the red and green arrows correspond to the ligand spin and the spins in the Mn center, respectively. The observed SET and COT transitions are represented by solid and dashed arrows, respectively. The red cross indicates the blocked SET transition. For charge state $N-1$, $S=1$ (*i*) and $S=2$ (*ii*), and for charge state N, $S=5/2$ (*iii*) and $S=3/2$ (*iv*, only appears as an excited state).

5.6. MOLECULAR SPIN STRUCTURE

A model explaining the main features of the experimental data can now be constructed. The observed spin excitations occur at relatively low bias voltages (~ 1 mV), which suggests that they are not related to spin reconfigurations of the Mn center itself, as for spin-crossover molecules [30, 31]; the energies of these transitions are typically orders of magnitude larger. Rather, we propose a model in which we invoke a weakly-coupled spin, exchange coupled to the high-spin center. This spin is possibly residing on the ligands of the molecule, as in other molecular systems [7, 32] and we will refer to it as the ligand spin. We present a simulation of this system's spin-excitation spectra, based on reference [33] in Figure 5.3c (see Section 5.9.1 for a description of the simulation).

The ground state (GS) and excited state (ES) in the simulation of $N-1$ (N) are sketched on the left-hand (right-hand) side in Figure 5.4, where red arrows represent the ligand spins, green arrows represent the spins of the Mn center and yellow spheres represent the gold atoms of the electrodes. The observed SET and COT transitions between the states are indicated by the solid and dashed black arrows, respectively. In the transition from charge state $N-1$ to N, the added electron is likely to reside on the metal center, changing the oxidation state from Mn^{4+} to Mn^{3+}, as illustrated in Figure 5.4. This charge transition of the Mn center occurs in solutions of this compound as shown by cyclic voltammetry measurements [2]. The spin of the Mn center in N would then match the spin measured in crystals of this type of compound [34], namely $S=2$.

For GSSB to occur in this system, the ground-state spin should change by more than $1/2$ upon charging. This can happen if the added charge not only contributes with its intrinsic spin, but its presence also changes the sign of the exchange coupling from anti-

ferromagnetic to ferromagnetic, further increasing the total spin by 1. Such a transition of the exchange coupling is observed, and it is marked by the parabolic ground-state transition line in $N-1$. We performed a model calculation to show that for this molecular system there exists a realistic scenario under which a sign change of the exchange coupling occurs (see Section 5.9.3).

The total spin of states *i* and *iii*, as shown in Figure 5.4, are 1 and 5/2, respectively, which amounts to a spin difference of 3/2. SET transitions between these ground states are thus rendered forbidden, as indicated by the red cross in Figure 5.4. At high magnetic fields, the high-spin state *ii* ($S = 2$) becomes the ground state for $N-1$, lowering the ground-state spin difference to 1/2, whereby the GSSB is lifted.

5.7. CONCLUDING REMARKS

In summary, we have demonstrated GSSB in a high-spin single-molecule junction, which can be reversibly lifted by driving the system through a magnetic ground-state transition with an external magnetic field. The blockade results from a sign change of the exchange coupling upon charging, which causes the ground-state spin of subsequent charge states to differ by more than 1/2.

This work shows that the act of charging a nanoscale object is not merely a consecutive filling of the lowest unoccupied orbitals, whereby the spin changes by $\pm 1/2$. Rather, the charging can have a strong influence on the internal exchange couplings of the object, to a degree that ground-state transitions cannot be realized by single charge carriers. The presence of GSSB is not restricted to single-molecule systems: every nano-object with a spin $S > 1$ can potentially host this effect under the right conditions. A thorough understanding of GSSB is therefore of essence in research directions where high-spin devices are increasingly gaining interest, such as spintronics [3–5] and quantum computing [6–8].

5.8. APPENDIX A — EXPERIMENTAL DETAILS

The pyridine-functionalized Mn(III) Anderson POM was prepared by modifying a previously described procedure [2]: $[N(C_4H_9)_4]_4[\alpha-Mo_8O_{26}]$ (0.5 g, 0.232 mmol), $Mn(OAc)_3$ (0.089 g, 0.350 mmol) and $(HOCH_2)_3CNHCO(4-C_5H_4N)$ (0.185 g, 0.818 mmol) were refluxed overnight under an argon atmosphere in 18 mL acetonitrile. The resulting solution was cooled to room temperature. Diethyl ether was added to obtain a precipitate, which was isolated by centrifugation and recrystallized in dimethylformamide.

The molecule consists of a molecular metal oxide formed by a central Mn(III)-ion, surrounded by six edge-sharing octahedra, which confer robustness to the POM and magnetic isolation. This type of molecule is axially functionalized on both sides by organic molecules linked directly to the Mn(III)-ion through alcoxo bridges. Magnetic characterization of these compounds in the solid state shows that the Mn(III) has a total spin $S = 2$ and a g-factor close to 2.

The transport device was created by depositing a bow-tie-shaped Au nanowire with a thickness of 12 nm, suitable for electromigration and self-breaking, on a pre-patterned gate electrode consisting of a 60 nm-thick Pd strip, covered with 5 nm of ALD-grown Al_2O_3. The nanowire was contacted to Au contact pads by 85 nm-thick Au connection lines. All Au and Pd structures were defined by standard e-beam lithography and e-beam evaporation techniques.

All transport measurements are performed in a dilution refrigerator with a base temperature of $T \approx 40$ mK. The dI/dV maps in Figures 5.1 to 5.3 are all recorded in DC, except for the magnetic-field dependence in Figure 5.3b, which is recorded using a lock-in amplifier to achieve a higher signal-to-noise ratio. The magnetic field is applied with a vector magnet oriented out-of-plane with respect to the sample's substrate, except for the measurements shown in Figure 5.7c and (d).

5.9. APPENDIX B — MODEL CALCULATIONS

5.9.1. SIMULATION OF THE SPIN-EXCITATION SPECTRA IN N-1

The spin-excitation spectra in Figure 5.3c are simulated by a tunneling model based on [33]. The model includes COT processes of second order and solves the rate equations for a spin system consisting of a ligand spin $S = 1/2$, tunnel coupled to two reservoirs and exchange coupled to a high-spin ($S = 3/2$) center. The exchange coupling in $N-1$ is antiferromagnetic, which at low magnetic fields results in a low-spin ground state ($S = 1$) and a high-spin excited state ($S = 2$). We add a linear V term (0.1 eV/V) in the expression of the exchange coupling as in [25], which accounts for the asymmetric positions of the COT excitations and the appearance of the slanted ground-state transition line.

5.9.2. TUNABILITY OF THE PARABOLIC GROUND-STATE TRANSITION LINE

Here, we focus on the influence of the gate voltage and bias voltage on the exchange coupling between the high-spin Mn center and the ligand spin in charge state $N-1$. We find that the exchange coupling is approximately given by the phenomenological expression

$$J = \alpha + \beta eV + \gamma e(V_g - \delta)^2, \tag{5.1}$$

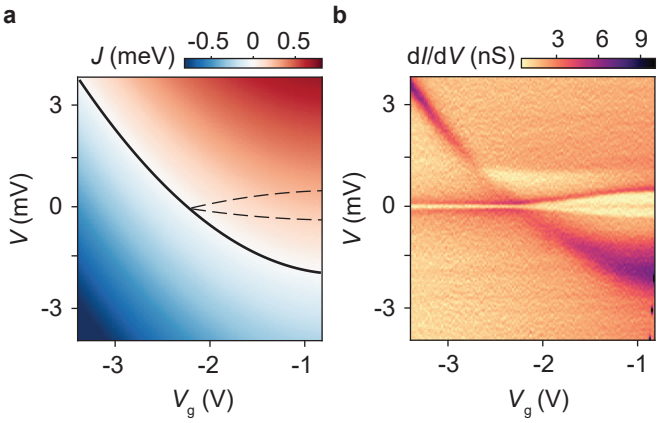

Figure 5.5: a. Value of J according to Equation (5.1). The solid line indicates where $J = 0$, which corresponds to a ground-state transition. The dashed lines indicate where $V = \pm 2J$, which is the condition for the low-energy COT excitations in this system. Parameters used: $\alpha = 0.2\,\text{meV}$, $\beta = 0.1$, $\gamma = -0.1\,\text{mV/V}$, $\delta = 0.6\,\text{V}$. **b**. Experimental data in the same gate and bias voltage range as in **a**.

5

in which $\alpha = 0.2\,\text{meV}$, $\beta = 0.1$, $\gamma = -0.1\,\text{mV/V}$, $\delta = 0.6\,\text{V}$ and e is the elementary charge. This quantity is plotted as a function of V and V_g in Figure 5.5a, in the range of the experimental data shown in Figure 5.5b. This region corresponds to the $N-1$ region of Figure 5.2b. The solid line in Figure 5.5a indicates where $J = 0$, i.e., where the ground-state transition from i to ii takes place, as seen in the experimental data. The same expression for the exchange coupling is used to simulate the $\text{d}I/\text{d}V$ spectra in Figure 5.3c. The dashed lines in Figure 5.5a indicate where the COT excitations from i to ii are expected, according to the condition $eV = \pm 2J$. The same gate and bias voltage dependence of these excitations is present in the experimental data shown in Figure 5.5b. The microscopic parameters involved in the exchange coupling are analyzed in the model calculation in Section 5.9.3.

5.9.3. MODEL CALCULATION OF GROUND-STATE SPIN BLOCKADE

Here, we show by a model calculation how GSSB arises in the scenario discussed in the main text. The model contains electron-electron repulsion, a Hund's rule coupling in the Mn center and a superexchange coupling between the ligand spin and the Mn center. We work out the energies for the different spin and charge states illustrated in Figure 5.4 of the main text and we discuss the conditions under which GSSB occurs.

The energy associated with the Hund's rule coupling in the Mn center is given by:

$$E_\text{H}(n) = -K\frac{n(n-1)}{2}, \tag{5.2}$$

where K is the Hund's rule coupling parameter and n is the number of electrons with the same spin. Further, we consider electron-electron repulsion on the atom, which

we parameterize in terms of U. The energy associated with this interaction scales with electron number in the following way:

$$E_U(m) = U\frac{m(m-1)}{2}, \tag{5.3}$$

where m is the total number of electrons in the relevant atomic shell. The one-electron energies are parameterized in terms of two gaps, Δ and Δ_L, where Δ is the ligand-field splitting in the d shell of the Mn center, and Δ_L is the energy splitting between the ligand orbital and the lower d orbitals. We set the energy of the lower d orbitals to zero and assume that the ground-state configurations of the two charge states correspond to the diagrams shown in Figure 5.6a. The energies of the ground states are given by:

$$E_3 = \Delta_L + 3U - 3K, \quad E_4 = \Delta + \Delta_L + 6U - 6K. \tag{5.4}$$

Both configurations are twice degenerate, since the spin on the ligand can be either up or down. The purpose of this section is to find out what mechanism breaks the degeneracy and which state has the lowest energy.

So far, we have not considered the coupling between the ligand orbital and the d orbitals of the Mn center. We incorporate this coupling by a simple hopping term parameterized in terms of a hopping parameter t, which we assume to be the same for all d orbitals. This assumption is not essential. In operator terms the Hamiltonian of the coupling reads:

$$H_{\mathrm{T}} = -t\sum_{i\sigma}(d_\sigma^\dagger c_{i\sigma} + c_{i\sigma}^\dagger d_\sigma), \tag{5.5}$$

where $d_\sigma^\dagger$ (d_σ) is the creation (annihilation) operator for an electron in the ligand orbital with spin σ and $c_{i\sigma}^\dagger$ ($c_{i\sigma}$) is the creation (annihilation) operator for an electron in orbital i of the Mn center with spin σ.

Superexchange is the result of a second order perturbation theory in the hopping t. The superexchange Hamiltonian is given by:

$$H_{\mathrm{SE}} = -H_{\mathrm{T}}\frac{1}{H_0 - E_0}H_{\mathrm{T}}, \tag{5.6}$$

where E_0 is the unperturbed ground state energy and H_0 is the unperturbed Hamiltonian, i.e., the energy of the system without the ligand-Mn coupling.

When applied to the ground state(s), H_{T} can create various intermediate states. We list these states below together with their energies. The model parameters are required to have values such that all these states are in fact excited states, i.e., have energies higher than their corresponding ground states.

Figure 5.6b and (c) show the intermediate states of the $n = 3$ and $n = 4$ sector, respectively. Their excitation energies, $\Delta E = H_0 - E_0$, are given by

$$\Delta E_a = \Delta - \Delta_L + 3U - 3K, \quad \Delta E_b = \Delta - \Delta_L + 3U, \tag{5.7}$$

$$\Delta E_c = -\Delta_L + 3U, \quad \Delta E_d = \Delta_L + U_L - 2U + 2K \tag{5.8}$$

$$\Delta E_e = \Delta - \Delta_L + 4U - 4K, \quad \Delta E_f = \Delta - \Delta_L + 4U \tag{5.9}$$

$$\Delta E_g = \Delta - \Delta_L + 4U, \quad \Delta E_h = -\Delta_L + 4U \tag{5.10}$$

$$\Delta E_i = \Delta_L - \Delta + U_L - 3U + 3K, \quad \Delta E_j = \Delta_L + U_L - 3U + 3K. \tag{5.11}$$

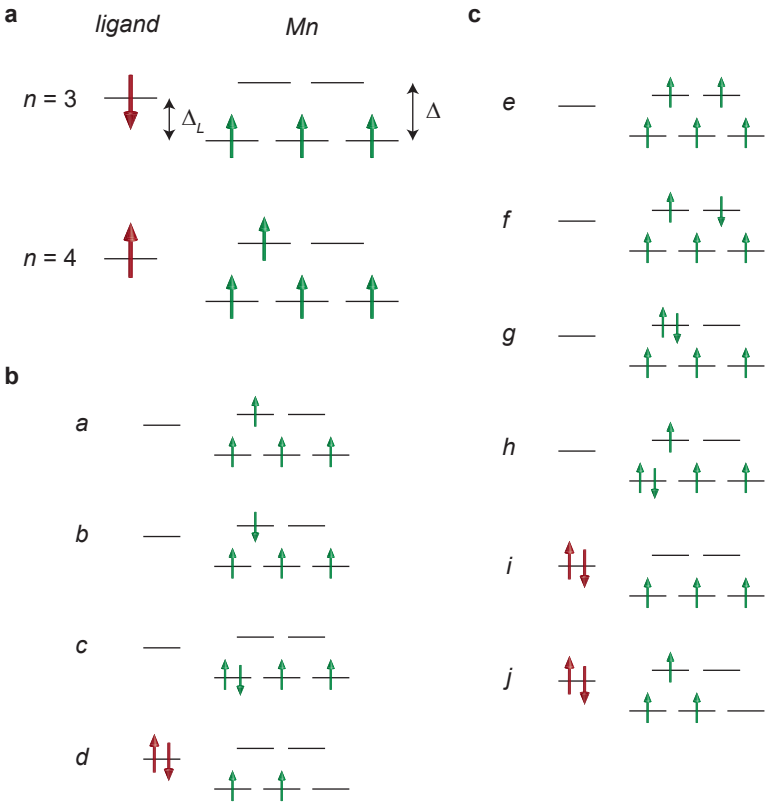

Figure 5.6: a. Ground-state configurations for $n = 3$ and $n = 4$. The ligand-field splitting Δ and the orbital energy difference between the ligand spin and the lower d orbitals, Δ_L, are indicated. **b**. Intermediate states in the $n = 3$ and (c) $n = 4$ sector.

Superexchange lifts the degeneracy between the spin up and spin down ligand states. Using the above expressions we obtain the following expressions for the energy differences $\Delta E_3 = E_{3\uparrow} - E_{3\downarrow}$ and $\Delta E_4 = E_{4\uparrow} - E_{4\downarrow}$. They are

$$\Delta E_3 = t^2\left(\frac{2}{E_b} + \frac{3}{E_c} + \frac{3}{E_d} - \frac{2}{E_a}\right) \tag{5.12}$$

and

$$\Delta E_4 = t^2\left(\frac{1}{E_f} + \frac{1}{E_g} + \frac{3}{E_h} + \frac{1}{E_i} + \frac{3}{E_j} - \frac{1}{E_e}\right). \tag{5.13}$$

For GSSB to occur in this model, it is required that the ligand spin anti-aligns with the Mn spin for the $n = 3$ case and aligns for the $n = 4$ case. This corresponds to a situation where $\Delta E_3 > 0$ and $\Delta E_4 < 0$. Upon inspection of the expressions, we see that this requirement is satisfied if the energy ΔE_e is close to zero. In case $\Delta E_e = 0$, the state with an empty ligand orbital and 5 parallel spins in the Mn center is degenerate with the $n = 4$ ground state.

In terms of parameters the situation $\Delta E_e = 0$ corresponds to

$$U + \frac{\Delta - \Delta_L}{4} = K. \tag{5.14}$$

The parameter U describes direct electron-electron repulsion. Such a quantity can be screened and is thus sensitive to changes in the environment, as is Δ_L. These are the quantities which are most likely tunable by the gate and bias voltage. This is in contrast to e.g. the Hund's rule coupling K, which is relatively insensitive to changes in the electrostatic environment.

It is important to check, that all other excitation energies are in fact positive and not close to zero. If we impose the condition (Equation (5.14)) we get the following energies:

$$\Delta E_a = \frac{\Delta - \Delta_L}{4}, \quad \Delta E_b = \frac{\Delta - \Delta_L}{4} + 3K, \tag{5.15}$$

$$\Delta E_c = -\frac{3}{4}\Delta - \frac{1}{4}\Delta_L + 3K, \quad \Delta E_d = \frac{1}{2}\Delta_L + \frac{1}{2}\Delta + U_L \tag{5.16}$$

$$\Delta E_e = 0, \quad \Delta E_f = 4K \tag{5.17}$$

$$\Delta E_g = 4K, \quad \Delta E_h = -\Delta + 4K \tag{5.18}$$

$$\Delta E_i = \frac{1}{4}\Delta_L - \frac{1}{4}\Delta + U_L, \quad \Delta E_j = \frac{1}{4}\Delta_L + \frac{3}{4}\Delta + U_L. \tag{5.19}$$

Given that K is the largest parameter, we only need to check the a and the d terms in the $n = 3$ sector. First, ΔE_a and ΔE_d have to be positive, and also ΔE_3 should be positive. The latter requires

$$3E_a > 2E_d \Rightarrow \Delta_L < -\frac{1}{7}\Delta - \frac{8}{7}U_L, \tag{5.20}$$

in which case we can write

$$\Delta E_d < \frac{3}{14}\Delta + \frac{3}{7}U_L, \tag{5.21}$$

which is consistent with ΔE_d being positive. Finally, we should check that the energies in the $n = 4$ sectors are positive. The most critical quantities are ΔE_i and ΔE_j. Given the

requirement (Equation (5.20)) we get

$$\Delta E_i < \frac{5}{7}U_L - \frac{2}{7}\Delta, \quad \Delta E_j < \frac{5}{7}(\Delta + U_L). \tag{5.22}$$

Neither of these bounds are negative if $U_L > 2\Delta/5$, which is a mild requirement.

The sign change of the exchange coupling can be understood from a more intuitive point of view in the following way: In N, the partial delocalization of the ligand spin over the e_g orbitals of the Mn^{3+} results in a ferromagnetic exchange coupling by the Hund's rule coupling. In $N-1$, the ligand spin rather delocalizes over the occupied t_{2g} orbitals of the Mn^{4+}, which yields an anti-ferromagnetic coupling. The electrostatic field created by the gate and bias voltage can influence the spatial distribution of the ligand spin, which results in the observed tunability of the spin ground states.

In conclusion, there exists a realistic scenario, where $\Delta E_4 < 0$ and $\Delta E_3 > 0$, i.e., where there is an anti-ferromagnetic coupling between the ligand and the Mn center in the $n = 3$ sector and a ferromagnetic coupling in the $n = 4$ sector, such that GSSB occurs.

5.10. APPENDIX C — ADDITIONAL DATA

5.10.1. MAGNETIC-FIELD DEPENDENCE OF THE dI/dV SPECTRUM IN N

Figure 5.7 shows four panels with the magnetic-field dependence of the dI/dV spectrum in charge state N ($V_g = -0.5$ V). The data in Figure 5.7a is recorded in a large magnetic field range, with the magnetic field directed out-of-plane (z-axis). One excitation splitting linearly with magnetic field can be identified. At low magnetic field, around 0.4 T, the excitation appears as a peak centered at zero bias. This peak is presumably due to a Kondo resonance that results from the spin degeneracy of the ground state. The expected COT excitations at finite magnetic field of this spin system correspond to transitions from the $m = -5/2$ state of *iii* ($S = 5/2$) to the $m = -3/2$ state of both *iii* ($S = 5/2$) and *iv* ($S = 3/2$). Other transitions are forbidden due to the spin selection rules. Resolving the two excitations separately in the data is hindered by the pronounced Kondo peak and presumably the small difference in excitation energy.

A detailed map of the low-magnetic field range is shown in Figure 5.7b, in which a zero-bias dip can be observed below 0.4 T. The transition in magnetic field from a dip at 0 T to a peak at 0.4 T that splits again at higher fields, is independent of the direction in which the magnetic field is oriented, as can be seen in Figure 5.7c and Figure 5.7d. These maps are recorded with the magnetic field oriented in-plane, in two perpendicular directions. The peak-dip structure can be clearly observed in Figure 5.7e where the dI/dV spectrum at $B = 0$ is presented. Figure 5.7f shows the linear conductance as a function of magnetic field, which is non-monotonic in the low magnetic field range.

The independence of the magnetic field direction excludes the possibility of the dip being the result of a zero-field splitting by magnetic anisotropy, as for single-molecule magnets [26]. Similarly, a splitting due to Dzyaloshinskii-Moriya interaction depends strongly on the orientation of the magnetic field [27] and can be excluded.

Instead, the data shows striking similarities with a two-stage Kondo effect [28]. This phenomenon can exclusively be observed in systems with $S > 1/2$, and involves two different Kondo energy scales: $k_B T_{K1}$ and $k_B T_{K2}$ ($T_{K2} < T_{K1}$). The former is associated with

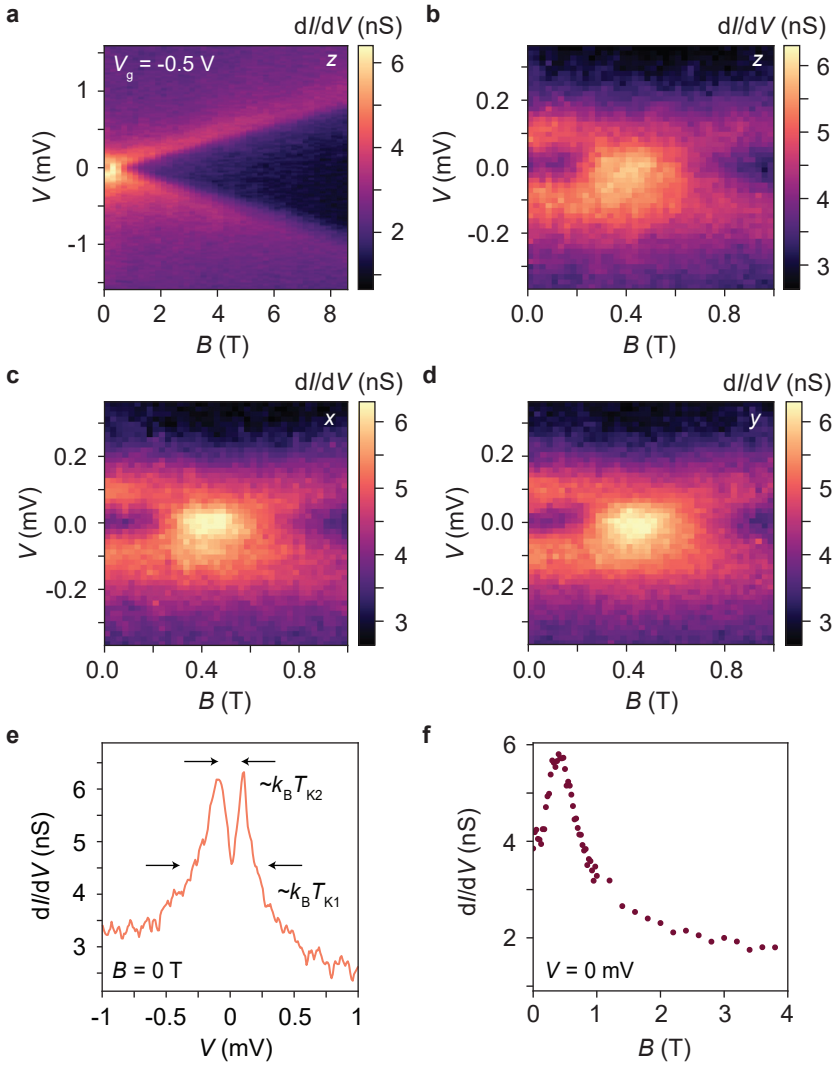

Figure 5.7: Magnetic-field dependence of the $\mathrm{d}I/\mathrm{d}V$ spectrum in N. All maps recorded at $V_\mathrm{g} = -0.5\,\mathrm{V}$. **a** Magnetic field applied in the z-direction, i.e., perpendicular to the current, out of the substrate's plane. **b**. Same B-field direction as in **a**, but in a smaller B and V range. **c** Same as **b**, with field applied along x, i.e., perpendicular to the current, in the substrate's plane. **d** Same as **b**, with field applied along y, i.e., parallel to the current. **e** and **f** show the $\mathrm{d}I/\mathrm{d}V$ spectrum at zero magnetic field and the linear conductance in magnetic field, respectively.

the first screening stage, whereby the spin is reduced by 1/2, yielding a peak of width $\sim k_B T_{K1}$; similar to the standard Kondo effect. The second stage reduces the spin by an additional amount of 1/2, which yields a zero-bias dip of width $k_B T_{K2}$. The dip results from the fact that the second screening stage quenches the first screening stage below $eV \sim k_B T_{K2}$ [29]. The spectrum in Figure 5.7e contains both these features. The two Kondo energy scales are tentatively indicated by the arrows. As the magnetic field is increased, the second stage of Kondo screening stage will be suppressed, recovering the zero-bias peak of width $\sim k_B T_{K1}$: Here, at 0.4 T. At even higher fields, the Kondo peak associated with T_{K1} splits in two, in a similar way as a standard spin-1/2 Kondo. The presence of a two-stage Kondo effect is also reflected by the non-monotonic evolution of the linear conductance in magnetic field [28, 29], as shown in Figure 5.7f for this device.

5.10.2. MAGNETIC-FIELD EVOLUTION OF STABILITY DIAGRAMS

A more detailed evolution of the lifting of the GSSB by the ground-state transition line is shown in Figure 5.8. The dI/dV maps in this figure are all recorded in the same gate and bias voltage range, around the charge transition from $N-1$ to N, at different magnetic fields, as indicated in the panels. As the ground-state transition line crosses zero bias, between 5 T and 6 T, the charge degeneracy point is recovered, which indicates that the GSSB is lifted. Figure 5.8 also shows that the ground-state transition line becomes narrower at higher magnetic field, i.e, when the spin multiplets are split. It is not yet understood how the magnetic field reduces the linewidth of the ground-state transition line.

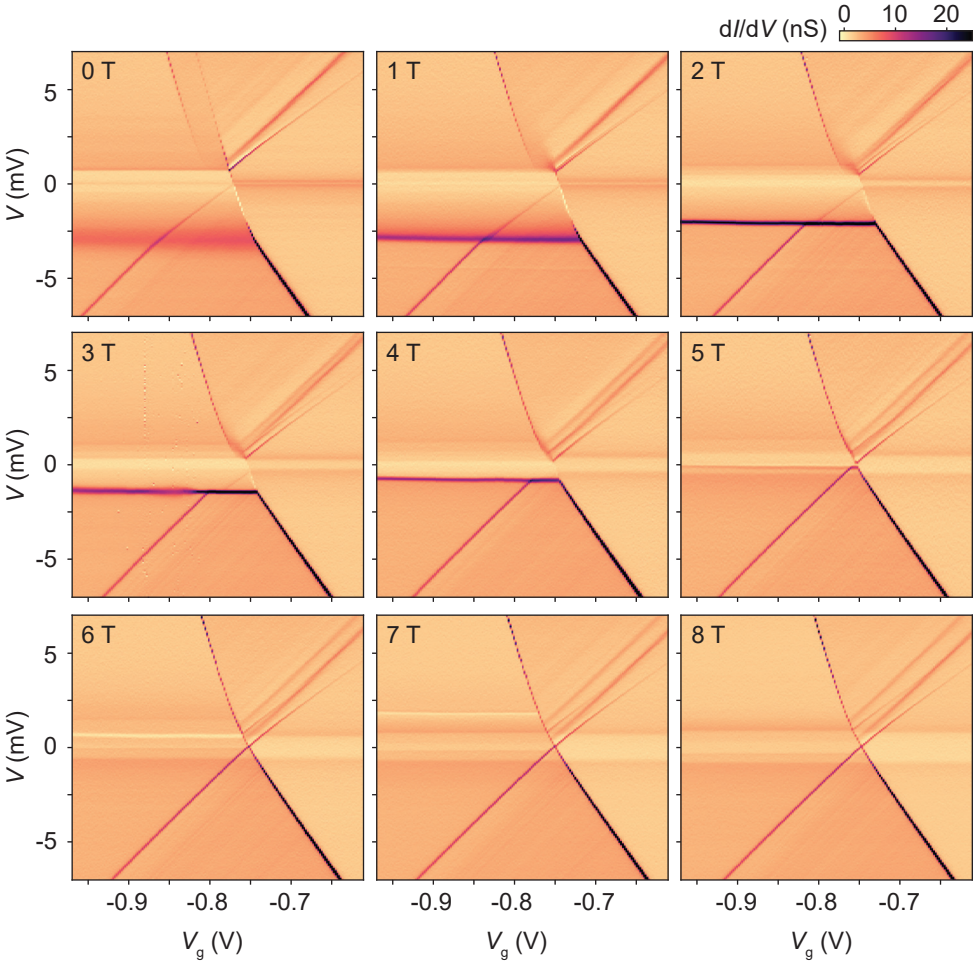

Figure 5.8: Differential conductance maps at different magnetic fields. All maps are recorded in the same gate and bias voltage range at the indicated B-field. The GSSB is gradually lifted as the ground-state transition line moves upwards by the magnetic field.

REFERENCES

[1] **J. de Bruijckere**, P. Gehring, M. Palacios-Corella, M. Clemente-León, E. Coronado, J. Paaske, P. Hedegård, and H. S. J. van der Zant. "Ground-State Spin Blockade in a Single-Molecule Junction". *Physical Review Letters* 122.19 (May 2019). DOI: 10.1103/physrevlett.122.197701.

[2] C. Allain, S. Favette, L.-M. Chamoreau, J. Vaissermann, L. Ruhlmann, and B. Hasenknopf. "Hybrid Organic-Inorganic Porphyrin-Polyoxometalate Complexes". *European Journal of Inorganic Chemistry* 2008.22 (Aug. 2008), pp. 3433–3441. DOI: 10.1002/ejic.200701331.

[3] L. Bogani and W. Wernsdorfer. "Molecular spintronics using single-molecule magnets". In: *Nanoscience and Technology*. Co-Published with Macmillan Publishers Ltd, UK, Aug. 2009, pp. 194–201. DOI: 10.1142/9789814287005_0020.

[4] S. Sanvito. "Molecular spintronics". *Chemical Society Reviews* 40.6 (2011), p. 3336. DOI: 10.1039/c1cs15047b.

[5] J. M. Clemente-Juan, E. Coronado, and A. Gaita-Ariño. "Magnetic polyoxometalates: from molecular magnetism to molecular spintronics and quantum computing". *Chemical Society Reviews* 41.22 (2012), p. 7464. DOI: 10.1039/c2cs35205b.

[6] M. N. Leuenberger and D. Loss. "Quantum computing in molecular magnets". *Nature (London)* 410.6830 (Apr. 2001), pp. 789–793. DOI: 10.1038/35071024.

[7] S. Thiele, F. Balestro, R. Ballou, S. Klyatskaya, M. Ruben, and W. Wernsdorfer. "Electrically driven nuclear spin resonance in single-molecule magnets". *Science* 344.6188 (June 2014), pp. 1135–1138. DOI: 10.1126/science.1249802.

[8] M. Shiddiq, D. Komijani, Y. Duan, A. Gaita-Ariño, E. Coronado, and S. Hill. "Enhancing coherence in molecular spin qubits via atomic clock transitions". *Nature (London)* 531.7594 (Mar. 2016), pp. 348–351. DOI: 10.1038/nature16984.

[9] F. H. L. Koppens. "Control and Detection of Singlet-Triplet Mixing in a Random Nuclear Field". *Science* 309.5739 (Aug. 2005), pp. 1346–1350. DOI: 10.1126/science.1113719.

[10] A. C. Johnson, J. R. Petta, C. M. Marcus, M. P. Hanson, and A. C. Gossard. "Singlet-triplet spin blockade and charge sensing in a few-electron double quantum dot". *Physical Review B* 72.16 (Oct. 2005). DOI: 10.1103/physrevb.72.165308.

[11] H. W. Liu, T. Fujisawa, Y. Ono, H. Inokawa, A. Fujiwara, K. Takashina, and Y. Hirayama. "Pauli-spin-blockade transport through a silicon double quantum dot". *Physical Review B* 77.7 (Feb. 2008). DOI: 10.1103/physrevb.77.073310.

[12] J. Koch and F. von Oppen. "Franck-Condon Blockade and Giant Fano Factors in Transport through Single Molecules". *Physical Review Letters* 94.20 (May 2005). DOI: 10.1103/physrevlett.94.206804.

[13] R. Leturcq, C. Stampfer, K. Inderbitzin, L. Durrer, C. Hierold, E. Mariani, M. G. Schultz, F. von Oppen, and K. Ensslin. "Franck–Condon blockade in suspended carbon nanotube quantum dots". *Nature Physics* 5.5 (Apr. 2009), pp. 327–331. DOI: 10.1038/nphys1234.

[14] E. Burzurí, Y. Yamamoto, M. Warnock, X. Zhong, K. Park, A. Cornia, and H. S. J. van der Zant. "Franck-Condon Blockade in a Single-Molecule Transistor". *Nano Letters* 14.6 (May 2014), pp. 3191–3196. DOI: 10.1021/nl500524w.

[15] C. B. Winkelmann, N. Roch, W. Wernsdorfer, V. Bouchiat, and F. Balestro. "Superconductivity in a single-C_{60} transistor". *Nature Physics* 5.12 (Oct. 2009), pp. 876–879. DOI: 10.1038/nphys1433.

[16] M. T. Deng, S. Vaitiekėnas, E. B. Hansen, J. Danon, M. Leijnse, K. Flensberg, J. Nygård, P. Krogstrup, and C. M. Marcus. "Majorana bound state in a coupled quantum-dot hybrid-nanowire system". *Science* 354.6319 (Dec. 2016), pp. 1557–1562. DOI: 10.1126/science.aaf3961.

[17] D. Weinmann, W. Häusler, and B. Kramer. "Spin Blockades in Linear and Nonlinear Transport through Quantum Dots". *Physical Review Letters* 74.6 (Feb. 1995), pp. 984–987. DOI: 10.1103/physrevlett.74.984.

[18] H. B. Heersche, Z. de Groot, J. A. Folk, H. S. J. van der Zant, C. Romeike, M. R. Wegewijs, L. Zobbi, D. Barreca, E. Tondello, and A. Cornia. "Electron Transport through Single Mn_{12} Molecular Magnets". *Physical Review Letters* 96.20 (May 2006). DOI: 10.1103/physrevlett.96.206801.

[19] R. Gaudenzi, **J. de Bruijckere**, D. Reta, I. de P. R. Moreira, C. Rovira, J. Veciana, H. S. J. van der Zant, and E. Burzurí. "Redox-Induced Gating of the Exchange Interactions in a Single Organic Diradical". *ACS Nano* 11.6 (May 2017), pp. 5879–5883. DOI: 10.1021/acsnano.7b01578.

[20] L. P. Rokhinson, L. J. Guo, S. Y. Chou, and D. C. Tsui. "Spin transitions in a small Si quantum dot". *Physical Review B* 63.3 (Jan. 2001). DOI: 10.1103/physrevb.63.035321.

[21] A. K. Hüttel, H. Qin, A. W. Holleitner, R. H. Blick, K. Neumaier, D. Weinmann, K. Eberl, and J. P. Kotthaus. "Spin blockade in ground-state resonance of a quantum dot". *Europhysics Letters (EPL)* 62.5 (June 2003), pp. 712–718. DOI: 10.1209/epl/i2003-00431-5.

[22] H. Park, A. K. L. Lim, A. P. Alivisatos, J. Park, and P. L. McEuen. "Fabrication of metallic electrodes with nanometer separation by electromigration". *Applied Physics Letters* 75.2 (July 1999), pp. 301–303. DOI: 10.1063/1.124354.

[23] K. O'Neill, E. A. Osorio, and H. S. J. van der Zant. "Self-breaking in planar few-atom Au constrictions for nanometer-spaced electrodes". *Applied Physics Letters* 90.13 (Mar. 2007), p. 133109. DOI: 10.1063/1.2716989.

[24] W. Liang, M. P. Shores, M. Bockrath, J. R. Long, and H. Park. "Kondo resonance in a single-molecule transistor". *Nature (London)* 417.6890 (June 2002), pp. 725–729. DOI: 10.1038/nature00790.

[25] C. Stevanato, M. Leijnse, K. Flensberg, and J. Paaske. "Finite-bias conductance anomalies at a singlet-triplet crossing". *Physical Review B* 86.16 (Oct. 2012). DOI: 10.1103/physrevb.86.165427.

[26] E. Burzurí, R. Gaudenzi, and H. S. J. van der Zant. "Observing magnetic anisotropy in electronic transport through individual single-molecule magnets". *Journal of Physics: Condensed Matter* 27.11 (Feb. 2015), p. 113202. DOI: 10.1088/0953-8984/27/11/113202.

[27] S. Herzog and M. R. Wegewijs. "Dzyaloshinskii-Moriya interaction in transport through single-molecule transistors". *Nanotechnology* 21.27 (June 2010), p. 274010. DOI: 10.1088/0957-4484/21/27/274010.

[28] W. G. van der Wiel, S. D. Franceschi, J. M. Elzerman, S. Tarucha, L. P. Kouwenhoven, J. Motohisa, F. Nakajima, and T. Fukui. "Two-Stage Kondo Effect in a Quantum Dot at a High Magnetic Field". *Physical Review Letters* 88.12 (Mar. 2002). DOI: 10.1103/physrevlett.88.126803.

[29] M. Pustilnik and L. I. Glazman. "Kondo Effect in Real Quantum Dots". *Physical Review Letters* 87.21 (Nov. 2001). DOI: 10.1103/physrevlett.87.216601.

[30] T. Miyamachi, M. Gruber, V. Davesne, M. Bowen, S. Boukari, L. Joly, F. Scheurer, G. Rogez, T. K. Yamada, P. Ohresser, E. Beaurepaire, and W. Wulfhekel. "Robust spin crossover and memristance across a single molecule". *Nature Communications* 3.1 (Jan. 2012). DOI: 10.1038/ncomms1940.

[31] V. Meded, A. Bagrets, K. Fink, R. Chandrasekar, M. Ruben, F. Evers, A. Bernand-Mantel, J. S. Seldenthuis, A. Beukman, and H. S. J. van der Zant. "Electrical control over the Fe(II) spin crossover in a single molecule: Theory and experiment". *Physical Review B* 83.24 (June 2011). DOI: 10.1103/physrevb.83.245415.

[32] E. A. Osorio, K. Moth-Poulsen, H. S. J. van der Zant, J. Paaske, P. Hedegård, K. Flensberg, J. Bendix, and T. Bjørnholm. "Electrical Manipulation of Spin States in a Single Electrostatically Gated Transition-Metal Complex". *Nano Letters* 10.1 (Jan. 2010), pp. 105–110. DOI: 10.1021/nl9029785.

[33] M. Ternes. "Spin excitations and correlations in scanning tunneling spectroscopy". *New Journal of Physics* 17.6 (June 2015), p. 063016. DOI: 10.1088/1367-2630/17/6/063016.

[34] A. Abhervé, M. Palacios-Corella, J. M. Clemente-Juan, R. Marx, P. Neugebauer, J. van Slageren, M. Clemente-León, and E. Coronado. "Bimetallic Mn^{III}-Fe^{II} hybrid complexes formed by a functionalized Mn^{III} Anderson polyoxometalate coordinated to Fe^{II}: observation of a field-induced slow relaxation of magnetization in the Mn^{III} centres and a photoinduced spin-crossover in the Fe^{II} centres". *Journal of Materials Chemistry C* 3.30 (2015), pp. 7936–7945. DOI: 10.1039/c5tc01089f.

6

SUPERCONDUCTING SINGLE-MOLECULE DEVICES

Having discussed single-molecule devices with normal-metal electrodes we now turn to the development of devices with superconducting (SC) electrodes. By applying the electromigration procedure to these devices we are able to study SC transport through individual molecules. While two-terminal SC molecular junctions can be realized in e.g. scanning tunneling microscopy or mechanical break junctions, electromigrated break junctions allow for the realization of SC three-terminal single-molecule transistors. The additional gate electrode enables the tuning of several properties of the junction such as the level alignment, the charge state, the spin state and the Kondo temperature. In addition, both resonant and off-resonant transport regimes can be studied. This tunability allows for studying transport in a regime of exceptionally high charging energy where one can study the interaction between superconductivity and the unique properties of molecules, such as high-spin ground states and magnetic anisotropy. In this chapter we discuss the development of single-molecule devices with both intrinsically superconducting electrodes and proximity-induced superconducting electrodes. We present transport measurements of various devices and highlight a single-level superconducting device which shows gate-tunable subgap resonances and multiple Andreev reflections.

Electrons in a superconductor are all part of a macroscopic condensate of bound pairs. Removing a single electron from this condensate costs a certain energy given by the superconducting gap Δ. Since transport in single-molecule devices is typically governed by *single*-electron processes one might wonder what happens if the electrodes contacting the molecule are superconductors. This question can be experimentally addressed within the field of hybrid superconductor devices [1] which has been attracting an increasing amount of attention in recent years. Various nano-objects in combination with superconductors have been studied, including semiconductor nanowires [2], carbon nanotubes [3], graphene [4] and C_{60} molecules [5]. In this chapter, we focus on the development of hybrid superconducting device platforms which can be used to study individual molecules between superconducting electrodes. We combine the electromigration technique [6] — a well-established method for creating single-molecule transistors with normal-metal electrodes [7] — with superconductivity. To this end, we consider two different approaches:

- The simplest approach is to keep using gold for the electrodes and utilize the proximity effect to induce superconductivity in them. This approach requires the deposition of a superconductor near the gold junction. We refer to these electrodes as *proximity-induced superconducting electrodes*. The advantage of this approach is the compatibility with the well-established electromigration procedure of gold nanobridges. In addition, by using gold one can benefit from the inertness to oxidation, the flat (Fermi-gas-like) density of states and the established ability to contact a vast range of molecules. A disadvantage is that for proximity-induced superconductivity the superconducting gap, the critical field and the critical temperature are reduced. In addition, the coherence peaks in the density of states become broader and less suitable for high-resolution spectroscopy.
- The second approach is to replace gold altogether by a superconducting material. We refer to these electrodes as *intrinsically superconducting electrodes*. A requirement for the success of this approach is that the electrode material needs to be compatible with the electromigration procedure in order to realize molecular junctions. Using this approach the disadvantages of the proximity effect could potentially be avoided.

In this chapter, we discuss the fabrication efforts towards both proximity-induced and intrinsically superconducting single-molecule devices and focus on several devices that were used for transport measurements. The superconducting materials used in this chapter are, respectively, lead, aluminum, molybdenum rhenium and niobium titanium nitride.

6.1. LEAD ELECTRODES

The first superconductor we discuss is lead (Pb). Lead is a type-I conventional superconductor with a critical temperature $T_c \approx 7.2\,\mathrm{K}$ and a superconducting gap of $\Delta \approx 1.3\,\mathrm{meV}$. Lead has recently attracted a lot of attention as a superconducting substrate material in scanning tunneling microscopy [8, 9] due to its suitable surface morphology and relatively high T_c and Δ.

6.1.1. DEPOSITION OF LEAD

Using lead in nanofabrication does require modifications to the standardized fabrication steps used for other metals due to the relatively low melting point of lead: 327 degrees Celsius. Fabrication steps that expose the lead nanostructures to high temperatures should therefore be avoided. In addition, since the native oxide of lead does not protect further oxidation and degradation of the nanostructure — as in the case of aluminum — exposure to air should be minimized and fabrication steps that accelerate oxidation — such as plasma cleaning — should be avoided. Furthermore, lead dissolves in water which limits the use water and water-based solutions in wet bench processes. The reactivity of lead to water is reflected by the fact that purified water has proven to be an effective lead etchant [10]. To avoid the aforementioned constraints the evaporation of lead was designed to be the last deposition step in the device fabrication.

The deposition of lead is known to work best when the substrate is cooled to cryogenic temperatures [11]. Deposited lead has a strong tendency to dewet on a surface and cooling the substrate lowers the mobility of the adatoms which thereby improves the wetting properties. We used an electron beam evaporator in which no cooling stage was available. The deposition of the material was optimized to work at room temperature, although significant dewetting was unavoidable. Further optimization might require cooling the substrate on e.g. a liquid-nitrogen stage or a liquid-helium stage [12].

Figure 6.1 shows scanning electron microscopy images of lead-based intrinsically superconducting electrodes. These electrodes are deposited without any capping layer such that the dewetted lead surface is exposed. The thickness of the lead layer is 50 nm, which proved to be the minimum thickness for lead to form a fully connected electrode at room temperature. Disconnected lead patches were unavoidable in thinner layers. Figure 6.2 shows images of proximity-induced superconducting devices with lead patches. The electromigrated part is a gold nanowire with a thickness of 12 nm, as in the all-gold single-molecule devices used in previous chapters. The patches connecting the nanowire and the contact pads in Figure 6.2a are made from evaporated lead with a thickness of 70 nm and a gold capping of 30 nm. The patches in Figure 6.2b only consist of a lead layer with a thickness of 120 nm. The capping layer is added in an attempt to suppress oxidation and reduce the degradation rate of the lead structure. Oxidation could still take place via the sides and limiting the exposure to air is still required. A potential disadvantage of capping lead by a normal metal is reducing its superconducting properties by the inverse proximity effect, although this effect may be negligible in thick lead structures (see Section 2.4.3).

In Figure 6.2b no capping layer is used and the surface morphology resembles that of the electrodes in Figure 6.2a. Even though significant dewetting occurs, reflected by the discontinuities at the edges of the gate electrode, the junction is still well defined and follows the intended design in which a 100 nm gold nanowire is exposed. Despite the discontinuities, various junctions of this type were connected throughout and could be electromigrated and subsequently measured.

6.1.2. ELECTROMIGRATION OF LEAD CONSTRICTIONS

We performed preliminary electromigration tests at room temperature on the intrinsically superconducting lead devices to study whether lead is compatible with the elec-

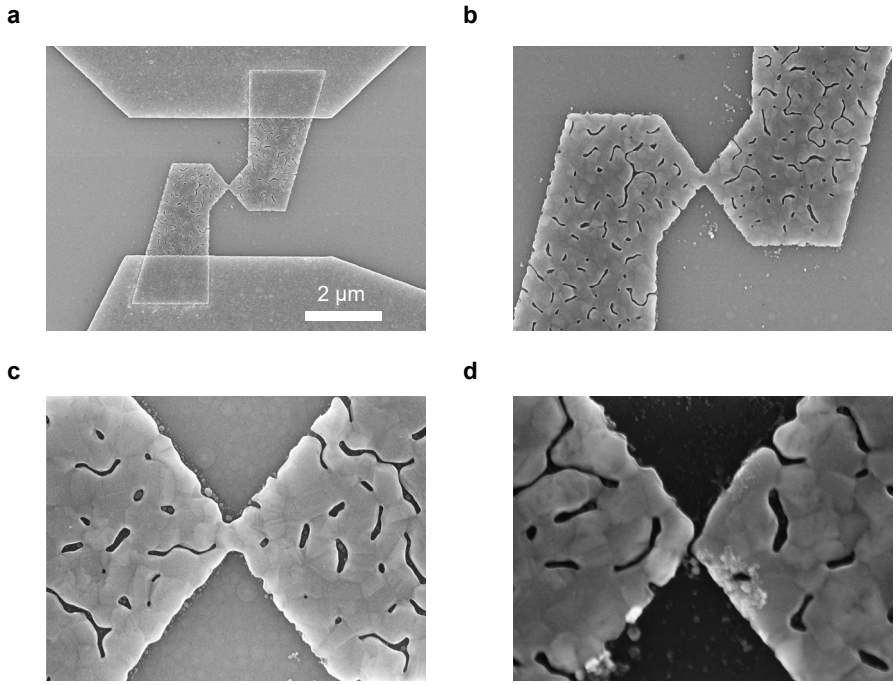

Figure 6.1: Scanning electron microscope images of the lead-based intrinsically superconducting transport devices. **a.** Overview of the device, showing the lead electrodes in the center and gold contact pads at the top and bottom of the image. **b.** Closeup of the lead electrodes, showing the dewetted surface morphology. **c.** The lead constriction before electromigration. **d.** The lead constriction after electromigration, which shows a gap between the electrodes.

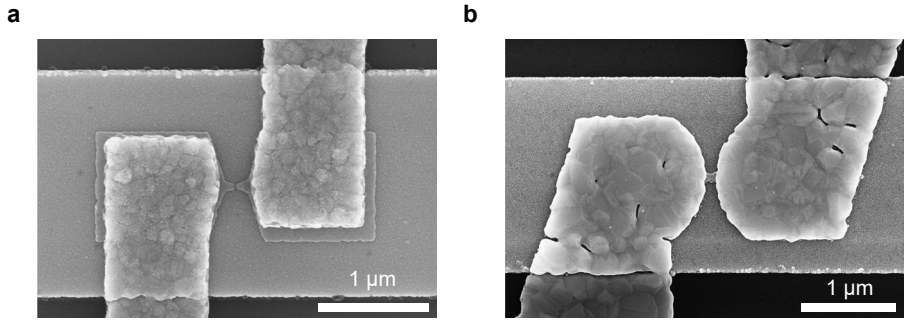

Figure 6.2: Proximity-induced superconducting lead devices with a gold nanowire of 12 nm. **a.** Patches of 70 nm of lead, capped by 30 nm of gold, after electromigration of the gold nanowire. **b.** Uncapped lead patches of 120 nm thick, before electromigration.

tromigration technique. Figure 6.1d shows an electromigrated lead junction in which a clear gap can be observed. The formation of gaps was successful in all tested lead junctions, however the gap sizes were all too large to be used as tunnel junctions. We found that even with very conservative electromigration parameters the lead junctions opened up very quickly, rendering it impossible to realize a stable tunnel junction. Whereas for gold electrodes electromigration typically starts for bias voltages around 1 V, a bias voltage as low as 50 mV was sufficient to open up a lead junction to the point where no tunnel current could be measured. Subsequent self-breaking of the lead junction may increase the gap between the electrodes even more. These preliminary tests therefore suggest that the direct electromigration of lead to create superconducting single-molecule junctions is at least impractical. Changes in the protocol and an optimization of the electromigration parameters would be required in order to check the viability of direct electromigration of lead constrictions.

One approach towards more stable electromigrated lead tunnel junctions could be low-temperature electromigration, although this would complicate the subsequent deposition of molecules onto the junction. A second approach would be changing the design of the constriction at which the electromigration takes place. Since lead has a strong tendency to dewet, more rounded constriction shapes — such as two touching semicircles — could potentially result in more stable junction geometries.

The complications associated with direct electromigration of lead are less of a concern in the proximity-induced lead-based devices shown in Figure 6.2. We found that we could successfully electromigrate certain devices to obtain measurable tunnel junctions. The electromigration process behaved in the same way as for all-gold devices and no changes in the procedure were required. We did not find any indications that the electromigration process might have affected the lead patches — e.g. through heating — as can be seen in Figure 6.2a.

6.1.3. TUNNEL SPECTRA OF LEAD JUNCTIONS

We cooled down the electromigrated proximitized lead devices to measure the induced superconducting properties of the tunnel junction. Figure 6.3a and Figure 6.3b show the IV-characteristics (red lines) and $\mathrm{d}I/\mathrm{d}V$ spectra (blue lines) of a single junction at $T = 0.5\,\mathrm{K}$ and $T = 2.2\,\mathrm{K}$, respectively. The spectrum of Figure 6.3a contains a superconducting gap of 1.2 mV in which small subgap peaks appear at $V = \pm 0.3\,\mathrm{mV}$. At 2.2 K the peaks become peak-dip structures with prominent negative $\mathrm{d}I/\mathrm{d}V$ dips. As expected for a proximitized junction the superconducting coherence peaks in Figure 6.3a appear more rounded as compared to the sharp coherence peaks observed in intrinsically superconducting tunnel junctions (see Section 2.4.3).

We attribute the appearance of the subgap peaks to a difference in the superconducting gaps of the left and right electrode. In superconductor-superconductor junctions where $\Delta_\mathrm{L} \neq \Delta_\mathrm{R}$ a nonzero temperature gives rise to peaks in the IV-characteristics at $V = \pm|\Delta_\mathrm{L} - \Delta_\mathrm{R}|$ [13], which in the $\mathrm{d}I/\mathrm{d}V$ spectra yields a peak-dip structure with negative $\mathrm{d}I/\mathrm{d}V$ dips. This feature is expected to be more pronounced at higher temperatures, which is also observed in the experimental spectra. The difference in the superconducting gaps may be due to the fact that the formation of the tunnel junction by electromigration did not occur at the center of the constriction. As a result, the distance from

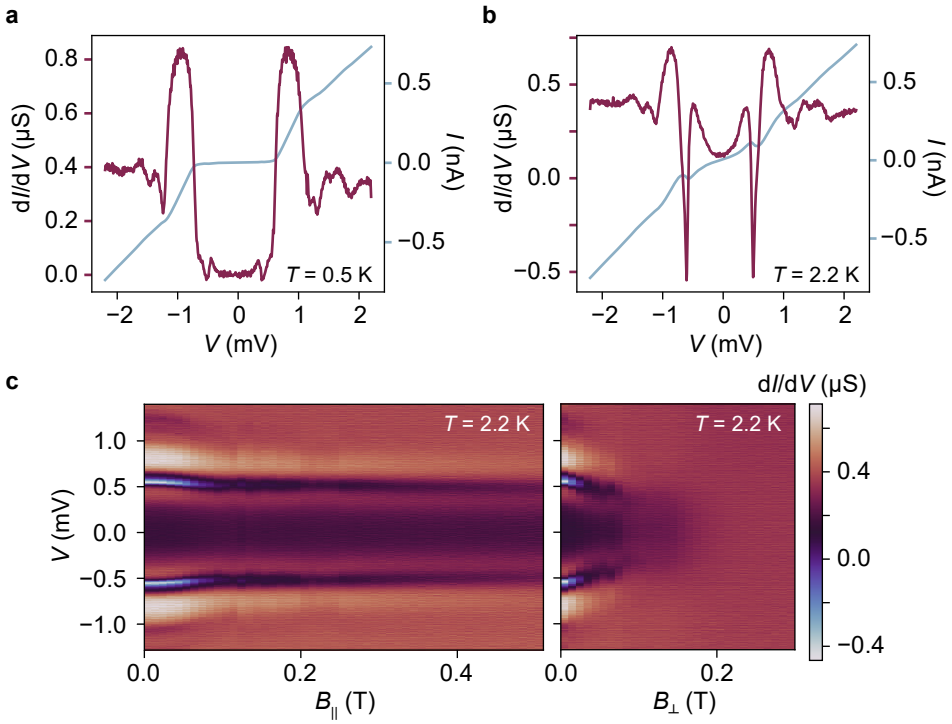

Figure 6.3: Transport data of Pb-based proximity-induced superconducting tunnel junctions. **a.** **(b.)** Current (red) and dI/dV (blue) as a function of the bias voltage, recorded at T = 0.5 K (T = 2.2 K). **c.** Evolution of the dI/dV spectrum in parallel and perpendicular magnetic field.

the tunnel junction to the superconducting patch is different on both sides, which yields the unequal gap sizes (see Section 2.4.3). Better control over the position of the junction might be achieved by designing a more strongly tapered constriction for which the current density is more localized at the constriction's center.

Alternative explanations for the appearance of the subgap peaks include the occurrence of multiple Andreev reflections (MAR), which are known to give subgap features at $V = \pm 2\Delta/ne$, where $n = 2, 3, 4, \ldots$ (see Section 2.5). This explanation however is not consistent with the observed temperature dependence of the experimental spectra: MAR features would be thermally broadened by the temperature rather than becoming more pronounced.

Figure 6.3c shows the evolution of the dI/dV spectrum in a parallel magnetic field $B_\parallel$ and a perpendicular magnetic field $B_\perp$. The two measurements show a clear difference in the degree to which superconductivity is suppressed by the magnetic field. When the magnetic field is oriented parallel to the plane of the superconducting layer the critical field is significantly higher, as expected for thin-film nanostructures [13].

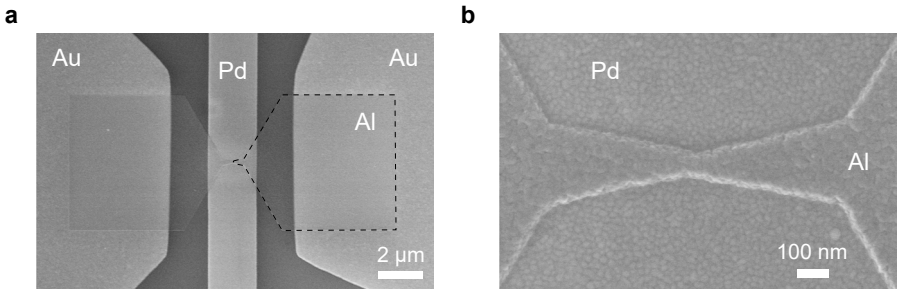

Figure 6.4: Aluminum-based intrinsically superconducting device before electromigration. **a.** Overview of the device in which the bow-tie shaped aluminum electrode is shown (marked by the dashed contour on the right side) along with the palladium gate electrode (vertical strip running through the middle of the image), covered with aluminum oxide, and the two gold contact pads on the right and left. **b.** Closeup image of the aluminum constriction.

6.2. ALUMINUM ELECTRODES

Perhaps the most commonly used superconductor in nanoscale devices is aluminum. This is in part due to the protective properties of aluminum's native oxide. Even in ambient conditions aluminum-based devices can remain stable over long periods of time. Aluminum is a conventional type-I superconductor with a critical temperature $T_c = 1.2\,\mathrm{K}$ and a superconducting gap $\Delta = 0.17\,\mathrm{meV}$. The relatively small size of the superconducting gap is a disadvantage of using aluminum for this work, as it becomes more challenging to resolve subgap features such as multiple Andreev reflections and Yu-Shiba-Rusinov states. In the case of proximity-induced superconducting electrodes — where the induced gap is even further reduced — this disadvantage would be even more significant.

6.2.1. DEPOSITION OF ALUMINUM

We used electron-beam evaporation to deposit aluminum electrodes designed for intrinsically superconducting single-molecule devices. Figure 6.4 shows two scanning electron microscopy images of the fabricated aluminum-based devices. The bow-tie shaped structure in Figure 6.4a — marked on the right side by a dashed line — is the aluminum electrode of which the tapered part is to be electromigrated. The vertical strip in the middle of the image is the palladium gate electrode, covered with aluminum oxide, and the left and right structures are the gold contact pads. Since aluminum is a relatively light atom the 50 nm-thick aluminum electrode has a low contrast in the scanning electron microscopy image. Figure 6.4b shows a closeup image of the aluminum constriction before electromigration. The contours of the constriction appear well defined and the surface morphology is more uniform compared to the lead-based devices shown in Figure 6.1.

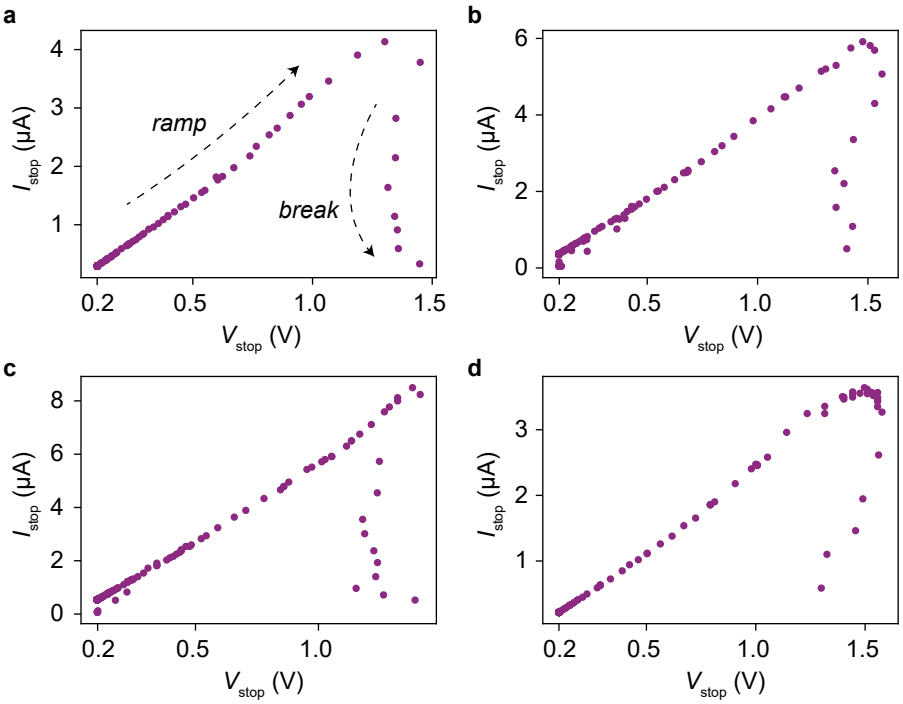

Figure 6.5: Representative electromigration IV-characteristics of aluminum-based intrinsically superconducting junctions. The points indicate at which bias voltage V_{stop} and current I_{stop} the bias-voltage ramps were stopped by the feedback loop. In these devices electromigration sets in around 1.5 V.

6.2.2. ELECTROMIGRATION OF ALUMINUM CONSTRICTIONS

We performed controlled electromigration experiments on the aluminum constrictions using the same procedure as for all-gold devices. The direct electromigration of aluminum has been reported before [5, 14], albeit at low temperatures. Here we focused on room-temperature electromigration in an attempt to maintain the same protocol of molecule deposition used in all-gold devices. We performed controlled electromigration of the aluminum devices up to a resistance of about 8 kΩ. Figure 6.5 shows the electromigration IV-curves of the aluminum constrictions. The dots in the plot indicate the current and the bias voltage at which the bias-voltage ramp is stopped by the feedback (see Section 1.2.3 for details on the electromigration protocol).

Above the target resistance of 8 kΩ, the signal-to-noise ratio in the feedback-controlled loop is too low for further electromigration. In all-gold devices, self-breaking starts at this point: The junction gradually opens further without any bias voltage applied over the course of hours until the tunneling condition $R \gg h/2e^2 \approx 13\,\mathrm{k\Omega}$ is reached. The devices are then cooled down to prevent further self-breaking. In the aluminum devices however, the resistance did not change over time after electromigration. Since no self-breaking occurs, electromigration up to tunneling resistances would be required to

realize aluminum-based tunnel- and single-molecule junctions. In the present setup, the signal-to-noise ratio limits controlled electromigration in this resistance range. Tunneling currents cannot be measured at sufficiently high rates. We resorted to the use of proximity-induced superconducting junctions with aluminum patches of which the electromigration worked successfully and similar to all-gold devices.

6.2.3. TRANSPORT THROUGH ALUMINUM JUNCTIONS

We performed transport measurements on the proximity-induced superconducting devices with aluminum patches at low temperatures ($T \approx 40\,\mathrm{mK}$) of which the results are shown in Figure 6.6. A small non-linearity appears at low bias in the IV-characteristic of Figure 6.6a which takes the shape of a soft superconducting gap in the (superimposed) $\mathrm{d}I/\mathrm{d}V$ spectra. Even at this low temperature of 40 mK the gap is not reaching zero conductance. The small size of the induced gap may play a role in this: With an estimated peak separation of 0.08 mV — which equals 4Δ in superconductor-superconductor junctions — we estimate the induced gap to be $\Delta = 0.02\,\mathrm{meV}$. As $\Delta \approx 4k_\mathrm{B}T$ thermal broadening of the $\mathrm{d}I/\mathrm{d}V$ spectra can at this low temperature still be expected. In combination with the broadening effect of the proximity effect we obtain the soft-gap spectrum of Figure 6.6b. A larger gap and sharper spectral features might be realized by placing the aluminum patches closer to the junction in the device design.

Figure 6.6c shows the suppression of the superconducting gap by a perpendicular and a parallel magnetic field. As in the measurements of the lead-based devices (see Figure 6.3c) we observe the expected increase in critical magnetic field for magnetic fields oriented parallel to plane of the aluminum layer.

6.3. MOLYBDENUM RHENIUM ELECTRODES

In the following we focus on preliminary transport measurements of a proximity-induced superconducting single-molecule device using the superconducting compound molybdenum rhenium (MoRe) and an Fe_4 single-molecule magnet (SMM) [15]. A scanning electron microscopy image of the device is shown in Figure 6.7a and a schematic representation of the Fe_4 SMM is shown in Figure 6.7b. The fabrication is described in detail by Gaudenzi *et al.* (2015) [16].

In Figure 6.8 we present the stability diagram of the MoRe-based single-molecule device in both normal scale (a) and logarithmic scale (b). We observe a charge degeneracy point at $V_\mathrm{g} = 2.73\,\mathrm{V}$ and a region of suppressed $\mathrm{d}I/\mathrm{d}V$ between the edges at $V = \pm 0.5\,\mathrm{mV}$, which reflects the induced superconducting state of the electrodes. The sum of the induced superconducting gaps of the two electrodes corresponds to the size of the $\mathrm{d}I/\mathrm{d}V$ gap, such that $\Delta_1 + \Delta_2 \approx 0.5\,\mathrm{meV}$. The $\mathrm{d}I/\mathrm{d}V$ gap appears to close and reopen upon crossing the charge degeneracy point, which is highlighted by the white dashed lines in Figure 6.8b. In addition, the $\mathrm{d}I/\mathrm{d}V$ is significantly higher around this transition.

The opening and closing of the gap by the gate voltage strongly resembles observations of gate-tunable subgap resonances — referred to as Andreev bound states (ABS) or Yu-Shiba-Rusinov (YSR) bound states — in superconductor-quantum dot-normal metal (S-QD-N) systems [17–20]. These subgap resonances result from the coupling between the superconducting electrode and the discrete states of the quantum dot and are probed

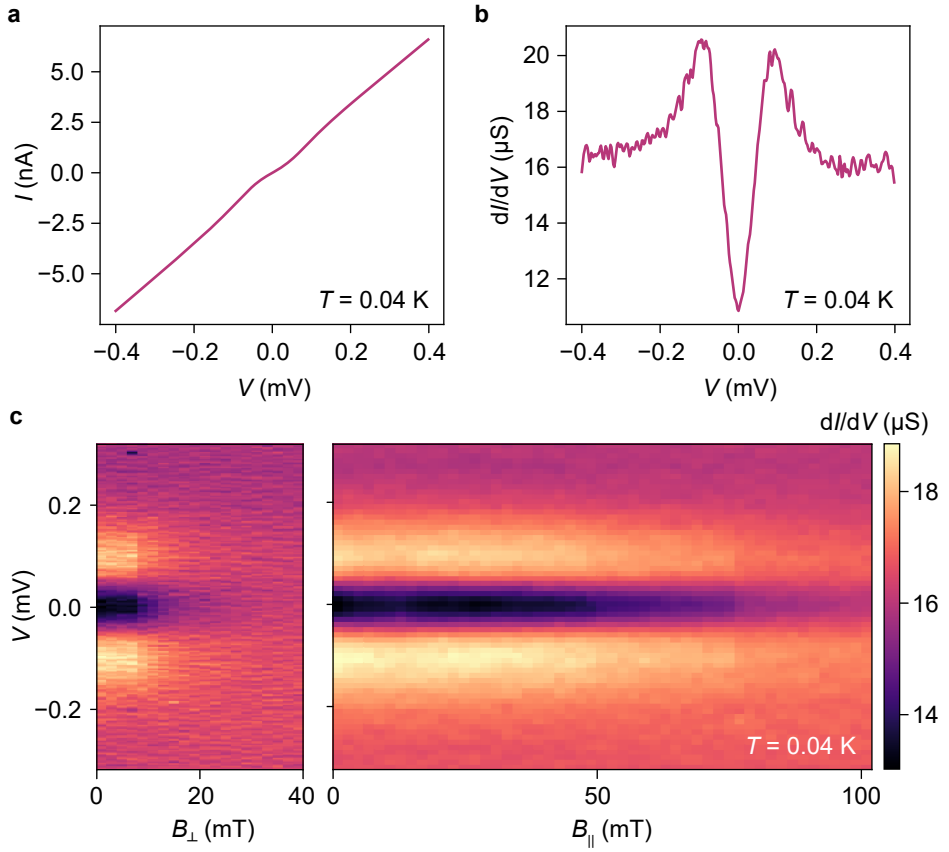

Figure 6.6: Transport measurements of proximity-induced superconducting junctions with aluminum patches. **a.** Low-bias IV-characteristic showing nonlinear behavior as a result of the induced superconductivity. **b.** $\mathrm{d}I/\mathrm{d}V$ spectra showing a soft gap and superconducting coherence peaks at $V = \pm 0.1\,\mathrm{mV}$. **c. (d.)** Evolution of the $\mathrm{d}I/\mathrm{d}V$ spectrum in a perpendicular (parallel) magnetic field.

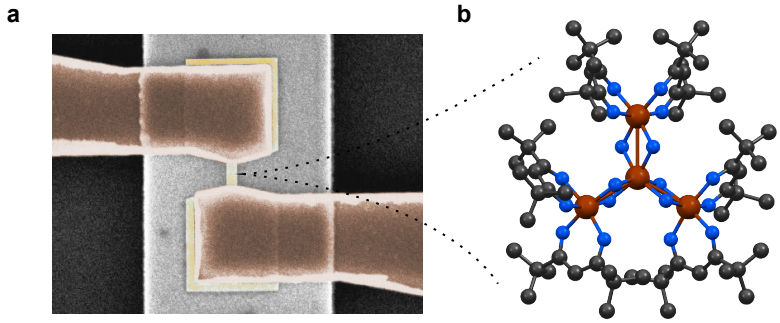

Figure 6.7: a. Scanning electron microscopy image of a proximity-induced superconducting device with MoRe electrodes (brown) connected through a gold nanowire with a separation of 250 nm. **b.** Schematic representation of an Fe_4 single-molecule magnet where the iron atoms are colored dark orange, the nitrogen atoms dark blue and the carbon atoms black. The hydrogen atoms are omitted for clarity.

by the normal electrode of the S-QD-N system. By varying the gate voltage the energy of the subgap resonances can be manipulated and can be tuned across zero energy near the charge degeneracy points. This zero-bias crossing is also observed in Figure 6.8, as highlighted by the white dashed lines. Despite the similarities, the device in Figure 6.7a is designed to have superconducting electrodes on *both* sides, in contrast to the S-QD-N devices. Similar gate-dependent subgap resonances can be observed in superconductor-quantum dot-superconductor (S-QD-S) systems [3, 21, 22]. One of the differences between the spectra of S-QD-S devices and S-QD-N devices is that the dI/dV gap does not close at any gate voltage in S-QD-S devices due to the superconducting gap, Δ, of the second electrode — bound-state resonances crossing zero energy are shifted from zero bias in the dI/dV spectrum by this Δ (see e.g. Pillet *et al.* (2010) [3]). Since the gap in Figure 6.8 appears to close completely at $V_g = 2.73\,V$, the measurements of this single-molecule device are not consistent with an S-QD-S system, but rather resemble the behavior of an S-QD-N system.

To explain why the presented data is similar to the behavior of an S-QD-N system rather than that of an S-QD-S system we need to consider the experimental aspects of the electromigration process. As discussed in Section 1.2.3, the position of the electromigrated gap in the gold nanowire (shown in the middle of Figure 6.7a) cannot be precisely controlled. Even more so in the initial design geometry shown in Figure 6.7 where the gold nanowire has the same width throughout. The gap formation in this device could in principle occur at any position in the nanowire and may be close to one of the superconductors and far from the other. As the induced superconducting correlations are suppressed with distance (see Section 2.4.3) the resulting device may effectively behave as a S-QD-N system, where Δ_1 is large and Δ_2 is too small to resolve. In later devices, we added a constriction in the design of the gold nanowire (see e.g. Figure 6.2a) to increase the chances of the gap forming at the center. The appearance of the gate-tunable subgap resonances in this device might thus be attributed to an ABS/YSR state which results from the coupling between the molecule and one of the superconducting electrodes,

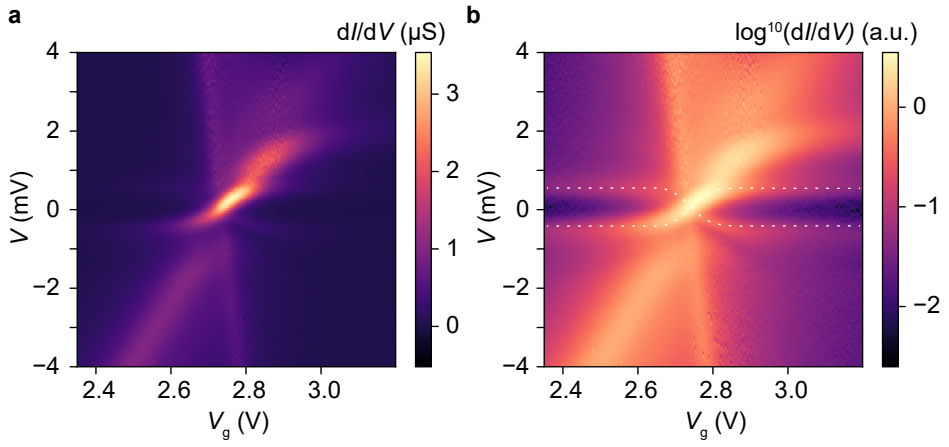

Figure 6.8: Stability diagrams of the MoRe-based proximity-induced superconducting single-molecule device shown in Figure 6.7a. The molecule in the junction is an Fe_4 single-molecule magnet, which is sketched in Figure 6.7b. **a.** dI/dV around a charge resonance showing the Coulomb-blockade edges and a strong enhancement of the dI/dV at the charge degeneracy point. **b.** Logarithm of the dI/dV for better visibility of the gate-dependent subgap resonances (marked by white dashed lines).

6

probed by the other — effectively normal — electrode.

In the tentative interpretation above we approximated the Fe_4 SMM by a simple quantum dot and neglected its additional degrees of freedom, such as the high spin of the Fe_4 core [15], the magnetic anisotropy [23, 24] and the vibrational excitations [25]. As superconducting transport through a simple quantum dot is by itself difficult to treat from a theoretical point of view [26, 27] adding the interaction with the molecular degrees of freedom is not attempted in this work, but might be of potential interest for future studies. Several features in Figure 6.8, such as the enhanced dI/dV around the charge degeneracy point and the appearance of the cotunneling excitation at $V = 2\,\mathrm{mV}$ to the right of the charge degeneracy point may be understood in terms of the molecular degrees of freedom and their interaction with the superconductor.

6.4. NIOBIUM TITANIUM NITRIDE ELECTRODES

The last material we discuss is the compound niobium titanium nitride (NbTiN). This superconductor is commonly used in hybrid superconductor-semiconductor nanowire devices, mainly for its relatively high critical magnetic field [2, 28]. The large superconducting gap of NbTiN ($\Delta \approx 1.3\,\mathrm{meV}$) also makes it an attractive material for the proximity-induced superconducting electrodes in this work.

6.4.1. DEPOSITION OF NBTIN

We deposited NbTiN by sputtering from a Nb/Ti target in a nitrogen-rich atmosphere. Figure 6.9 shows images of the resulting devices. The unwanted overlap between the

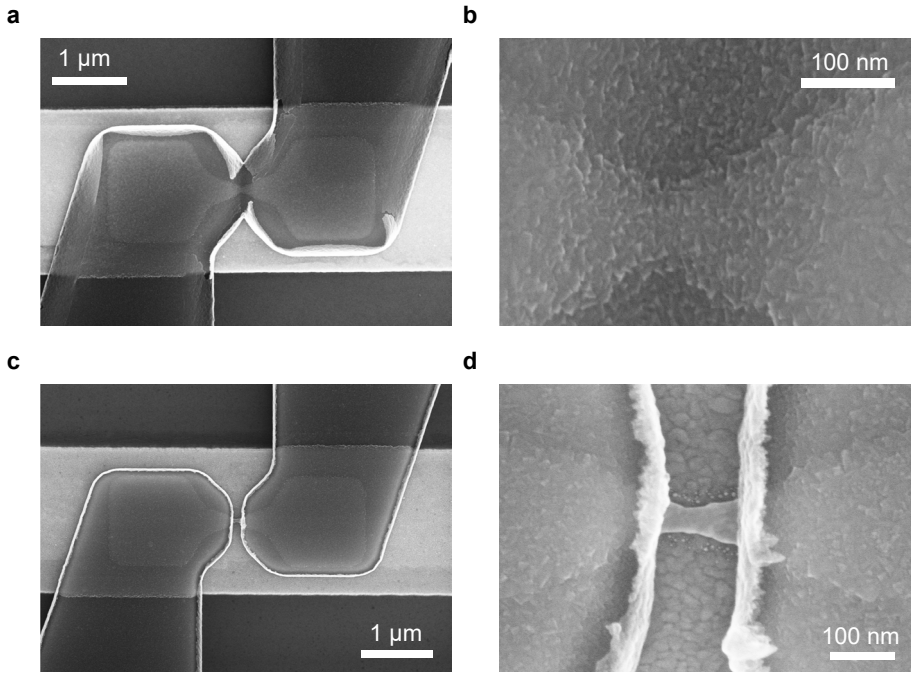

Figure 6.9: Scanning electron microscopy images of proximity-induced superconducting junctions with NbTiN patches designed for single-molecule studies. **a.** Resist stack with large undercut results in overlap between the NbTiN patches illustrating the isotropic nature of deposition by sputtering. **b.** Closeup of the constriction showing the surface morphology. **c.** Resist stack with small undercut results in the desired separation between the electrodes. **d.** Closeup of the gold constriction showing a separation of about 100 nm between the NbTiN patches.

electrodes in the first image is due to the deposited material underneath the undercut in the resist layers which illustrates the isotropic nature of deposition by sputtering. In Figure 6.9b a closeup image of the constriction — covered by the NbTiN patch — is presented, which shows the surface morphology of the NbTiN layer. In a subsequent fabrication round, the desired pattern was obtained by selecting a combination of resists which results in a small undercut. The result is shown in Figure 6.9c where the NbTiN patches are separated by the gold nanowire. A closeup of the exposed constriction is shown in Figure 6.9d.

6.4.2. TUNNEL SPECTRA OF NBTIN JUNCTIONS

The proximity-induced superconducting devices with NbTiN patches proved to be compatible with electromigration and tunnel junctions could be realized successfully. We performed preliminary transport measurements at low temperatures on these devices to study the induced superconducting properties. Representative $\mathrm{d}I/\mathrm{d}V$ spectra of four different tunnel junctions are presented in Figure 6.10. All spectra contain supercon-

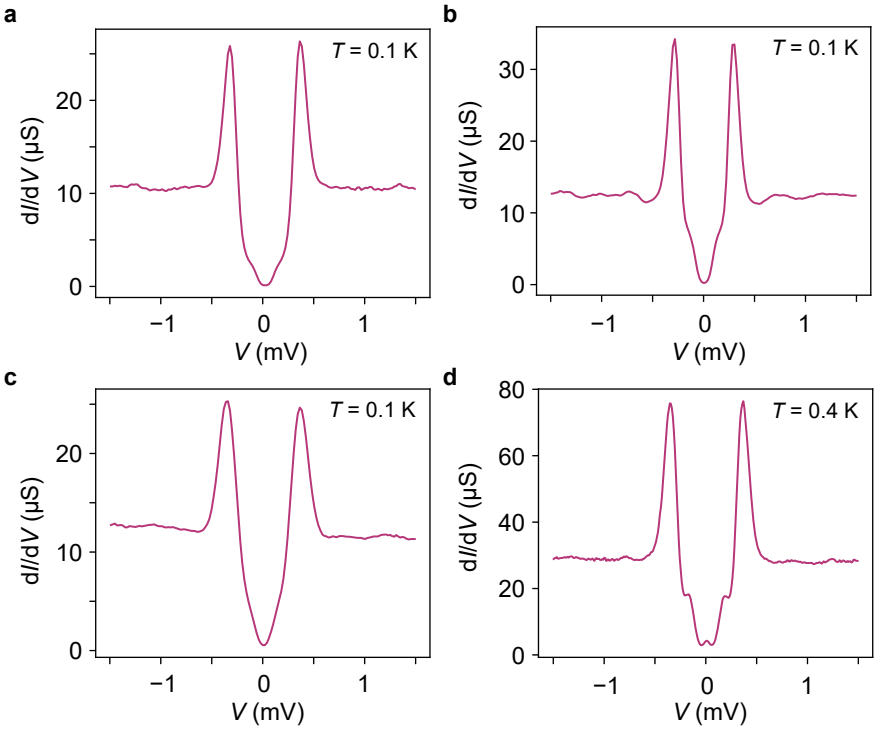

Figure 6.10: Representative $\mathrm{d}I/\mathrm{d}V$ spectra of the electromigrated proximity-induced superconducting junctions with NbTiN patches. All spectra show superconducting coherence peaks at $V = \pm 0.35\,\mathrm{mV}$ along with shoulders within the gap which might result from first-order Andreev reflections.

ducting coherence peaks which appear around $\pm 0.35\,\mathrm{meV}$. As the coherence peaks in superconductor-superconductor junctions appear at $V = \pm 2\Delta/e$ we estimate the average proximity-induced gap to be $\Delta_{\mathrm{prox}} \approx 0.17\,\mathrm{meV}$.

The induced gaps in the $\mathrm{d}I/\mathrm{d}V$ spectra do not go to zero completely. Instead, shoulders of finite $\mathrm{d}I/\mathrm{d}V$ appear at $V \approx \pm 0.15\,\mathrm{mV}$ in all spectra. We attribute the appearance of these shoulders to multiple Andreev reflections (MAR). The signature for MAR is the appearance of a subgap structure where peaks appear at $2\Delta/ne$ for $n = 2, 3, 4, \ldots$ (see Section 2.5). The cutoff of n depends on the transparency of the junction and the phase coherence time. Here, we only observe the first-order peak at $V \approx \Delta/e$.

In the spectrum of Figure 6.10d a zero-bias peak appears in addition to the MAR shoulders. This peak most like results from the fact that the measurement temperature was higher than in the other spectra. At zero bias, the quasiparticle excitation peaks of both superconducting electrodes are at the same energy, which leads to an enhancement of the quasiparticle current when these states become thermally populated. This thermal enhancement results in the observed zero-bias peak.

In most NbTiN devices the gate voltage did not significantly influence the $\mathrm{d}I/\mathrm{d}V$ spec-

tra, as expected for bare superconductor-superconductor junctions. However, in the device corresponding to the spectrum in Figure 6.10d a charge degeneracy point was observed, which indicates the presence of an impurity between the electrodes. The transport measurements of this device are presented in Section 6.4.3.

6.4.3. SINGLE-LEVEL IMPURITY IN A NBTIN DEVICE

Of all the measured NbTiN-based proximitized tunnel junctions one device unexpectedly exhibited Coulomb blockade, which suggests that a nanoscale object — e.g. a single molecule or a metallic grain — is embedded between the superconducting electrodes. The measured stability diagrams of this device are shown in Figure 6.11. Since only a single charge degeneracy point appears within the accessible gate-voltage range this system effectively behaves as a single-level impurity. Although we do not know the nature of the impurity, it can still serve as a platform for studying superconducting transport through a single-level nano-object.

The superconducting state of the electrodes is reflected by the gap in the low-bias region of Figure 6.11a, which extends throughout the full gate-voltage range. Figure 6.11b shows the stability diagram at a finite magnetic field of $B = 1\,\mathrm{T}$ where no gap is observed and superconductivity is suppressed. In both stability diagrams a single charge degeneracy point appears at $V_g \approx 0.9\,\mathrm{V}$ from which four Coulomb edges extend towards positive and negative bias voltages. In the left Coulomb-blockaded region a step in the $\mathrm{d}I/\mathrm{d}V$ appears at $V = \pm 9\,\mathrm{mV}$, which signals the onset of transport through an inelastic cotunneling (COT) channel (see Section 2.2 for an explanation of COT). The COT excitation continues as an sequential-electron-tunneling (SET) excitation upon crossing the leftmost Coulomb edges (see Section 2.1 for a discussion about SET excitations).

Detailed stability diagrams of the low-bias region around the charge degeneracy point are shown in Figure 6.11c and d. The gap in the $\mathrm{d}I/\mathrm{d}V$ appears between the $\mathrm{d}I/\mathrm{d}V$ peaks at $V = \pm 0.33\,\mathrm{mV}$. The $\mathrm{d}I/\mathrm{d}V$ peaks appear where the bias voltage exceeds the sum of the induced gaps such that quasiparticles from one electrode can be injected in the other. This implies that $\Delta_1 + \Delta_2 = 0.33\,\mathrm{meV}$. We observe several lines of enhanced $\mathrm{d}I/\mathrm{d}V$ within the gap, which are highlighted by the white dashed lines in Figure 6.11d. The lines move towards zero bias by tuning the gate voltage towards the charge degeneracy point.

Before discussing the subgap behavior at the center of the stability diagram we first focus on the regions at the left- and right-hand side of the charge degeneracy point, i.e., where the charge of the impurity is fixed. In Figure 6.12a we show two $\mathrm{d}I/\mathrm{d}V$ spectra, which are measured at fixed gate voltages on both sides of the charge degeneracy point. The spectrum recorded at $V_g = 0.72\,\mathrm{V}$ shows a pair of $\mathrm{d}I/\mathrm{d}V$ steps at $V = \pm 0.12\,\mathrm{mV}$ and a less clear pair of shoulders at $V = \pm 0.21\,\mathrm{mV}$, as indicated by the black arrows. In the spectrum corresponding to $V_g = 1.05\,\mathrm{V}$ these features are largely suppressed and only a pair of shoulders at $V \approx \pm 0.1\,\mathrm{mV}$ may be identified. In addition, the overall $\mathrm{d}I/\mathrm{d}V$ is lower at $V_g = 1.05\,\mathrm{V}$ as compared to $V_g = 0.72\,\mathrm{V}$.

Since the impurity is confined between two superconducting electrodes the NbTiN-based device is expected to behave as a superconductor-quantum dot-superconductor (S-QD-S) system with proximity-induced superconducting gaps in both electrodes, Δ_1 and Δ_2. It is known that in S-QD-S systems subgap peaks can appear as a result of multiple Andreev reflections (MAR) [27]. In case the quantum dot is symmetrically coupled to

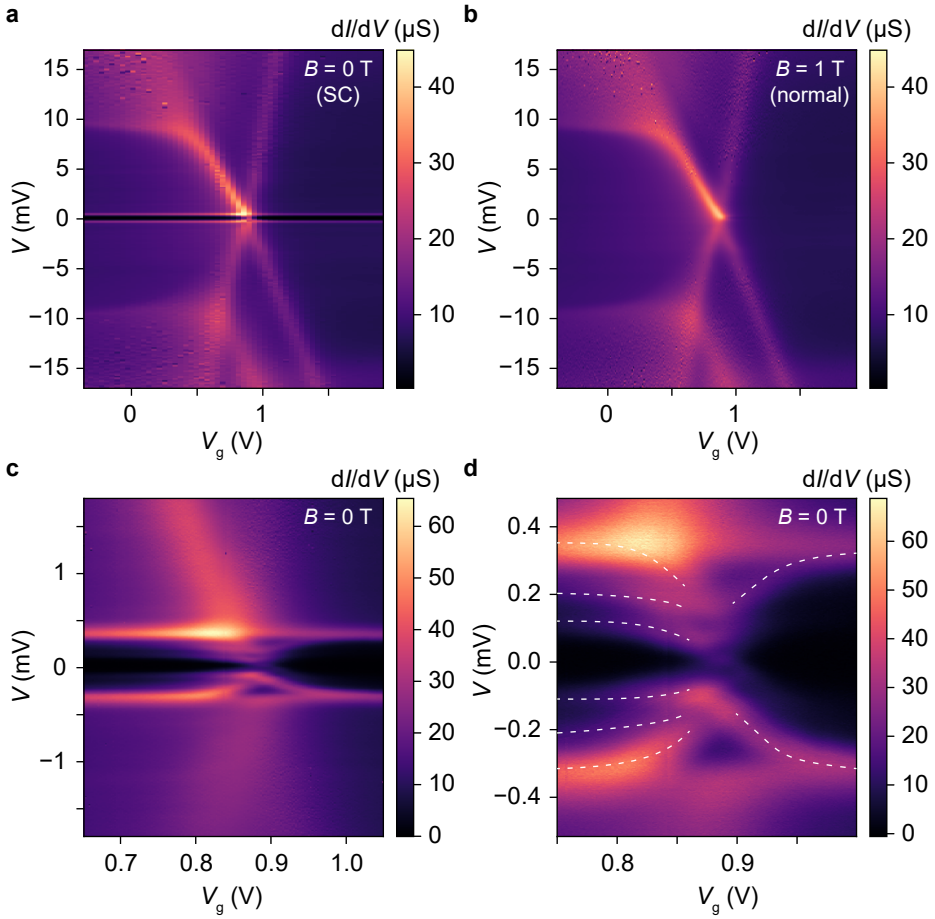

Figure 6.11: Transport measurements of a NbTiN-based proximity-induced superconducting junction exhibiting Coulomb blockade. **a.** Stability diagram of the superconducting state ($B = 0\,\mathrm{T}$) showing a single charge resonance and a superconducting gap at low bias. Cotunneling excitation lines appear at $V = \pm 9\,\mathrm{mV}$. **b.** Stability diagram of the normal state ($B = 1\,\mathrm{T}$) where no superconducting gap is present. **c.** Detailed stability diagram of the region around the charge resonance showing a superconducting gap at $V \approx \pm 0.3\,\mathrm{mV}$ along with the appearance of gate-dependent subgap resonances. **d.** Closeup of **c** in which the subgap resonances are highlighted by white dashed lines.

the electrodes and the superconducting gaps are equal the peaks appear at $|V| = 2\Delta/ne$ for $n = 2,3,4,...$. For unequal gaps, i.e., $\Delta_1 \neq \Delta_2$, the lowest order subgap peaks can be found at $|V| = \Delta_1$ and $|V| = \Delta_2$ [29]. Since we cannot fully control the position of the electromigrated gap, the induced superconducting gaps will generally be different, as discussed in Section 1.2.3. The indicated subgap features in Figure 6.12a may thus be due to the lowest order MAR processes at $V = \pm\Delta_1 = \pm 0.21\,\text{mV}$ and $V = \pm\Delta_2 = \pm 0.12\,\text{mV}$. This is corroborated by the fact that the quasiparticle peaks appear at $V = \pm 0.33\,\text{mV}$, which equals $\Delta_1 + \Delta_2$.

The intensity difference of the MAR features may be due to a Kondo-enhancement of MAR, as observed in InAs nanowire quantum dots [30] and carbon nanotubes [31]. Even though the Kondo effect and superconductivity are competing phenomena [32], MAR features may be enhanced due to the Kondo correlations in the odd charge states. According to this interpretation, the left-hand side of the stability diagrams in Figure 6.11 would correspond to the odd charge state and the right-hand side to the even charge state. The presence of Kondo correlations is corroborated by the asymmetry in the linear conductance — or $\mathrm{d}I/\mathrm{d}V|_{V=0}$— around the charge degeneracy point in the normal state, as shown in Figure 6.12b. The observed enhancement of the linear conductance in the odd charge state is a typical fingerprint of Kondo-enhanced transport [33]. We note that in contrast with other experiments [30, 31], we do not observe a zero-bias Kondo resonance in the stability diagram of the normal state (see Figure 6.11b). This suggests that the Kondo coupling is weak and if there is any Kondo-enhancement of MAR at all, it must be a relatively small effect.

Thus far, we have only considered the symmetric-coupling limit of the S-QD-S system, in which MAR-mediated transport prevails. In the asymmetric limit — where the quantum dot is strongly coupled to one electrode and weakly to the other — transport through S-QD-S systems is governed by tunneling through localized Yu-Shiba-Rusinov (YSR) states [27]. The YSR states form as a result of the interaction between the quantum dot's spin and the strongly-coupled electrode and appear as excitations within the superconducting gap. The weakly-coupled electrode in the S-QD-S system effectively probes the YSR excitations, which then appear as subgap features in the $\mathrm{d}I/\mathrm{d}V$ spectrum. Although we cannot accurately determine the asymmetry in the tunnel couplings, we note that the maximum linear conductance of the Coulomb peak in the normal state is $\mathrm{d}I/\mathrm{d}V|_{V=0} = 37\,\mu\text{S}$, which is about half the conductance quantum $G_0 \equiv 2e^2/h$. Since G_0 equals the conductance of a fully transparent channel, both electrodes are likely to be strongly coupled to the impurity with a relatively low asymmetry factor. Realistically, the coupling is never fully symmetric and neither of the two theoretical limits fully describes the experimental case. The experiment takes place in the intermediate regime, which is the most difficult regime to treat from a theoretical point of view [27] and is therefore not yet fully understood.

After having discussed the $\mathrm{d}I/\mathrm{d}V$ spectra in the two fixed charge states we now focus on the region between the charge states. As Figure 6.11c and d show, the subgap features move as a function of the gate voltage and approach zero bias upon reaching the charge degeneracy point. A similar gate-dependence of the subgap features near a charge degeneracy point has previously been observed in carbon nanotube quantum dot devices [34]. The behavior was understood within the limits of a resonant level model,

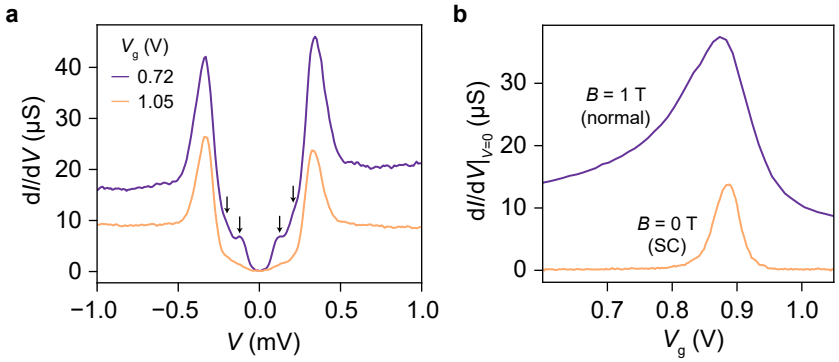

Figure 6.12: a. $\mathrm{d}I/\mathrm{d}V$ spectra in the two fixed charge states that correspond the left- and right-hand side of the charge degeneracy point shown in Figure 6.11. The spectrum measured at $V_g = 0.72\,\mathrm{V}$ shows MAR-like subgap features, as indicated by the arrows. These features are largely suppressed in the spectrum recorded at $V_g = 1.5\,\mathrm{V}$. **b.** Linear conductance as a function of gate voltage in the normal ($B = 1\,\mathrm{T}$) and the superconducting state ($B = 0\,\mathrm{T}$). The linear conductance in the superconducting state is largely suppressed due to the induced superconducting gaps in the electrodes, except for the peak around $V_g = 0.88\,\mathrm{V}$. In the normal state, a Coulomb peak with asymmetric tails appears.

which neglects the charging energy and considers the tunnel couplings to be the largest energy scale. In the measurements presented here, the charging energy is by far the largest energy scale making the resonant level model unsuitable. Even though the limit of asymmetric coupling discussed above is also not fully applicable in this device, the gate-dependence of the subgap features may still be understood in terms of YSR-like bound states. Within the interpretation of YSR states the gate dependence of the subgap lines reflects the tuning of the YSR state's energy E_{YSR} by the gate's electric field, as observed in quantum dots coupled to a single superconducting electrode [20]. The most significant change in E_{YSR} is observed across the charge degeneracy point where the subgap lines move towards zero-bias.

An expected fingerprint for YSR states in S-QD-S systems is a negative differential conductance (NDC) dip at the outer edges of the bound-state resonance peaks [21, 27, 35, 36]. In Figure 6.11 however, we do not observe these NDC dips at any gate voltage. This discrepancy can be explained by the following two reasons: (i) The coupling in the junction is not sufficiently asymmetric to describe transport in terms of tunneling through YSR states. Instead, the intermediate regime applies, for which no theoretical predictions are available and in which the NDC dip might not appear. (ii) By employing the proximity effect the electrodes do not behave as BCS superconductors with sharp superconducting coherence peaks. More rounded features appear in the induced local density of states (see Section 2.4.3) which may modify the spectrum of the asymmetric S-QD-S system to a degree that the NDC dips no longer appear.

We finally discuss the observed linear conductance peak in the superconducting state ($B = 0\,\mathrm{T}$), shown in Figure 6.12b. As expected, the linear conductance on both sides

of the peak is largely suppressed by the superconducting gaps in the electrodes, below which no quasiparticle tunneling can occur. The increase in the linear conductance at $V_g = 0.88\,\mathrm{V}$ however, cannot be explained by quasiparticle tunneling. Instead, the peak might result from Cooper-pair tunneling, which is strongly enhanced at the charge resonance of the impurity. At any other gate voltage, Cooper-pair tunneling is largely suppressed due to the large charging energy of the impurity. The charging energy for a Cooper pair is even larger due to its $2e$-charge quantization. Still, when the impurity level is on resonance, a measurable Josephson current might develop when the tunnel coupling exceeds the superconducting gap, i.e., $\Gamma \gg \Delta$ [37]. In this limit, the electrons of the Cooper pair may coherently tunnel through the level in a sequential manner, such that the charging energy for Cooper pairs does not play a role.

6.5. CONCLUDING REMARKS

In this chapter we discussed the development of superconducting single-molecule devices using different electrode materials. We first focused on the superconductor lead, which is a promising material in terms of its superconducting properties — high critical field and large superconducting gap — but comparatively difficult to use in device fabrication due to the strong tendency to dewet on surfaces, the low melting point and the susceptibility to oxidation. Depositing lead at cryogenic temperatures may however significantly improve the wetting and make lead an attractive material for proximity-induced superconducting devices. Direct electromigration of lead was attempted, but proved to be challenging due to the instability of the constriction at low bias voltages. The disadvantages of lead in the device fabrication are less of a concern for aluminum, MoRe and NbTiN. For these materials we realized stable proximity-induced superconducting junctions and presented low-temperature transport data showing superconducting behavior. A disadvantage of aluminum compared to the other materials is the small superconducting gap of $\sim 0.17\,\mathrm{meV}$, further reduced by the proximity effect, which makes it less suitable for studies on subgap states. In that regard, the compounds MoRe and NbTiN with bulk gaps of $\sim 1.3\,\mathrm{meV}$ are more attractive to use in these types of devices. Apart from the $\mathrm{d}I/\mathrm{d}V$ spectra of bare superconducting tunnel junctions we presented data of MoRe-based and NbTiN-based devices which exhibited Coulomb blockade.

The MoRe-based device showed a closing and reopening of the gap in the $\mathrm{d}I/\mathrm{d}V$ across a charge degeneracy point, which we tentatively interpret as the zero-energy crossing of a YSR bound state. We argued that the zero-bias crossing could only occur if the second electrode effectively behaved as a normal-metal electrode, which is plausible considering the uncertainty in the position of the electromigrated gap. A constriction in the nanowire design would result in better control over the size of the superconducting gaps in both electrodes.

One NbTiN-based device also exhibited Coulomb blockade with gate-tunable subgap resonances. We expect this device to be in an intermediate tunnel-coupling regime between the limits of symmetric coupling, where MAR features are expected, and strongly asymmetric couplings, in which transport is governed by tunneling through YSR bound states. The observed MAR/YSR-like subgap resonances appeared more intense in one of the two charge states, which may be due to the Kondo-enhancement of the underly-

ing transport processes. In the superconducting state, a linear-conductance peak was present at the charge degeneracy point, which we attributed to a resonant Josephson current. The presented measurements provide a demonstration of the complex interaction between a single level and superconducting electrodes, which may motivate further experimental studies using the employed combination of electromigration and the proximity effect. In addition, the experimental data shows that a deeper theoretical understanding is needed to fully capture the emerging transport phenomena in these devices.

REFERENCES

[1] S. D. Franceschi, L. P. Kouwenhoven, C. Schönenberger, and W. Wernsdorfer. "Hybrid superconductor-quantum dot devices". *Nature Nanotechnology* 5.10 (Sept. 2010), pp. 703–711. DOI: 10.1038/nnano.2010.173.

[2] V. Mourik, K. Zuo, S. M. Frolov, S. R. Plissard, E. P. A. M. Bakkers, and L. P. Kouwenhoven. "Signatures of Majorana Fermions in Hybrid Superconductor-Semiconductor Nanowire Devices". *Science* 336.6084 (Apr. 2012), pp. 1003–1007. DOI: 10.1126/science.1222360.

[3] J.-D. Pillet, C. H. L. Quay, P. Morfin, C. Bena, A. L. Yeyati, and P. Joyez. "Andreev bound states in supercurrent-carrying carbon nanotubes revealed". *Nature Physics* 6.12 (Nov. 2010), pp. 965–969. DOI: 10.1038/nphys1811.

[4] T. Dirks, T. L. Hughes, S. Lal, B. Uchoa, Y.-F. Chen, C. Chialvo, P. M. Goldbart, and N. Mason. "Transport through Andreev bound states in a graphene quantum dot". *Nature Physics* 7.5 (Feb. 2011), pp. 386–390. DOI: 10.1038/nphys1911.

[5] C. B. Winkelmann, N. Roch, W. Wernsdorfer, V. Bouchiat, and F. Balestro. "Superconductivity in a single-C_{60} transistor". *Nature Physics* 5.12 (Oct. 2009), pp. 876–879. DOI: 10.1038/nphys1433.

[6] H. Park, A. K. L. Lim, A. P. Alivisatos, J. Park, and P. L. McEuen. "Fabrication of metallic electrodes with nanometer separation by electromigration". *Applied Physics Letters* 75.2 (July 1999), pp. 301–303. DOI: 10.1063/1.124354.

[7] M. L. Perrin, E. Burzurí, and H. S. J. van der Zant. "Single-molecule transistors". *Chemical Society Reviews* 44.4 (2015), pp. 902–919. DOI: 10.1039/c4cs00231h.

[8] M. Ruby, F. Pientka, Y. Peng, F. von Oppen, B. W. Heinrich, and K. J. Franke. "Tunneling Processes into Localized Subgap States in Superconductors". *Physical Review Letters* 115.8 (Aug. 2015). DOI: 10.1103/physrevlett.115.087001.

[9] D.-J. Choi, C. Rubio-Verdú, **J. de Bruijckere**, M. M. Ugeda, N. Lorente, and J. I. Pascual. "Mapping the orbital structure of impurity bound states in a superconductor". *Nature Communications* 8.1 (May 2017). DOI: 10.1038/ncomms15175.

[10] T. Kanne, M. Marnauza, D. Olsteins, D. J. Carrad, J. E. Sestoft, **J. de Bruijckere**, L. Zeng, E. Johnson, E. Olsson, K. Grove-Rasmussen, and J. Nygård. "Epitaxial Pb on InAs nanowires" (Feb. 26, 2020). arXiv: http://arxiv.org/abs/2002.11641v1 [cond-mat.mes-hall].

[11] D. Weber and E. Scheer. "Superconducting properties of lithographic lead break junctions". *Nanotechnology* 29.4 (Dec. 2017), p. 045703. DOI: 10.1088/1361-6528/aa99b8.

[12] D. Vasyukov, Y. Anahory, L. Embon, D. Halbertal, J. Cuppens, L. Neeman, A. Finkler, Y. Segev, Y. Myasoedov, M. L. Rappaport, M. E. Huber, and E. Zeldov. "A scanning superconducting quantum interference device with single electron spin sensitivity". *Nature Nanotechnology* 8.9 (Sept. 2013), pp. 639–644. DOI: 10.1038/nnano.2013.169.

[13] M. Tinkham. *Introduction to Superconductivity*. Courier Corporation, 2004.

[14] X. D. A. Baumans, D. Cerbu, O.-A. Adami, V. S. Zharinov, N. Verellen, G. Papari, J. E. Scheerder, G. Zhang, V. V. Moshchalkov, A. V. Silhanek, and J. V. de Vondel. "Thermal and quantum depletion of superconductivity in narrow junctions created by controlled electromigration". *Nature Communications* 7.1 (Feb. 2016). DOI: 10.1038/ncomms10560.

[15] S. Accorsi, A.-L. Barra, A. Caneschi, G. Chastanet, A. Cornia, A. C. Fabretti, D. Gatteschi, C. Mortalò, E. Olivieri, F. Parenti, P. Rosa, R. Sessoli, L. Sorace, W. Wernsdorfer, and L. Zobbi. "Tuning Anisotropy Barriers in a Family of Tetrairon(III) Single-Molecule Magnets with an $S = 5$ Ground State". *Journal of the American Chemical Society* 128.14 (Apr. 2006), pp. 4742–4755. DOI: 10.1021/ja0576381.

[16] R. Gaudenzi, J. O. Island, **J. de Bruijckere**, E. Burzurí, T. M. Klapwijk, and H. S. J. van der Zant. "Superconducting molybdenum-rhenium electrodes for single-molecule transport studies". *Applied Physics Letters* 106.22 (June 2015), p. 222602. DOI: 10.1063/1.4922042.

[17] R. S. Deacon, Y. Tanaka, A. Oiwa, R. Sakano, K. Yoshida, K. Shibata, K. Hirakawa, and S. Tarucha. "Tunneling Spectroscopy of Andreev Energy Levels in a Quantum Dot Coupled to a Superconductor". *Physical Review Letters* 104.7 (Feb. 2010). DOI: 10.1103/physrevlett.104.076805.

[18] W. Chang, V. E. Manucharyan, T. S. Jespersen, J. Nygård, and C. M. Marcus. "Tunneling Spectroscopy of Quasiparticle Bound States in a Spinful Josephson Junction". *Physical Review Letters* 110.21 (May 2013). DOI: 10.1103/physrevlett.110.217005.

[19] J. Schindele, A. Baumgartner, R. Maurand, M. Weiss, and C. Schönenberger. "Nonlocal spectroscopy of Andreev bound states". *Physical Review B* 89.4 (Jan. 2014). DOI: 10.1103/physrevb.89.045422.

[20] A. Jellinggaard, K. Grove-Rasmussen, M. H. Madsen, and J. Nygård. "Tuning Yu-Shiba-Rusinov states in a quantum dot". *Physical Review B* 94.6 (Aug. 2016). DOI: 10.1103/physrevb.94.064520.

[21] A. Eichler, M. Weiss, S. Oberholzer, C. Schönenberger, A. L. Yeyati, J. C. Cuevas, and A. Martín-Rodero. "Even-Odd Effect in Andreev Transport through a Carbon Nanotube Quantum Dot". *Physical Review Letters* 99.12 (Sept. 2007). DOI: 10.1103/physrevlett.99.126602.

[22] A. Kumar, M. Gaim, D. Steininger, A. L. Yeyati, A. Martín-Rodero, A. K. Hüttel, and C. Strunk. "Temperature dependence of Andreev spectra in a superconducting carbon nanotube quantum dot". *Physical Review B* 89.7 (Feb. 2014). DOI: 10.1103/physrevb.89.075428.

[23] E. Burzurí, A. S. Zyazin, A. Cornia, and H. S. J. van der Zant. "Direct Observation of Magnetic Anisotropy in an Individual Fe_4 Single-Molecule Magnet". *Physical Review Letters* 109.14 (Oct. 2012). DOI: 10.1103/physrevlett.109.147203.

[24] M. Misiorny, E. Burzurí, R. Gaudenzi, K. Park, M. Leijnse, M. R. Wegewijs, J. Paaske, A. Cornia, and H. S. J. van der Zant. "Probing transverse magnetic anisotropy by electronic transport through a single-molecule magnet". *Physical Review B* 91.3 (Jan. 2015). DOI: 10.1103/physrevb.91.035442.

[25] E. Burzurí, Y. Yamamoto, M. Warnock, X. Zhong, K. Park, A. Cornia, and H. S. J. van der Zant. "Franck-Condon Blockade in a Single-Molecule Transistor". *Nano Letters* 14.6 (May 2014), pp. 3191–3196. DOI: 10.1021/nl500524w.

[26] V. Koerting, B. M. Andersen, K. Flensberg, and J. Paaske. "Nonequilibrium transport via spin-induced subgap states in superconductor/quantum dot/normal metal cotunnel junctions". *Physical Review B* 82.24 (Dec. 2010). DOI: 10.1103/physrevb.82.245108.

[27] B. M. Andersen, K. Flensberg, V. Koerting, and J. Paaske. "Nonequilibrium Transport through a Spinful Quantum Dot with Superconducting Leads". *Physical Review Letters* 107.25 (Dec. 2011). DOI: 10.1103/physrevlett.107.256802.

[28] Ö. Gül, H. Zhang, F. K. de Vries, J. van Veen, K. Zuo, V. Mourik, S. Conesa-Boj, M. P. Nowak, D. J. van Woerkom, M. Quintero-Pérez, M. C. Cassidy, A. Geresdi, S. Koelling, D. Car, S. R. Plissard, E. P. A. M. Bakkers, and L. P. Kouwenhoven. "Hard Superconducting Gap in InSb Nanowires". *Nano Letters* 17.4 (Apr. 2017), pp. 2690–2696. DOI: 10.1021/acs.nanolett.7b00540.

[29] M. Hurd, S. Datta, and P. F. Bagwell. "Current-voltage relation for asymmetric ballistic superconducting junctions". *Physical Review B* 54.9 (Sept. 1996), pp. 6557–6567. DOI: 10.1103/physrevb.54.6557.

[30] T. Sand-Jespersen, J. Paaske, B. M. Andersen, K. Grove-Rasmussen, H. I. Jørgensen, M. Aagesen, C. B. Sørensen, P. E. Lindelof, K. Flensberg, and J. Nygård. "Kondo-Enhanced Andreev Tunneling in InAs Nanowire Quantum Dots". *Physical Review Letters* 99.12 (Sept. 2007). DOI: 10.1103/physrevlett.99.126603.

[31] A. Eichler, R. Deblock, M. Weiss, C. Karrasch, V. Meden, C. Schönenberger, and H. Bouchiat. "Tuning the Josephson current in carbon nanotubes with the Kondo effect". *Physical Review B* 79.16 (Apr. 2009). DOI: 10.1103/physrevb.79.161407.

[32] C. Buizert, A. Oiwa, K. Shibata, K. Hirakawa, and S. Tarucha. "Kondo Universal Scaling for a Quantum Dot Coupled to Superconducting Leads". *Physical Review Letters* 99.13 (Sept. 2007). DOI: 10.1103/physrevlett.99.136806.

[33] S. M. Cronenwett. "A Tunable Kondo Effect in Quantum Dots". *Science* 281.5376 (July 1998), pp. 540–544. DOI: 10.1126/science.281.5376.540.

[34] M. R. Buitelaar, W. Belzig, T. Nussbaumer, B. Babić, C. Bruder, and C. Schönenberger. "Multiple Andreev Reflections in a Carbon Nanotube Quantum Dot". *Physical Review Letters* 91.5 (Aug. 2003). DOI: 10.1103/physrevlett.91.057005.

[35] K. Grove-Rasmussen, H. I. Jørgensen, B. M. Andersen, J. Paaske, T. S. Jespersen, J. Nygård, K. Flensberg, and P. E. Lindelof. “Superconductivity-enhanced bias spectroscopy in carbon nanotube quantum dots”. *Physical Review B* 79.13 (Apr. 2009). DOI: 10.1103/physrevb.79.134518.

[36] K. J. Franke, G. Schulze, and J. I. Pascual. “Competition of Superconducting Phenomena and Kondo Screening at the Nanoscale”. *Science* 332.6032 (May 2011), pp. 940–944. DOI: 10.1126/science.1202204.

[37] L. I. Glazman and K. A. Matveev. “Resonant Josephson current through Kondo impurities in a tunnel barrier”. *JETP* 49.10 (1989), pp. 659–662.

7

SUPERCONDUCTING INAS/PB NANOWIRE ISLAND DEVICES

The last chapter of this thesis is not about single molecules, but focuses on a significantly larger nanostructure, namely a semiconductor nanowire. We use a recently developed hybrid semiconductor-superconductor material system consisting of an indium arsenide (InAs) nanowire with epitaxial lead (Pb) to realize superconducting island devices that have the potential to host topologically non-trivial bound states. In this context, we demonstrate a magnetic-field-driven transition from the 2e-charging regime, where only Cooper pairs can tunnel through the island, to the 1e-charging regime, where single-electron transport occurs through zero-energy bound states; a prerequisite for use in topological quantum computation.

Parts of this chapter have been published in [1]

In this chapter we turn from single molecules to semiconductor nanowires, and in particular hybrid semiconductor-superconductor nanowire devices. This type of device has attracted much attention in recent years for its potential to be used as a topological qubit [2–4]. Here, we focus on a novel hybrid system which consists of an indium arsenide (InAs) nanowire partially covered by epitaxially-grown lead (Pb). Recent measurements of tunnel junctions made from this type of nanowire have demonstrated the excellent superconducting properties of the hybrid InAs/Pb system, showing a hard superconducting gap of $\Delta \sim 1.3\,\text{meV}$ resilient against magnetic fields well above 8 T [1]. We note that the combination of InAs and Pb has been used before [5], albeit with evaporated Pb and not with epitaxially-grown Pb. The resulting critical field of this system was orders of magnitude smaller than the critical field we find in this study and is therefore not suited for topological applications. The large size of the critical field in combination with a hard superconducting gap in the novel InAs/Pb material system is unprecedented in the field of hybrid semiconductor-superconductor nanowire devices and is crucial in suppressing unwanted quasiparticle excitations for topological-qubit operation [6, 7].

In the context of topological superconductivity, a commonly used device architecture is the hybrid semiconductor-superconductor *island*, which consists of a semiconductor nanowire covered by a segment of superconducting material. Under certain conditions, including strong spin-orbit coupling and a magnetic field parallel to the wire, this system has the potential to host topological superconductivity with Majorana zero modes at the ends of the hybrid island [2]. So far, the most commonly used superconducting material for these hybrid island devices has been aluminum. Only recently, the superior properties of epitaxial Pb on InAs nanowires in terms of interface quality and superconductivity have been demonstrated [1]. In the following sections, we focus on transport measurements of the InAs/Pb material system as part of a hybrid island device. These measurements demonstrate the $2e$ quantization of charge and single-electron transport through zero-energy bound states at finite magnetic field, which are essential requirements for topological applications [4, 6, 8–12].

7.1. DEVICE DESCRIPTION

Figure 7.1a shows a scanning electron microscope (SEM) image of an InAs/Pb nanowire on its InAs growth substrate, where the Pb film can be seen on the right-hand side of the wire. A nanowire of this type was deposited on a silicon/silicon-dioxide substrate after which titanium/gold (Ti/Au) contacts and gate electrodes were deposited using e-beam lithography and e-beam evaporation. Before evaporation, the epitaxial Pb was selectively removed by an H_2O etch in the regions where the contacts would be deposited, such that after Ti/Au deposition the epitaxial Pb only remained on a single InAs segment between the contacts. Controlled over-etching ensured that the Pb did not contact the Ti/Au directly. Figure 7.1b shows an SEM image of the finished device and Figure 7.1c shows a schematic drawing of the InAs/Pb island device. In both figures, the InAs/Pb segment is false-colored red and the contacts and gate electrodes yellow. Charge transport is measured as a function of the bias voltage between the two contacts, V, and the voltage applied to the electrostatically coupled gate electrode, V_g, as indicated in Fig-

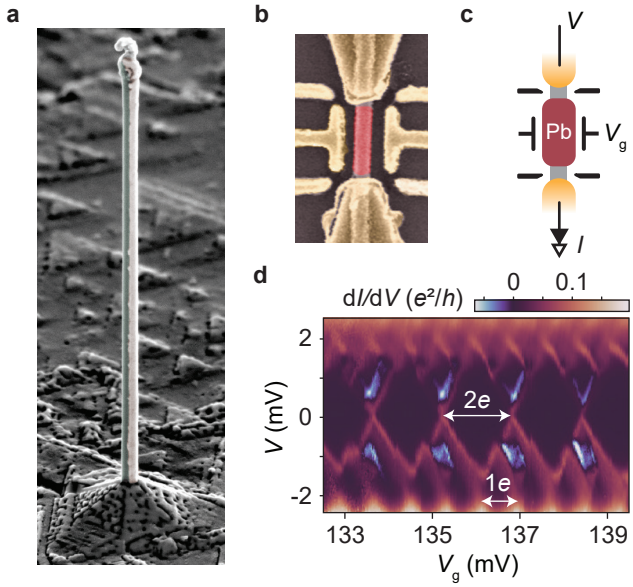

Figure 7.1: a. Scanning electron microscope (SEM) image of an InAs nanowire on its InAs growth substrate, covered on the right-hand side by epitaxial Pb. **b.** SEM image of an InAs/Pb island device, where the Pb segment is false-colored red and the contacts and gate electrodes yellow. **c.** Schematic representation of the island device, showing where the current, I, is measured and where the bias voltage, V, and gate voltage, V_g, are applied. **d.** Differential conductance (dI/dV) map of an InAs/Pb island device, showing Coulomb blockade with $2e$-spaced Coulomb diamonds at low bias and $1e$-spaced charge transitions at high bias. The $2e$- and $1e$-periods are indicated by white arrows. Regions of negative differential conductance indicate the onset of transport through long-lifetime quasiparticle states.

ure 7.1c. The differential conductance, dI/dV, of this device is measured using standard lock-in amplifier techniques. The two T-shaped side gates, or *plunger gates*, control the charge occupation of the island, whereas the other four side gates control the island-contact coupling. In the measurements shown below, the V_g parameter is a linear combination of the two plunger gates. The weights of this linear combination were selected based on dI/dV maps as a function of the two plunger gates, which revealed regions in which the influence of unintentional quantum dots — commonly observed in InAs nanowire devices — was minimal. All measurements are performed in a dilution refrigerator with a base temperature of ~ 30 mK.

7.2. COULOMB-BLOCKADE SPECTROSCOPY

Figure 7.1d shows the measured dI/dV as a function of V and V_g, revealing periodic Coulomb diamonds due to the sequential charging of the superconducting island. Regions of negative differential conductance are present, which indicate the onset of trans-

port through long-lifetime quasiparticle states [4, 8, 9]. When occupied, the quasiparticle states inhibit Cooper pair tunneling, resulting in a decrease of the overall current. In the superconducting state, charge states with an odd number of electrons are lifted in energy by the superconducting gap, Δ. If in this case Δ is larger than the charging energy, $E_C = e^2/2C$, the ground state at any gate voltage has an even number of electrons such that ground-state transitions only occur between even charge states [13]. The charge of the superconducting island is thus quantized in units of $2e$, as indicated by the white arrow in the center of Figure 7.1d. At high-bias, the excess energy from the bias voltage enables transitions between even and odd charge states, resulting in the observed $1e$ periodicity of the charge-state transition lines indicated by the white arrow. As a consequence of the charging in units of $2e$, the addition energy of a superconducting island is four times larger than the addition energy of a normal metal island [8] for which $E_{add} = 2E_C = e^2/C$ [14]. Hence, for a superconducting island $E_{add} = 8E_C = (2e)^2/C \sim 2\,\text{meV}$ and thus $E_C \sim 0.2 - 0.3\,\text{meV}$.

Next, we focus on the magnetic-field dependent behavior of the same InAs/Pb island device in a different gate-voltage range. Figure 7.2a shows three $\mathrm{d}I/\mathrm{d}V$ maps, recorded at different magnetic fields. At $B_\parallel = 0\,\text{T}$, $2e$-periodic charging is observed as in Figure 7.1d, albeit with a smaller addition energy ($\sim 1\,\text{meV}$) due to the different gate-voltage setting. The inset shows the corresponding energy diagram, where the energy of different charge states is plotted as a function of the normalized gate voltage, N_g. The normalization is chosen such that one unit corresponds to the distance between the energy minima of adjacent charge states. The energy of the odd charge state (red parabola) is lifted with respect to the even charge states (black parabolas) by $\Delta > E_C$, such that ground-state energy crossings only occur between even charge states. By applying a magnetic field, the energy of the odd — spinful — charge states is reduced due to the Zeeman interaction. At $B_\parallel = 1.1\,\text{T}$ in Figure 7.2a, a second set of Coulomb diamond appears which forms an alternating pattern of diamonds with different sizes. The energy of the odd charge state is reduced by the magnetic field below E_C (see inset), such that transitions between even and odd states (gray circles) can occur. Upon increasing the magnetic field to $B_\parallel = 1.8\,\text{T}$, the energy minima of the even and odd charge states become equal (see inset, bottom panel) which results in evenly spaced Coulomb diamonds as seen in the measurement. Due to the transition from $2e$- to $1e$-charge quantization the addition energy is now reduced from $8E_C$ to $2E_C$, as expected for superconducting island devices [8]. At the $1e$-spaced charge degeneracy points, pronounced zero-bias peaks appear, which is a fingerprint of single-particle transport through zero-energy bound states, as observed in aluminum-based hybrid nanowire devices [4, 8, 9, 15].

The complete evolution from the $2e$-charging regime to the even-odd regime and finally the $1e$-charging regime is shown in Figure 7.2b, where the zero-bias $\mathrm{d}I/\mathrm{d}V$ is plotted in an extended gate-voltage range as a function of $B_\parallel$. The inset shows the underlying data on a logarithmic scale to highlight the gradual splitting of the $2e$-periodic peaks as $B_\parallel$ is increased. A strong asymmetry in the peak intensity is observed between the two sets of split peaks, which may be due to a difference in the electron-like and hole-like components of the bound states [8, 10, 16]. Towards higher magnetic field the two sets of peaks shift from an alternating even-odd spacing to a uniform $1e$ spacing. Concomitantly, the peak intensity of the even and odd peaks becomes equal. In the following

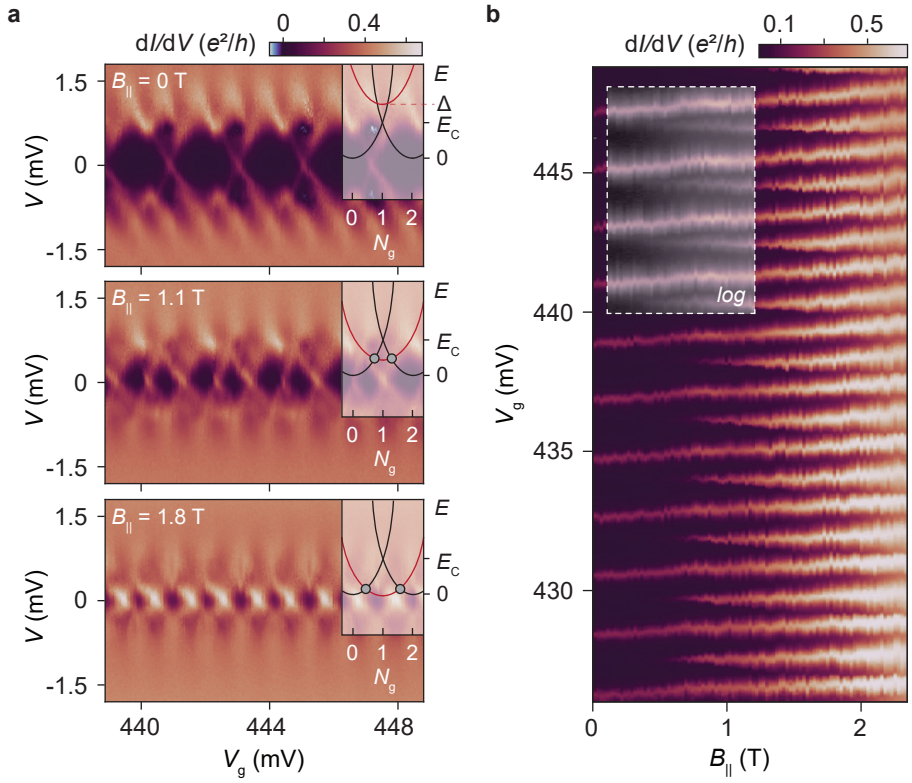

Figure 7.2: a. Differential conductance maps at various magnetic field in a different gate-voltage range of the same device as in Figure 7.1d. The three panels show the transition from the $2e$-charging regime (top panel, $B_\parallel = 0\,\mathrm{T}$), to the even-odd regime (middle panel, $B_\parallel = 1.1\,\mathrm{T}$) and the $1e$-charging regime (bottom panel, $B_\parallel = 1.8\,\mathrm{T}$). The insets show the corresponding energy diagrams, where the black (red) parabolas represent the energy of the even (odd) charge states, as a function of the normalized gate voltage, N_g. **b.** Magnetic field dependence of the zero-bias $\mathrm{d}I/\mathrm{d}V$ in an extended gate-voltage range, showing the gradual transition between the different regimes. The inset shows the underlying data on a logarithmic scale, to clarify the splitting of the $2e$-periodic Coulomb peaks.

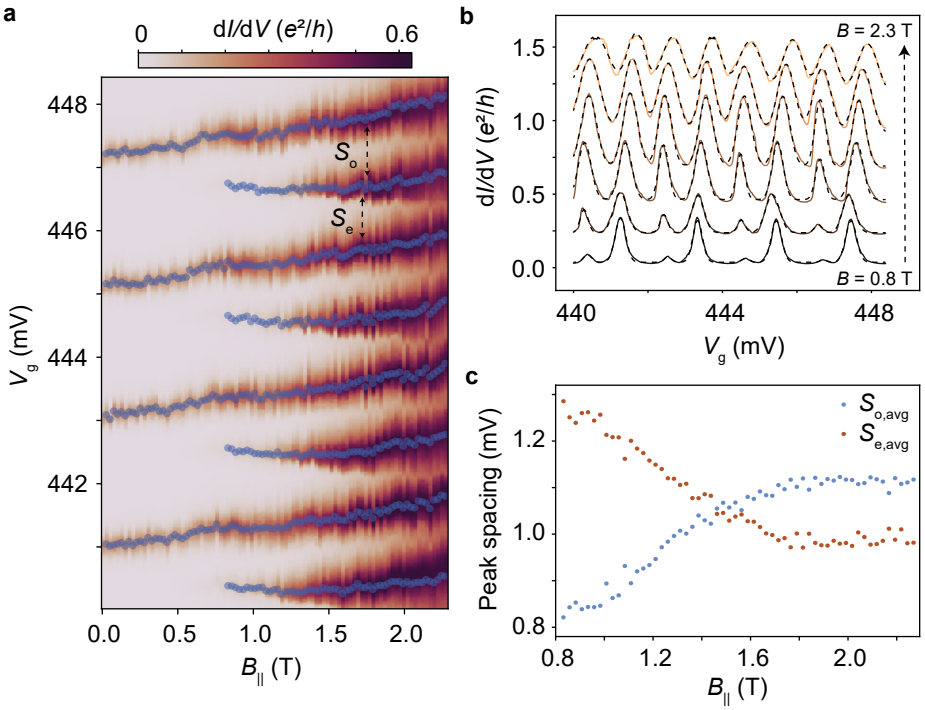

Figure 7.3: Magnetic-field evolution of the Coulomb-peak spacings. a. Fitted Coulomb-peak center positions (blue dots) in the Coulomb-blockade spectroscopy data of Figure 7.2b in the gate-voltage range $V_g = 440\,\text{mV}$ to $V_g = 449\,\text{mV}$. **b.** Selection of gate-voltage traces from **a** with the fitted traces superimposed (dashed lines). **c.** Magnetic-field dependence of the average even- and odd Coulomb-peak spacings.

section, we further analyze the magnetic-field dependent behavior by focusing on the evolution of the Coulomb-peak spacings.

7.3. ANALYSIS OF THE COULOMB-PEAK SPACING

Previous studies on hybrid nanowire devices have studied the magnetic-field dependence of the Coulomb-peak spacings in the context of hybridized Majorana modes at the ends of the nanowire [4]. Oscillations in the peak spacings are expected to be a signature of this hybridization and are exponentially suppressed as the distance between the Majorana modes is increased. For comparison with aluminum-based hybrid nanowire devices we discuss here the magnetic-field evolution of the Coulomb-peak spacings of the InAs/Pb island. We first focus on the Coulomb-blockade spectroscopy measurements in the same gate-voltage range as in Figure 7.2 and later on measurements of the same device in a different gate-voltage range.

In order to accurately determine the peak positions we fit each gate-voltage trace with a function containing multiple Gaussian functions on top of a constant background. To

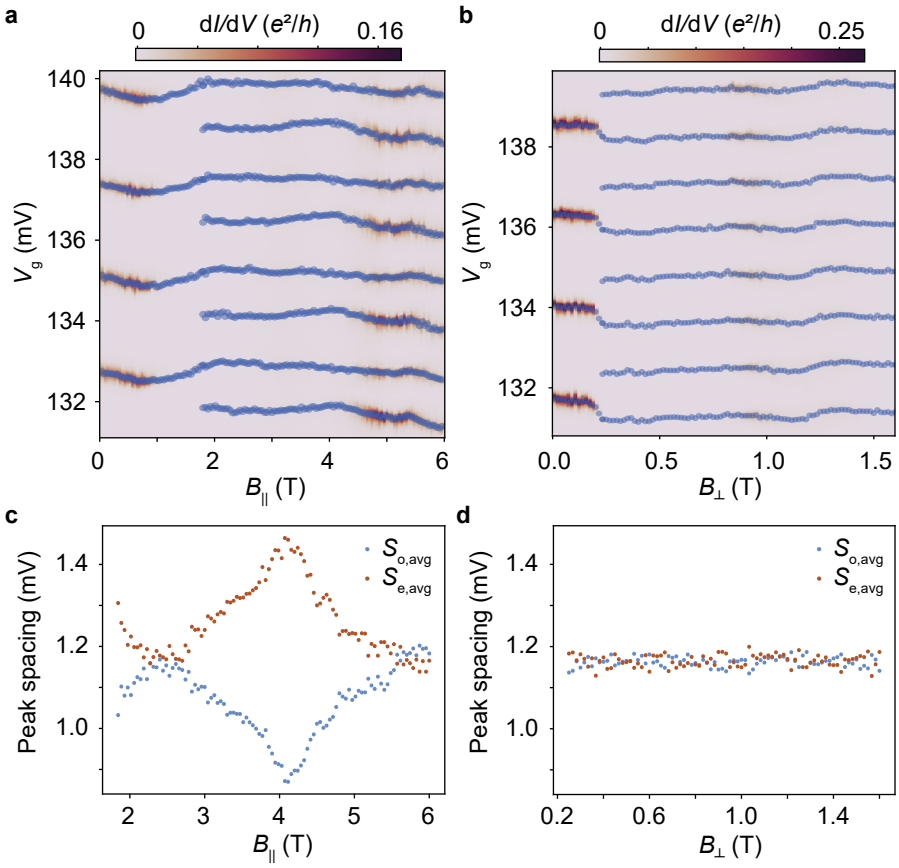

Figure 7.4: a. Coulomb-peak spacing evolution in the gate-voltage range corresponding to Figure 7.1d. Fitted Coulomb-peak center positions for parallel magnetic field. **b.** Same as **a** for perpendicular magnetic field. **c.** Magnetic-field dependence of $S_{e,avg}$ and $S_{o,avg}$ for parallel magnetic field. **d.** Same as **c** for perpendicular magnetic field.

limit the number of fitting parameters we restricted the analysis to the gate-voltage range $V_g = 440\,\text{mV}$ to $V_g = 449\,\text{mV}$, in which 8 peaks can be clearly identified at high magnetic field. The strong asymmetry in intensity between the two sets of Coulomb peaks at low magnetic fields limits our analysis to the range $B_\parallel > 0.8\,\text{T}$ for which 8 peaks could be reliably fitted (see Figure 7.3b). In Figure 7.3a, the center positions of the Coulomb peaks obtained from the fit are marked by blue dots, superimposed on the $\mathrm{d}I/\mathrm{d}V$ map. For completeness we show the peak-center positions also in the range $B_\parallel < 0.8\,\text{T}$ for which we reduced the number of Gaussian functions to 4 to ensure reliable fit results. We distinguish between the peak spacings in the even charge states and the odd charge states as indicated by S_e and S_o, respectively.

The average values of the peak spacings for $B_\parallel > 0.8\,\text{T}$ are shown in Figure 7.3c. Near $B_\parallel = 0.8\,\text{T}$ the difference between $S_{e,avg} \approx 1.3\,\text{mV}$ and $S_{o,avg} \approx 0.8\,\text{mV}$ implies that the is-

land is well within the even-odd regime at this magnetic field. Around $B_{\parallel} = 1.5\,\mathrm{T}$ the even- and odd spacings become equal and a regular $1e$-spaced Coulomb-peak pattern is obtained. At even higher fields $S_{\mathrm{e,avg}}$ and $S_{\mathrm{o,avg}}$ appear to converge to different values. This might be the onset of a Coulomb-peak spacing oscillation as observed by Albrecht et al. (2016) [4], which was interpreted as a fingerprint of topological zero-energy bound states. In this device, we were unable to confirm oscillatory behavior due to its instability at higher magnetic fields. The modulation of the peak spacing in the fitted gate-voltage range does suggest that the doubling of the Coulomb peaks is not due to quasiparticle poisoning or the quenching of superconductivity for which a uniform $1e$-spacing is expected [7].

We performed the same Coulomb-peak analysis in a different gate-voltage range of the same device for both the parallel magnetic field $B_{\parallel}$ as well as the perpendicular magnetic field $B_{\perp}$. The results are presented in Figure 7.4. For the parallel magnetic field we again observe a strong modulation of $S_{\mathrm{e,avg}}$ and $S_{\mathrm{o,avg}}$ where in this case we are able to resolve a complete oscillation. In contrast, the same measurement in the perpendicular magnetic-field direction shows no measurable oscillations. The uniform $1e$-spacing may suggest that superconductivity was quenched around $B_{\perp} = 0.2\,\mathrm{T}$, or may be a result of one or more trivial bound states converging around zero energy [8, 17, 18].

7.4. CONCLUDING REMARKS

The transport measurements presented in this chapter demonstrate some of the essential requirements for topological superconductivity, such as the quantization of charge in units of $2e$ and the observation of single-electron transport through bound states at finite magnetic field. These observations highlight the potential of InAs nanowires with epitaxial Pb to be used for topological applications and motivate further studies using this novel material system. Future work could e.g. focus on island-length-dependent studies, which could give information about whether the zero-energy bound states observed in the hybrid system are in fact topological. The attractive superconducting properties of the InAs/Pb hybrid allow for conducting experiments in a significantly extended parameter space — large superconducting gap, high critical field, high critical temperature — as compared to previous studies using aluminum-based devices [4, 9]. Future experiments could therefore benefit from a significantly extended range of operating temperatures, including liquid-helium temperature. In addition, the InAs/Pb nanowires can be of great interest in studies of subgap Yu-Shiba-Rusinov states (see Section 2.6.2), which could be probed in great detail due to the large superconducting gap of Pb.

REFERENCES

[1] T. Kanne, M. Marnauza, D. Olsteins, D. J. Carrad, J. E. Sestoft, **J. de Bruijckere**, L. Zeng, E. Johnson, E. Olsson, K. Grove-Rasmussen, and J. Nygård. "Epitaxial Pb on InAs nanowires" (Feb. 26, 2020). arXiv: http://arxiv.org/abs/2002.11641v1 [cond-mat.mes-hall].

[2] R. M. Lutchyn, E. P. A. M. Bakkers, L. P. Kouwenhoven, P. Krogstrup, C. M. Marcus, and Y. Oreg. "Majorana zero modes in superconductor–semiconductor heterostructures". *Nature Reviews Materials* 3.5 (May 2018), pp. 52–68. DOI: 10.1038/s41578-018-0003-1.

[3] V. Mourik, K. Zuo, S. M. Frolov, S. R. Plissard, E. P. A. M. Bakkers, and L. P. Kouwenhoven. "Signatures of Majorana Fermions in Hybrid Superconductor-Semiconductor Nanowire Devices". *Science* 336.6084 (Apr. 2012), pp. 1003–1007. DOI: 10.1126/science.1222360.

[4] S. M. Albrecht, A. P. Higginbotham, M. Madsen, F. Kuemmeth, T. S. Jespersen, J. Nygård, P. Krogstrup, and C. M. Marcus. "Exponential protection of zero modes in Majorana islands". *Nature* 531.7593 (Mar. 2016), pp. 206–209. DOI: 10.1038/nature17162.

[5] J. Paajaste, M. Amado, S. Roddaro, F. S. Bergeret, D. Ercolani, L. Sorba, and F. Giazotto. "Pb/InAs Nanowire Josephson Junction with High Critical Current and Magnetic Flux Focusing". *Nano Letters* 15.3 (Feb. 2015), pp. 1803–1808. DOI: 10.1021/nl504544s.

[6] D. Aasen, M. Hell, R. V. Mishmash, A. Higginbotham, J. Danon, M. Leijnse, T. S. Jespersen, J. A. Folk, C. M. Marcus, K. Flensberg, and J. Alicea. "Milestones Toward Majorana-Based Quantum Computing". *Physical Review X* 6.3 (Aug. 2016). DOI: 10.1103/physrevx.6.031016.

[7] S. M. Albrecht, E. B. Hansen, A. P. Higginbotham, F. Kuemmeth, T. S. Jespersen, J. Nygård, P. Krogstrup, J. Danon, K. Flensberg, and C. M. Marcus. "Transport Signatures of Quasiparticle Poisoning in a Majorana Island". *Physical Review Letters* 118.13 (Mar. 2017). DOI: 10.1103/physrevlett.118.137701.

[8] J. Shen, S. Heedt, F. Borsoi, B. van Heck, S. Gazibegovic, R. L. M. O. het Veld, D. Car, J. A. Logan, M. Pendharkar, S. J. J. Ramakers, G. Wang, D. Xu, D. Bouman, A. Geresdi, C. J. Palmstrøm, E. P. A. M. Bakkers, and L. P. Kouwenhoven. "Parity transitions in the superconducting ground state of hybrid InSb–Al Coulomb islands". *Nature Communications* 9.1 (Nov. 2018). DOI: 10.1038/s41467-018-07279-7.

[9] S. Vaitiekėnas, G. W. Winkler, B. van Heck, T. Karzig, M.-T. Deng, K. Flensberg, L. I. Glazman, C. Nayak, P. Krogstrup, R. M. Lutchyn, and C. M. Marcus. "Flux-induced topological superconductivity in full-shell nanowires". *Science* 367.6485 (Mar. 2020), eaav3392. DOI: 10.1126/science.aav3392.

[10] M. Pendharkar, B. Zhang, H. Wu, A. Zarassi, P. Zhang, C. P. Dempsey, J. S. Lee, S. D. Harrington, G. Badawy, S. Gazibegovic, J. Jung, A.-H. Chen, M. A. Verheijen, M. Hocevar, E. P. A. M. Bakkers, C. J. Palmstrøm, and S. M. Frolov. "Parity-preserving and magnetic field resilient superconductivity in indium antimonide nanowires with tin shells" (Dec. 11, 2019). arXiv: http://arxiv.org/abs/1912.06071v1 [cond-mat.mes-hall].

[11] J. E. Sestoft, T. Kanne, A. N. Gejl, M. von Soosten, J. S. Yodh, D. Sherman, B. Tarasinski, M. Wimmer, E. Johnson, M. Deng, J. Nygård, T. S. Jespersen, C. M. Marcus, and P. Krogstrup. "Engineering hybrid epitaxial InAsSb/Al nanowires for stronger topological protection". *Physical Review Materials* 2.4 (Apr. 2018). DOI: 10.1103/physrevmaterials.2.044202.

[12] B. van Heck, R. M. Lutchyn, and L. I. Glazman. "Conductance of a proximitized nanowire in the Coulomb blockade regime". *Physical Review B* 93.23 (June 2016). DOI: 10.1103/physrevb.93.235431.

[13] D. V. Averin and Y. V. Nazarov. "Single-electron charging of a superconducting island". *Physical Review Letters* 69.13 (Sept. 1992), pp. 1993–1996. DOI: 10.1103/physrevlett.69.1993.

[14] J. M. Thijssen and H. S. J. van der Zant. "Charge transport and single-electron effects in nanoscale systems". *physica status solidi (b)* 245.8 (Aug. 2008), pp. 1455–1470. DOI: 10.1002/pssb.200743470.

[15] M. T. Deng, S. Vaitiekėnas, E. B. Hansen, J. Danon, M. Leijnse, K. Flensberg, J. Nygård, P. Krogstrup, and C. M. Marcus. "Majorana bound state in a coupled quantum-dot hybrid-nanowire system". *Science* 354.6319 (Dec. 2016), pp. 1557–1562. DOI: 10.1126/science.aaf3961.

[16] E. B. Hansen, J. Danon, and K. Flensberg. "Probing electron-hole components of subgap states in Coulomb blockaded Majorana islands". *Physical Review B* 97.4 (Jan. 2018). DOI: 10.1103/physrevb.97.041411.

[17] S. Vaitiekėnas, A. Whiticar, M.-T. Deng, F. Krizek, J. Sestoft, C. Palmstrøm, S. Marti-Sanchez, J. Arbiol, P. Krogstrup, L. Casparis, and C. Marcus. "Selective-Area-Grown Semiconductor-Superconductor Hybrids: A Basis for Topological Networks". *Physical Review Letters* 121.14 (Oct. 2018). DOI: 10.1103/physrevlett.121.147701.

[18] S. Vaitiekėnas, M.-T. Deng, J. Nygård, P. Krogstrup, and C. Marcus. "Effective g Factor of Subgap States in Hybrid Nanowires". *Physical Review Letters* 121.3 (July 2018). DOI: 10.1103/physrevlett.121.037703.

8

CONCLUSION AND OUTLOOK

In the following chapter we conclude this thesis by discussing the main conclusions of the previous chapters and providing an outlook for future experiments. We relate the ideas to the relevant literature and give motivations for why one might continue along these lines of research.

The collection of studies presented in this thesis offers a glimpse into the field of charge transport through single molecules and displays some of the diverse behavior molecular devices can exhibit. In the previous chapters we mainly focused on studying the physics of molecular *spin*. The first system we studied in Chapter 3 was a diradical molecule. We found that this molecule behaved as a two-spin system when embedded in an electronic circuit and we were able to probe the associated transitions between spin-singlet and spin-triplet states. The spin-excitation spectra could be accurately simulated by an elementary tunneling model. This model behavior makes the diradical molecule an attractive platform for future experiments which encompass additional elements, such as superconducting electrodes. Since superconducting transport is often difficult to interpret, adding a well-understood molecule to the circuit is preferable in this regard. A potentially interesting research topic would be the interaction between superconductivity and the exchange coupling of the molecular spin system. The exchange coupling we measured in Chapter 3 was found to range between 1 and a few meV, which is similar to the superconducting gap, Δ, of the superconducting materials discussed in Chapter 6. The interaction between a radical spin and a superconductor — which gives rise to the formation of Yu-Shiba-Rusinov bound states — may therefore be strongly influenced by the exchange coupling between the two radical spins, similar to how the Kondo effect competes with superconductivity when $T_K \sim \Delta$ [1]. The exceptionally high charging energy of the single-molecule device would ensure that one could study this interaction in a well-isolated and stable charge state, unlike other nano-objects where the charging energy is similar to other energy scales.

The three-spin behavior of the same type of diradical molecule was studied in Chapter 4. Whereas for most devices we were not able to change the charge state, in this particular device we could reversibly reduce the diradical molecule, i.e., add an electron, by the gate voltage. Remarkably, we found that the reduced single-molecule device behaved as a three-spin system and we were able to probe its two doublet and one quartet states. The scarcity of devices in which the three-spin state was accessible makes the diradical molecule not the most suitable system for studying the behavior of exchange-coupled three-spin clusters. Nevertheless, using this device we could perform a novel analysis of the three exchange couplings based on the step height of the cotunneling excitations. Even though a strong Kondo coupling made it difficult to draw definite conclusions for this particular device, in other three-spin devices the same analysis could be a valuable tool. For instance, a topic of debate in many single-molecule devices is the path the electric current takes through the molecule. In most cases one can only speculate about whether transport occurs exclusively through the ligand orbitals, or whether the core orbitals of the molecule also play a role. The proposed exchange-coupling analysis can provide extra information on this topic, as it could reveal whether one or multiple interfering current paths are involved.

Future studies of molecular three-spin systems could also focus on the observation of exotic Kondo effects, which have been theoretically studied over the past years. One example of this is the ferromagnetic Kondo effect [2–4]. This phenomenon is predicted to emerge in three-spin spin clusters in a specific region of the parameter space spanned by the three exchange couplings. It involves the formation of a Kondo cloud in the leads

which is ferromagnetically coupled to the effective spin of the three-spin cluster — in contrast to the standard Kondo effect, where this coupling is antiferromagnetic. The experimental fingerprints of this effect include an inverted zero-bias anomaly and a strong magnetic-field dependence [3]. For these potential future studies of molecular three-spin systems one option would be to use the triradical molecule from the same family of organic radicals as the diradical molecule [5]. Previous experiments have demonstrated that this triradical molecule is suitable for electromigration studies [6] and is a more robust three-spin system than the reduced diradical molecule.

In Chapter 5 we focused on the first experimental observation of ground-state spin blockade in a single-molecule junction. These measurements highlight the rich spin structure that single-molecule devices can have and the dramatic influence of molecular spin on charge transport. Whether resonant transport could occur depended on the sign of the exchange coupling between the ligand orbital and the Mn-ion core of the polyoxometalate molecule used in this study. The blockade occurred due to a charge-induced sign flip of the exchange coupling which resulted in a spin difference between the ground states of adjacent charge states larger than the spin of a conduction electron. Only a small number of devices with polyoxometalate molecules were measured for this study and it is therefore unclear whether the observation of ground-state spin blockade was a rare event, or a general feature of the molecule. Future studies would be able to answer this question and could focus on more fundamental properties of the blockade. Given the large difference of the ground-state spins, it would be interesting to measure the associated changes in the molecule's entropy [7]. The change in entropy across a charge transition causes a shift of the associated Coulomb peak with temperature [8]. In the case of ground-state spin blockade however, there are no Coulomb peaks. Perhaps still, if one would be able to measure the shift of the ground-state transition — e.g. through clever extrapolation of the excitation lines — one may be able to observe entropy changes exceeding the value $k_B \ln 2$, i.e., the entropy of a single spin-1/2 system.

Experimental observations of exotic phenomena in single-molecule junctions such as the ground-state spin blockade and the two-stage Kondo effect are often serendipitous events. This is in part due to the fact that the electromigration break junction is inherently stochastic; the way molecules are trapped in a junction cannot be controlled and the amount of control is restricted to adjusting global parameters such as the magnetic field and the gate voltage. Whether the gate voltage tunes the desired parameters of the experiment in turn depends on the microscopic details of the molecular junction, which cannot be controlled. Despite these limitations, once a single-molecule electromigration device has been realized it can in principle be measured for as long as one cares to keep it at cryogenic temperatures. The device can therefore be mapped out in great detail, as demonstrated throughout this thesis. In addition, as of yet no other method exists by which nano-objects as small as individual molecules can be simultaneously probed *and* tuned — by the gate electrode. The electromigration technique therefore remains a unique and invaluable tool for fundamental and exploratory single-molecule studies.

As discussed in Chapter 6, the electromigration break junction technique can also be of great interest in the field of hybrid superconducting devices. Being able to measure transport through a single molecule with superconducting electrodes in a transistor-like device opens up the possibility to study superconducting transport in a unique experi-

mental regime where the charging energy is effectively infinite — a limit commonly considered in theoretical studies. The supercurrent through a nano-object is typically governed by transport processes which involve the double occupation of the nano-object. In contrast, in single molecules the charging energy is so high that only those processes which do not involve the charging energy are relevant [9, 10]. In future studies, molecules with unique properties such as high-spin states and magnetic anisotropy can be measured e.g. to investigate the predicted influence of magnetic anisotropy on the supercurrent [11, 12]. But perhaps the most attractive topic to pursue at the time of writing is the emergence of subgap bound states, such as the Yu-Shiba-Rusinov states mentioned above and in Chapter 6. Subgap bound states play an important role in the field of superconductivity e.g. for the realization of topological superconductivity, which could potentially be used for fault-tolerant quantum computing, as discussed in Chapter 7. The large separation of energy scales in single molecules in combination with their unique chemically-tailored properties provide an attractive experimental platform for future experiments in this direction.

REFERENCES

[1] K. J. Franke, G. Schulze, and J. I. Pascual. "Competition of Superconducting Phenomena and Kondo Screening at the Nanoscale". *Science* 332.6032 (May 2011), pp. 940–944. DOI: 10.1126/science.1202204.

[2] A. K. Mitchell, T. F. Jarrold, and D. E. Logan. "Quantum phase transition in quantum dot trimers". *Physical Review B* 79.8 (Feb. 2009). DOI: 10.1103/physrevb.79.085124.

[3] P. P. Baruselli, R. Requist, M. Fabrizio, and E. Tosatti. "Ferromagnetic Kondo Effect in a Triple Quantum Dot System". *Physical Review Letters* 111.4 (July 2013). DOI: 10.1103/physrevlett.111.047201.

[4] A. K. Mitchell, T. F. Jarrold, M. R. Galpin, and D. E. Logan. "Local Moment Formation and Kondo Screening in Impurity Trimers". *The Journal of Physical Chemistry B* 117.42 (Apr. 2013), pp. 12777–12786. DOI: 10.1021/jp401936s.

[5] J. Veciana, C. Rovira, N. Ventosa, M. I. Crespo, and F. Palacio. "Stable polyradicals with high-spin ground states. 2. Synthesis and characterization of a complete series of polyradicals derived from 2,4,6 - trichloro - α,α,α',α',α'',α'' - hexakis(pentachlorophenyl)mesitylene with S = 1/2, 1, and 3/2 ground states". *Journal of the American Chemical Society* 115.1 (Jan. 1993), pp. 57–64. DOI: 10.1021/ja00054a008.

[6] R. Gaudenzi, E. Burzurí, D. Reta, I. de P. R. Moreira, S. T. Bromley, C. Rovira, J. Veciana, and H. S. J. van der Zant. "Exchange Coupling Inversion in a High-Spin Organic Triradical Molecule". *Nano Letters* 16.3 (Feb. 2016), pp. 2066–2071. DOI: 10.1021/acs.nanolett.6b00102.

[7] N. Hartman, C. Olsen, S. Lüscher, M. Samani, S. Fallahi, G. C. Gardner, M. Manfra, and J. Folk. "Direct entropy measurement in a mesoscopic quantum system". *Nature Physics* 14.11 (Aug. 2018), pp. 1083–1086. DOI: 10.1038/s41567-018-0250-5.

[8] C. W. J. Beenakker. "Theory of Coulomb-blockade oscillations in the conductance of a quantum dot". *Physical Review B* 44.4 (July 1991), pp. 1646–1656. DOI: 10.1103/physrevb.44.1646.

[9] L. I. Glazman and K. A. Matveev. "Resonant Josephson current through Kondo impurities in a tunnel barrier". *JETP* 49.10 (1989), pp. 659–662.

[10] T. Novotný, A. Rossini, and K. Flensberg. "Josephson current through a molecular transistor in a dissipative environment". *Physical Review B* 72.22 (Dec. 2005). DOI: 10.1103/physrevb.72.224502.

[11] I. A. Sadovskyy, D. Chevallier, T. Jonckheere, M. Lee, S. Kawabata, and T. Martin. “Josephson effect through an anisotropic magnetic molecule”. *Physical Review B* 84.18 (Nov. 2011). DOI: 10.1103/physrevb.84.184513.

[12] P. Stadler, C. Holmqvist, and W. Belzig. “Josephson current through a quantum dot coupled to a molecular magnet”. *Physical Review B* 88.10 (Sept. 2013). DOI: 10.1103/physrevb.88.104512.

Acknowledgements

In September 2014 I joined the group molecular electronics and devices, better known as MED, for my master's thesis project. I already knew one of the professors, Herre, from the courses Mesoscopic Physics and Molecular Electronics he taught, and I found his style of teaching very refreshing. For that reason I had asked him about the possibilities of doing a master's thesis project in his group and he referred me to Rocco, who later became my supervisor. Immediately after joining MED I was pleasantly surprised by the welcoming atmosphere and the social cohesion of this wildly diverse group of people. After the good times I had during my master's project, the decision to stay for a PhD was not a difficult one. Therefore, first and foremost, I would like to thank you, Herre, for this opportunity you gave me. Working with you has been a very pleasant experience and I am grateful for the trust and freedom you have given me in all these years. Even during the times when all equipment failed, I never felt like I was on my own. You stayed involved and helped me in thinking about solutions, even when that solution was moving to another country for the continuation of my PhD. Joining the group of Jesper Nygård in Copenhagen for the last year was an amazing opportunity you made possible and I am very grateful for it. For that opportunity I also want to thank you, Jesper, for your generous hospitality; I felt very welcome in your group and I had a wonderful time. And I want to acknowledge the other members of my PhD committee. Now that thanking you in person is not an option due to travel restrictions, I want to mention here that I highly appreciate you have taken the time to evaluate my thesis and be part of my defense committee in these strange times.

Next I would like to thank Rocco. You have taught me so much and I am grateful that I got to work with you. Your passion for science and many other aspects of life was contagious and truly inspiring. I miss our long discussions and witnessing your signature beach-volleyball move, 'the tulip'! Also thanks to the other inhabitants of F394, Max and Shun, for being great office mates! After you all left I was the only one left in the office for quite some time, until Pascal joined the group. This goofy German brought the lab back to life and I was very happy that I got someone to spar with again. I want to thank you Pascal, for sharing your passion for beer and board games, and making the last years of my PhD life much more entertaining. I hope the future will allow you to measure many more "lekkere Kondootjes"! The second German that played a prominent role during my time at MED was Holger. I want to thank you for your curiosity and enthusiasm; you were always up for a late-night beer, a good discussion, a game, anything! You are hereby forgiven for any misspellings of Dutch family names. Then Nikos, I want to thank you for the positive energy you brought inside and outside of the lab. I am glad we were able to share some of our mutual passion for music and I hope that after the lockdown you can display your deejaying skills again! Talking about DJs, dank je wel Dirk voor de wetenschappelijke samenwerking. Ik vond het leuk dat we nog een goed feestje in Amsterdam

konden meepakken, praktisch in jouw achtertuin! En Mafalda, tegen jou kan ik inmiddels ook net zo goed Nederlands praten. Ook jij bedankt voor het samenwerken en de gezelligheid! Giordano, thank you for your endless enthusiasm and for taking the initiative for so many great activities and pranks; MED wouldn't have been the same without you. I hope the three gods aren't still haunting you in your sleep! Thank you Yildiz for the positive energy you always brought to work, even after nearly losing your leg! Good luck with the last part of your PhD! And also thank you to all the other members of the Caviglia lab: Andrea, Dima, Jorrit, Emre, Lucinda, Bas, Inge, Edouard, Nicola and Thierry (I'm sorry for giving you the dilution-fridge curse...). Ranko, dank je wel voor alle gezelligheid, en hopelijk blijf je nog lang in Nederland; dan zien we elkaar wel weer! Dejan, thank you for being a reliable source of NSFW jokes; it has been of crucial importance in the many great songs we wrote! Thank you Floris for displaying your unique dance moves and for the career advice you have already given me. Marc, thank you for your contagious laughter and your memorable Whatsapp monologues; they have made my day more than once! The same holds for Santiago, thank you for making sure MED never became a boring place! Thank you Davide for being a great lab-neighbor and for still speaking to me after many betrayals in our Diplomacy game!

And thank you to all the other people of the Van der Zant lab: Alexandra, Enrique, Joshua and Mickael; I had a great time collaborating with you and I am grateful for the knowledge you shared with me. My two master students, Damian and Damianos; you both did an amazing job and I foresee a successful continuation of your careers! Thank you Julien, Diana, Ignacio, Nandini, Maria, Thomas, Luca, Chunwei, Davide, Sabina, Vera, Benjamin, Jacqui, Martijn, Eugenio, Matthijs and Jasper. I wish you all the best! Also a big thanks to all the staff: Heleen, Tino, Maria, Dorine, Erika, Marijke, Etty and Marije. And thank you Alessandro, for showing me the art of evaporating superconductors the old-school way. Thanks to all the other people at QN, including my mentor Gary, Iacopo, João, Andreas, Marios, Felix, Rasa, Mario, Sarwan, Brecht, Sonakshi, Martin, Ines, Jérémie, Jan and Luigi!

Then to everyone I worked with in Copenhagen, I am grateful that I had the possibility to work in a great scientific environment with such a nice group of people. Jens and Per, thank you for inviting me to visit Copenhagen and working together on the spin-blockade paper. And thanks to Juan-Carlos, Kasper, I-Ju, Alex, Damon, Joachim, Sara, Victoria, Thomas, Michelle, Gorm, Dags and Mikelis for your collaborations and your hospitality. Thank you Martin, Karolis, Nader, for training me in the clean room and Maria and Dorthe for making sure I had everything I needed upon arrival.

Verder wil ik nog Michel, Steven, Robin en Eva bedanken voor de ontzettend leuke tijd die we gehad hebben op de Rotterdamseweg! Ik vond het erg fijn dat zelfs na mijn verhuizing ik nog altijd een slaapplek bij jullie kon vinden wanneer ik voor werk in Nederland was. Dat geldt ook voor Astrid, heel erg bedankt daarvoor!

En dan mijn familie. Mam en pap, heel erg bedankt voor jullie steun en voor jullie interesse in mijn werk! En dat geldt ook voor Lotte, Ayla, Bertie, oma Simone, Geert, Karin, Agim, Cees en Tom. Dank jullie wel!

Ten slotte, Laurie, dank je wel voor jouw steun, liefde en het plezier wat je mij hebt gegeven. Ik ben heel blij dat ik het laatste jaar van mijn PhD samenwonend met jou in Kopenhagen heb kunnen meemaken!

CURRICULUM VITÆ

Joeri DE BRUIJCKERE

5-3-1992 Born in Oostburg, the Netherlands.

EDUCATION

2004–2010 Secondary School
Zwin College, Oostburg

2010–2013 Bachelor of Science in Mechanical Engineering, *cum laude*
Delft University of Technology
Thesis: Zebro Light: Lightweight Mobile Hexapod Robot
Supervisor: Prof. dr. R. Babuška

2012–2013 Honours Programme Bachelor
Delft University of Technology

2013–2015 Master of Science in Applied Physics, *cum laude*
Delft University of Technology
Short rotation 1: Engineering Functionalities in Vanadate Heterostructures
Supervisor: Dr. S. Gariglio (University of Geneva)
Short rotation 2: Superconductivity in $NbSe_2$ Single Layers
Supervisor: Prof. dr. J. I. Pascual (CIC nanoGUNE, San Sebastián)
Long rotation: Superconducting Transport through Individual Fe_4 Single-Molecule Magnets
Supervisor: Prof. dr. ir. H. S. J. van der Zant (TU Delft)

2016–2020 PhD in Physics
Delft University of Technology
Thesis: Correlated Spin Phenomena in Molecular Quantum Transport Devices
Supervisor: Prof. dr. ir. H. S. J. van der Zant

List of Publications

12. A. Vekris, J. C. E. Saldaña, **J. de Bruijckere**, K. Grove-Rasmussen, and J. Nygård. "Little Parks Oscillations in Double Nanowires" (*in preparation*)

11. P. Gehring, J. K. Sowa, C. Hsu, **J. de Bruijckere**, M. van der Sar, J. J. L. Roy, L. Bogani, E. M. Gauger, and H. S. J. van der Zant. "Vibrational coupling and spin-entropy in the thermoelectric properties of single-molecule junctions" (*in preparation*)

10. T. Kanne, M. Marnauza, D. Olsteins, D. J. Carrad, J. E. Sestoft, **J. de Bruijckere**, L. Zeng, E. Johnson, E. Olsson, K. Grove-Rasmussen, and J. Nygård. "Epitaxial Pb on InAs nanowires" (Feb. 26, 2020). arXiv: http://arxiv.org/abs/2002.11641v1 [cond-mat.mes-hall]

9. D. J. Groenendijk, N. Manca, **J. de Bruijckere**, A. M. R. V. L. Monteiro, R. Gaudenzi, H. S. J. van der Zant, and A. D. Caviglia. "Anisotropic magnetoresistance in spin-orbit semimetal $SrIrO_3$" (Jan. 24, 2020). arXiv: http://arxiv.org/abs/2001.08939v1 [cond-mat.str-el]

8. **J. de Bruijckere**, P. Gehring, M. Palacios-Corella, M. Clemente-León, E. Coronado, J. Paaske, P. Hedegård, and H. S. J. van der Zant. "Ground-State Spin Blockade in a Single-Molecule Junction". *Physical Review Letters* 122.19 (May 2019). DOI: 10.1103/physrevlett.122.197701

7. P. Zalom, **J. de Bruijckere**, R. Gaudenzi, H. S. J. van der Zant, T. Novotný, and R. Korytár. "Magnetically Tuned Kondo Effect in a Molecular Double Quantum Dot: Role of the Anisotropic Exchange". *The Journal of Physical Chemistry C* 123.18 (Apr. 2019), pp. 11917–11925. DOI: 10.1021/acs.jpcc.9b00783

6. H. Meley, Karandeep, L. Oberson, **J. de Bruijckere**, D. T. L. Alexander, J.-M. Triscone, P. Ghosez, and S. Gariglio. "Structural analysis of $LaVO_3$ thin films under epitaxial strain". *APL Materials* 6.4 (Apr. 2018), p. 046102. DOI: 10.1063/1.5021844

5. A. M. R. V. L. Monteiro, D. J. Groenendijk, I. Groen, **J. de Bruijckere**, R. Gaudenzi, H. S. J. van der Zant, and A. D. Caviglia. "Two-dimensional superconductivity at the (111) $LaAlO_3/SrTiO_3$ interface". *Physical Review B* 96.2 (July 2017). DOI: 10.1103/physrevb.96.020504

4. R. Gaudenzi, **J. de Bruijckere**, D. Reta, I. de P. R. Moreira, C. Rovira, J. Veciana, H. S. J. van der Zant, and E. Burzurí. "Redox-Induced Gating of the Exchange Interactions in a Single Organic Diradical". *ACS Nano* 11.6 (May 2017), pp. 5879–5883. DOI: 10.1021/acsnano.7b01578

3. D.-J. Choi, C. Rubio-Verdú, **J. de Bruijckere**, M. M. Ugeda, N. Lorente, and J. I. Pascual. “Mapping the orbital structure of impurity bound states in a superconductor”. *Nature Communications* 8.1 (May 2017). DOI: 10.1038/ncomms15175

2. J. O. Island, R. Gaudenzi, **J. de Bruijckere**, E. Burzurí, C. Franco, M. Mas-Torrent, C. Rovira, J. Veciana, T. M. Klapwijk, R. Aguado, and H. S. J. van der Zant. “Proximity-Induced Shiba States in a Molecular Junction”. *Physical Review Letters* 118.11 (Mar. 2017). DOI: 10.1103/physrevlett.118.117001

1. R. Gaudenzi, J. O. Island, **J. de Bruijckere**, E. Burzurí, T. M. Klapwijk, and H. S. J. van der Zant. “Superconducting molybdenum-rhenium electrodes for single-molecule transport studies”. *Applied Physics Letters* 106.22 (June 2015), p. 222602. DOI: 10.1063/1.4922042